AFRL-AFOSR-VA-TR-2020-0039

Multi-Step Computational Modeling and Shock-Tube Study of Energy Transfer Processes in High-Enthalpy Air

IAIN BOYD
REGENTS OF THE UNIVERSITY OF MICHIGAN

12/05/2019
Final Report

Air Force Research Laboratory
AF Office Of Scientific Research (AFOSR)/ RTA1
Arlington, Virginia 22203
Air Force Materiel Command

DISTRIBUTION A: Distribution approved for public release

REPORT DOCUMENTATION PAGE

Form Approved
OMB No. 0704-0188

1. REPORT DATE *(DD-MM-YYYY)*	2. REPORT TYPE	3. DATES COVERED *(From - To)*
16-03-2020	Final Performance	01 Sep 2016 to 30 Sep 2019

4. TITLE AND SUBTITLE
Multi-Step Computational Modeling and Shock-Tube Study of Energy Transfer Processes in High-Enthalpy Air

5a. CONTRACT NUMBER

5b. GRANT NUMBER
FA9550-16-1-0291

5c. PROGRAM ELEMENT NUMBER
61102F

6. AUTHOR(S)
IAIN BOYD, Ronald Hanson

5d. PROJECT NUMBER

5e. TASK NUMBER

5f. WORK UNIT NUMBER

7. PERFORMING ORGANIZATION NAME(S) AND ADDRESS(ES)
REGENTS OF THE UNIVERSITY OF MICHIGAN
503 THOMPSON ST
ANN ARBOR, MI 48109-1340 US

8. PERFORMING ORGANIZATION REPORT NUMBER

9. SPONSORING/MONITORING AGENCY NAME(S) AND ADDRESS(ES)
AF Office of Scientific Research
875 N. Randolph St. Room 3112
Arlington, VA 22203

10. SPONSOR/MONITOR'S ACRONYM(S)
AFRL/AFOSR RTA1

11. SPONSOR/MONITOR'S REPORT NUMBER(S)
AFRL-AFOSR-VA-TR-2020-0039

12. DISTRIBUTION/AVAILABILITY STATEMENT
A DISTRIBUTION UNLIMITED: PB Public Release

13. SUPPLEMENTARY NOTES

14. ABSTRACT
This project involved a carefully coordinated set of activities that aimed to significantly improve our understanding of the molecular energy transfer processes of oxygen species in flows of high enthalpy air characteristic of hypersonic vehicles. The work at the University of Michigan focused on computational analyses. Molecule-molecule interactions were studied using computational chemistry in which accurate potential energy surfaces (PES) for specific molecular interactions were used in high fidelity trajectory calculations to determine the process rates, resolved by internal energy state. The rates were used in master equation analyses of heat baths and shock waves. The heat bath analyses allowed the extraction of low order models that can be used in multi-dimensional computational fluid dynamics (CFD) simulations of hypersonic flows. At Stanford, shock tube experiments were conducted to generate new information and provide data to validate the models. Progress in this project focused on an improved absorption model for O2, design of experiments employing a shock tube code provided by Michigan, new measurements of vibrational relaxation times and dissociation rate coefficients of O2, and new measurements of excited state oxygen atoms.

15. SUBJECT TERMS
thermal-non equilibrium, Park model, Landau-Teller rates

16. SECURITY CLASSIFICATION OF:			17. LIMITATION OF ABSTRACT	18. NUMBER OF PAGES	19a. NAME OF RESPONSIBLE PERSON
a. REPORT	b. ABSTRACT	c. THIS PAGE			LEYVA, IVETT
Unclassified	Unclassified	Unclassified	UU		

Standard Form 298 (Rev. 8/98)
Prescribed by ANSI Std. Z39.18

				19b. TELEPHONE NUMBER *(Include area code)* 703-696-8478

FINAL TECHNICAL REPORT

Multi-Step Computational Modeling and Shock-Tube Study of Energy Transfer Processes in High-Enthalpy Air

AFOSR Grant FA9550-16-1-0291
Monitored by Ivett Leyva

Iain D. Boyd, PI
Department of Aerospace Engineering, University of Michigan

Ronald K. Hanson, Co-PI
Department of Mechanical Engineering, Stanford University

Summary
This project involved a carefully coordinated set of activities that aimed to significantly improve our understanding of the molecular energy transfer processes of oxygen species in flows of high enthalpy air characteristic of hypersonic vehicles. In the following, brief summaries are provided of the progress made in the project, and key papers representing the work from each institution are attached.

The work at the University of Michigan focused on computational analyses. Molecule-molecule interactions were studied using computational chemistry in which accurate potential energy surfaces (PES) for specific molecular interactions were used in high fidelity trajectory calculations to determine the process rates, resolved by internal energy state. The rates were used in master equation analyses of heat baths and shock waves. The heat bath analyses allowed the extraction of low order models that can be used in multi-dimensional computational fluid dynamics (CFD) simulations of hypersonic flows. Progress was made on analyzing the thermochemistry of the O_2-N_2 system as well as the interaction of NO with O_2, N_2, NO, N, and O. In addition, our shock tube models were extended considerably in order to analyze the electronically excited states of oxygen atoms. These simulations allowed direct comparison with new measurements developed at Stanford.

A second important research direction pursued at Michigan involved the evaluation of existing experimental data sets that are being used to assess new thermochemistry models. Shock tube experiments conducted in pure molecular oxygen in Russia were shown to have such large levels of uncertainty that makes it impossible to discriminate between different models. Double cone experiments conducted in a shock tunnel were found to have inconsistent trends that strongly suggests they are not suitable for thermochemistry model validation. A key outcome from this project is the recommendation that new experiments are needed in well-characterized facilities and that employ advanced diagnostics, in order to generate data sets suitable for chemistry model validation. Unpublished data with low error bars generated in the Stanford shock tube facilities near the end of the project provided the first set of vibrationally-resolved population densities that compared favorably with state-resolved analyses performed at Michigan.

At Stanford, shock-tube experiments have acquired absorption cross-sections, obtained novel state-specific time-histories, and determined kinetic rate parameters for molecular and atomic oxygen. Shock-tube/laser absorption measurements provide useful kinetic rate data and species time-histories for many species and conditions relevant to hypersonic flows. These measurements provide a more accurate picture of the chemical, vibrational and electronic relaxation processes in high-temperature air than currently exist. Work on shock tubes at Stanford University acquired reaction rates, relaxation rates, and species time-histories for molecular oxygen (O_2) and electronically excited atomic oxygen (O*). Specifically, these studies have expanded spectroscopic models for both species, measured state-specific time-histories for comparison with models, and obtained rates relevant to coupled vibration-dissociation (CVD), vibrational relaxation in air, and atomic excitation. Stanford experimental studies extended data to higher temperatures than previously studied and demonstrated the quantum-state-specificity of laser absorption diagnostics when applied to high-enthalpy air.

Studies of O_2 involved the development of a "Stanford Hybrid Model" to describe the absorption process of O_2, measurements of number density and vibrational temperature time-histories, and isolation of chemical and vibrational rate parameters. The Stanford Hybrid Model was developed to accurately simulate non-equilibrium absorption cross-section of molecular oxygen in the UV region. Model calculations informed wavelength selection for kinetic studies by determining which wavelengths had a majority of transitions arising from a specific lower vibrational level, and validation experiments were performed to confirm the accuracy of the model. Coupled vibration-dissociation processes in 2% and 5% O_2 in Ar mixtures were measured behind reflected shocks at temperatures between 5,300 and 10,700 K. The ratio of absorbance from two vibrational levels, interpreted via the Stanford Hybrid Model, was used to determine vibrational temperature (T_v) time-histories, and the number density ($n_{v''}$) time-histories were determined directly from the measured vibrational-level-specific absorbance. The temperature and number density time-histories were further analyzed to isolate coupling parameters from the Marrone and Treanor CVD model such as vibrational relaxation time (τ), average vibrational energy loss (E), vibrational coupling factor (Z), and dissociation rate constant (k_d). Finally, the vibrational relaxation times of O_2 in N_2 were measured in mixtures of 10% and 21% O_2 in N_2 at temperatures between 2000 and 4000 K for sub-atmospheric pressures. All experimental data for O_2 shows consistency with previous measurements, but with much lower uncertainty and scatter.

Studies of O* used scanned laser absorption techniques to isolate the Doppler temperature and measure electronic excitation time-histories. Stanford achieved the first direct measurements of O* at T > 8,000 K. During these measurements, the laser wavelength was rapidly scanned across the transitions to obtain spectrally- and temporally-resolved lineshape data. These data were used to infer key thermodynamic properties of O*, such as the translational temperature from the linewidth, and the population ratio from the integrated absorption area. The measured $O(3s\ ^5S^0)$ population time history revealed multi-stage behavior that was not observed in previous measurements over a temperature range of 5,300-7,200 K. To interpret the multi-stage behavior, a three-level collisional-radiative model for atomic oxygen excitation kinetics was developed, and rate parameters for this model were determined.

University of Michigan Publications

1. Andrienko, D.A. and Boyd, I.D., "Kinetic Models of Oxygen Thermochemistry Based on Quasi-Classical Trajectory Analysis," *Journal of Thermophysics and Heat Transfer*, Vol. 32, 2018, pp. 904-916.

2. Andrienko, D.A. and Boyd I.D., "Vibrational Energy Transfer and Dissociation in O_2-N_2 Collisions at Hyperthermal Temperatures," *Journal of Chemical Physics*, Vol. 148, 2018, Article 084309.

3. Neitzel, K., Andrienko, D., and Boyd, I.D., "Aerothermochemical Nonequilibrium Modeling for Oxygen Flows," *Journal of Thermophysics and Heat Transfer*, Vol. 31, 2017, pp. 634-645.

4. Andrienko, D.A. and Boyd I.D., "State-Specific Dissociation in O_2-O_2 Collisions By Quasiclassical Trajectory Method," *Chemical Physics*, Vol. 491, 2017, pp. 74-81.

5. Andrienko, D.A. and Boyd I.D., "Thermal Relaxation of Molecular Oxygen in Collisions With Nitrogen Atoms," *Journal of Chemical Physics*, Vol. 145, Article 014309, 2016.

6. Andrienko, D.A. and Boyd, I.D., "Master Equation Study of Vibrational and Rotational Relaxations of Oxygen," *Journal of Thermophysics and Heat Transfer*, Vol. 30, 2016, pp. 533-552.

7. Andrienko, D.A. and Boyd I.D., "Rovibrational Energy Transfer and Dissociation in O_2-O Collisions," *Journal of Chemical Physics*, Vol. 144, Article 104301, 2016.

8. Boyd, I.D. and Schwartzentruber, T.S., *Nonequilibrium Gas Dynamics and Molecular Simulation*, Cambridge University Press, March 2017.

9. Esposito, F., Macdonald, R., Boyd, I.D., Neitzel, K., and Andrienko, D.A., "Heavy-Particle Elementary Processes in Hypersonic Flows," *Hypersonic Meteoroid Entry Physics*, edited by G. Colonna, M. Capitelli, and A. Laricchiuta, IOP, 2019.

10. Hanquist, K. M. and Boyd, I. D., "Modeling of Electronically Excited Oxygen in O_2-Ar ShockTube Studies," AIAA Paper 2019-3567, June 2019.

11. Holloway, M.E, Hanquist, K.M., and Boyd, I.D., "Effect of Thermochemistry Modeling on Hypersonic Flow Over a Double Cone", AIAA Paper 2019-2281, January 2019.

12. Andrienko, D.A. and Boyd, I.D., "Molecular dynamics simulation of nitric oxide formation and extinction," AIAA Paper 2019-0791, January 2019.

13. Andrienko, D.A. and Boyd, I.D., "Kinetics of O_2–N_2 Collisions at Hypersonic Temperatures," AIAA Paper 2018-3438, June 2018.

14. Hanquist, K.M. and Boyd, I.D., "Modeling of Excited Oxygen in Post Normal Shock Waves," AIAA Paper 2018-3769, June 2018.

15. Andrienko, D.A., and Boyd, I.D., "Dissociation of Oxygen and Nitrogen in a Bimolecular Reaction at Hypersonic Temperatures," AIAA Paper 2018-0240, Jan 2018.

16. Andrienko, D.A., and Boyd, I.D., "State-Resolved Characterization of Nitric Oxide Formation in Shock Flows," AIAA Paper 2018-1233, Jan 2018.

17. Andrienko, D.A. and Boyd, I.D., "Master Equation Simulation of O_2-N_2 Collisions on an Ab-Initio Potential Energy Surface," AIAA Paper 2017-3163, June 2017.

18. Andrienko, D.A. and Boyd, I.D., "Simulation of Oxygen Dissociation on a Six-dimensional O_4 Potential Energy Surface," AIAA Paper 2017-3487, June 2017.

19. Andrienko, D.A., and Boyd, I.D., "State-Resolved O_2-N_2 Kinetic Model at Hypersonic Temperatures," AIAA Paper 2017-0659, January 2017.

20. Neitzel, K., Andrienko, D., and Boyd, I.D., "Thermochemical Nonequilibrium Modeling for Hypersonic Flows Containing Oxygen," AIAA Paper 2016-4023, June 2016.

21. Andrienko, D., and Boyd, I. D., "Vibrational Relaxation and Dissociation in O_2-O Mixtures," AIAA Paper 2016-4021, June 2016.

22. Andrienko, D. and Boyd, I. D., "High Fidelity Modeling of Thermal Relaxation and Dissociation of Oxygen," AIAA Paper 2016-0736, January 2016.

23. Andrienko, D. and Boyd, I. D., "Simulation of O_2 –N Collisions on ab-initio Potential Energy Surfaces," AIAA Paper 2016-1249, January 2016.

Stanford University Publications

24. Nations, M., “Laser-Based Diagnostics of Electronically Excited Oxygen Atoms at Extreme Temperatures,” Ph.D. Thesis, June 2016, Mechanical Engineering Department, Stanford University.

25. Nations, M., Wang, S., Goldenstein, C. S., Davidson D. F., and Hanson, R. K., “Kinetics of Excited Oxygen Formation in Shock-Heated O_2/Ar Mixtures,” submitted to *Journal Physical Chemistry A*, May 2016.

26. Nations, M., Wang, S., Goldenstein, C. S., Sun, K., Davidson, D.F., Jeffries, J.B., and Hanson, R.K., “Shock Tube Measurements of Excited Oxygen Atoms using Cavity-enhanced Absorption Spectroscopy,” *Applied Optics* 54 (29) 8766-8775 (2015) Selected by the Optical Society of America for “Spotlight on Optics.” for February 2016.

27. Owen, K., Davidson D. F., and Hanson, R. K., "Measurements of Oxygen Dissociation Laser Absorption" AIAA *Journal Thermophysics and Heat Transfer*, Published online February 16, 2016.

28. Owen, K., Davidson D. F., and Hanson, R. K., "Measurements of Vibrational Relaxation Times for Oxygen with Laser Absorption Spectroscopy in a Shock Tube," AIAA *Journal Thermophysics and Heat Transfer*, Published online December 22, 2015.

29. Owen, K., "Measurements of Vibrational Relaxation and Dissociation of Oxygen with Laser Absorption Spectroscopy with Applications for Energy Transfer in Non-Equilibrium Air," Engineers Thesis, May 2014, Mechanical Engineering Department, Stanford University.

30. Streicher, J.W., Krish, A., Wang, S., Davidson D. F., and Hanson, R. K., "Measurements of Oxygen Vibrational Relaxation and Dissociation Using Ultraviolet Laser Absorption in Shock Tube Experiments," manuscript submitted to AIAA SciTech 2019.

31. Krish, A., Streicher, J. W., and Hanson, R. K., "Ultraviolet Absorbance Cross-Section Measurements of Shock Heated O_2 using a Tunable Laser from 2,000-10,700 K," *Journal of Quantitative Spectroscopy and Radiative Transfer*, in prep.

32. Streicher, J.W., Krish, A., Hanson, R.K., Hanquist, K.M., Boyd, I.D., "Shock-Tube Measurements of Coupled Vibration-Dissociation in Dilute Mixtures of Oxygen in Argon Between 5,300 and 10,700 K Using Ultraviolet Laser Absorption Spectroscopy," *Journal of Chemical Physics*, in prep.

33. Streicher, J. W., Krish, A., and Hanson, R. K., "Shock-Tube Measurements of Vibrational Relaxation Times in Oxygen and Nitrogen Mixtures Using Ultraviolet Laser Absorption Spectroscopy," manuscript submitted to AIAA SciTech 2020.

34. Li, Y., Wang S. K., Strand C. L., and Hanson, R. K. "Two-Temperature Collisional-Radiative Modeling of Partially Ionized O_2-Ar Mixtures over 8000-10000K behind Reflected Shock Waves," in prep.

JOURNAL OF THERMOPHYSICS AND HEAT TRANSFER
Vol. 32, No. 4, October–December 2018

Kinetic Models of Oxygen Thermochemistry Based on Quasi-Classical Trajectory Analysis

Daniil A. Andrienko* and Iain D. Boyd†
University of Michigan, Ann Arbor, Michigan 48109

DOI: 10.2514/1.T4968

Recent progress in state-resolved kinetic models of thermal relaxation and dissociation of oxygen based on high-fidelity transition rate coefficients is presented. Specifically, three types of collisions encountered in high-temperature flows are discussed: O_2–O, O_2–N, and O_2–N_2. For these molecular systems, the thermal relaxation times and dissociation rate coefficients, obtained from extensive trajectory simulations, are compared with existing experimental data. A new set of calculations for O_2–N_2 on an ab-initio potential energy surface is presented. Accuracy of multitemperature models is assessed based on comparison with the solution of master equations. Recommendations for adjustable parameters employed in multitemperature models are provided.

I. Introduction

RECENT progress in hypersonic aerothermochemistry is associated with the modeling of nonequilibrium relaxation and dissociation from first principles using quantum-mechanical and semi- and quasi-classical methods. The initial capacity for such research was formed by the ever-increasing computational power that made statistical methods tractable, as well as by the variety of potential energy surfaces (PESs), developed for studies of low-temperature kinetics in the upper atmosphere [1–3].

Although a large amount of previous work regarding the nonequilibrium processes in high-temperature gases have concentrated on the state-resolved chemistry of nitrogen [4–11] and nitric oxide [12] due to the importance of these species in reentry and combustion problems, thermochemistry of oxygen has received little attention. This is because the atmosphere contains only one-fifth molar fraction of oxygen, and it dissociates easily under harsh reentry conditions. However, historical success and setbacks of hypersonic programs [13] have directed research in the study of oxygen nonequilibrium thermalization at lower speeds that correspond to the flight conditions of airbreathing hypersonic vehicles.

For diatomic oxygen, the most important collisions in terms of rovibrational relaxation and dissociation are observed with molecular oxygen and nitrogen as well as with atomic oxygen. Currently, only the latter type of collisions is studied in detail. For the O_2–O system, a number of PESs [14–17] of different fidelity are available due to the important property of the O_3 molecule to absorb harmful ultraviolet radiation [18]. The open-shell electrons of oxygen greatly complicate the treatment of ozone with standard methods. Such problems include nonadiabatic coupling between 27 PESs of the ground state of ozone, presence of reef structure that causes negative temperature dependence of rate coefficients, and isotope effect [1]. High-temperature kinetics of O_2–O collisions received special attention recently due to anomalously high rate coefficients (RCs) of vibrational transitions [19–23]. This phenomenon is associated with the small potential barrier in the entrance/exit channel of the O_2–O interaction. This subject is discussed in detail in the following sections.

The study of collisions of molecular oxygen with other diatomic air species is limited to low temperatures (say, 1000 K). There are a number of O_2–O_2 [3,24,25] and O_2–N_2 [2,26] PESs; however, they are designed only for low-energy collisions. In many cases, these PESs are either limited to a rigid rotor approximation, use empirical data to approximate the intermolecular forces, or do not describe the potential energy in bond-breaking collisions. Nevertheless, the semi- and quasi-classical calculations, conducted on these PESs, showed good agreement with measurements in the rates of vibration–translation (VT) and vibration–vibration (VV) energy transfer between diatomic species at room temperatures [27]. The interest in such kinetic models is dictated by the disagreement in theoretical and experimental predictions of ozone formation rates [1], probably due to some shadow mechanisms involving vibrationally excited O_2 [28,29].

Only recently the investigation of bimolecular collisions at higher temperatures received special attention [30,31] due to the availability of ab-initio four-body PESs. Six-dimensional N_4 PESs based on accurate quantum calculations were developed in the NASA Ames Research Center [32] and in the University of Minnesota [33]. More interesting, in the context of the present paper, is the recent global O_2N_2 PES by Varga et al. [31]. However, sampling all rovibrational states with good statistical accuracy using quasi-classical trajectory (QCT) simulations appears to be computationally intractable using these high-quality PESs. One of the possible ways to overcome this difficulty is the direct molecular simulation method, developed by Koura [34]. Although this approach makes it possible to obtain the average macroscopic parameters, such as vibrational and rotational relaxation times and the quasi-steady-state (QSS) dissociation RC of thermally and chemically nonequilibrium gas mixtures, this method does not allow extraction of the state-specific transition RCs that are typically required for detailed kinetic modeling and interpretation of experiments.

The present paper features the QCT calculations, conducted on the new O_2N_2 PES, and compares the global dissociation RCs and vibrational relaxation time with existing experimental data. The VT and VV energy transfer RCs for selected states are compared with other semiclassical calculations as well. The limitations and applicability of the present technique is discussed. The previous studies of O_2–O and O_2–N molecular systems are revisited and summarized, and general remarks about the computational cost of these three molecular systems are given. In Sec. II, the state-specific and multitemperature models are discussed. Section III presents the discussion of O_2–O, O_2–N, and O_2–N_2 molecular systems. Conclusions are drawn in Sec. IV.

II. Computational Approach

Molecular dynamics approaches can be tentatively divided into quantum [35–37], semiclassical [38–41], and quasi-classical [42,43] methods. The applicability of these methods is defined by the needs

Received 1 April 2016; revision received 19 September 2016; accepted for publication 21 September 2016; published online 22 November 2016.

*Postdoctoral Research Fellow, Department of Aerospace Engineering, 1320 Beal Avenue.

†James E. Knott Professor, Department of Aerospace Engineering, 1320 Beal Avenue.

of a particular problem, such as necessity in the exact quantization of a product's final state, accurate treatment of interference effects, importance of multidimensional tunneling effects, and so on. Without providing further discussion on this matter, one should note that there are only a few alternatives to the QCT method when attempting to resolve all possible rovibrational state-specific cross sections at high kinetic energies with sufficient statistical accuracy. On the other hand, it is worth mentioning that the QCT method fails to provide accurate results at some conditions [42]. This occurs due to quantum effects, such as tunneling and complex phase accumulation [42]. Recently, a significant difference in O_2–Ar vibrational relaxation times, obtained via quasi-classical and quantum methods was demonstrated at temperatures below 3000 K [44]. In the present work, O_2–N_2 RCs, obtained via the QCT, are compared with semiclassical calculations [45]. These results indicate that the quasi-classical propagation of trajectories for these species should be treated with caution as well.

The QCT method for three (atom–diatom) and six (diatom–diatom) degrees of freedom yields 12 and 18 Hamiltonian equations, when recognized that the center of mass is a cyclic coordinate and the momentum conjugate to that coordinate is a constant of motion. These numbers can be reduced to 8 and 14 by applying the conservation law of total energy and total angular momentum. However, this would considerably complicate the mathematical formulation of the governing equations. On the contrary, the semiclassical (SC) coupled approach, proposed by Billing [38], involves additional time-dependent Schrödinger equations, for which the number is proportional to the number vibrational states involved in a trajectory simulation. At hypersonic temperatures, when the population of all vibrational states must be captured, such a method becomes computationally intractable.

Details of the QCT method, adopted in the present work, are given elsewhere [20,44]. In summary, each trajectory is initialized by explicit assignment of initial vibrational and rotational quantum numbers and collision energy. This was done to allow for a flexible analysis of state-specific transitions during subsequent kinetic modeling. Other variables, such as impact parameter, orientation angles, and vibrational phase, are sampled randomly. The number of trajectories in each batch varies between 1000 and 10,000. The statistical uncertainty of most RCs is less than 15%.

Table 1 presents a summary on available databases of state-resolved O_2 chemistry [46,47]. These databases have been generated using the QCT method on PESs of different fidelity. For all three atom–molecule systems, listed in Table 1, the computational time reflects the amount of resources required to resolve the cross-sectional data for all possible precollisional rovibrational states. In the case of O_2–N_2, such calculations are intractable. Instead, simulations are performed for 160 pairs of initial vibrational states of oxygen and nitrogen with the initial rotational state sampled according to the Boltzmann distribution at $T_r = 10{,}000$ K. The number of trajectories reflects the size of database for each pair of species.

The O_2–Ar system employs the pairwise analytical PES. These calculations have demonstrated sufficient accuracy due to the closed-shell electronic configuration of the projectile species. The simulations of O_2–O and O_2–N systems use well-tested semi-empirical and ab-initio PESs by Varandas and Pais [17] and Sayós et al. [48], respectively. One can notice that the utilization of a semi-empirical PES does not necessarily lead to a lower computational cost of the QCT method, compared with the analytical fit to the ab-initio data. Lastly, the present paper focuses on O_2–N_2 collisions using the latest available PES by Varga et al. [31]. This study is in progress and results are reported only for selected vibrational states.

An extensive overview of three- and four-body QCT methods is given elsewhere [42,49]. The present paper concentrates on kinetic models of hypersonic flows and provides discussion on utilization of the QCT data. The primary tool for analysis of state-specific RCs is the system of master equations. The general appearance of the kinetic model that includes the bound–bound and bound–free (dissociation and tunneling) processes is given by Eq. (1):

$$\frac{\mathrm{d}n_i}{\mathrm{d}t} = \sum_{i' \neq i} (K_{i' \to i} n_x n_{i'} - K_{i \to i'} n_x n_i) - D_i n_i n_x + R_i n_O^2 n_x - T_i^f n_i + T_i^b n_O^2, \quad i = 1, \ldots, N \tag{1}$$

where n_i is the population of the i rovibrational state, $K_{i' \to i}$ is the rate of transition from i' to i rovibrational states, n_x is the number density of the collision partner of the O_2 molecule, D_i and R_i are the state-specific dissociation and recombination rate coefficients of the i state, T_i^f and T_i^b are the forward and backward tunneling rate coefficients, and N denotes the total number of rovibrational states. The summation in Eq. (1) is performed over the entire rovibrational ladder. The principle of detailed balance is invoked to generate rates of endothermic transitions to reduce the statistical error of the QCT method.

The rates of bound–bound and bound–free transitions can be averaged over the range of transrotational temperatures, because this type of thermal equilibrium is typically observed in gas flows with temperatures below 10,000 K. The system of master equations that employs rotationally averaged RCs is termed as the VT model. Otherwise, when a complete set of rovibrationally resolved RCs is used, the system of master equations is termed the RVT model.

The state-resolved approach becomes prohibitively expensive with increasing number of diatomic species and dimensionality of the problem. Although reduced-order models that retain the main features of the state-resolved approach have been proposed recently [50], the multitemperature (MT) model remains popular due to its simplicity. The solution of master equations provides new insight on parameters that are used in MT models. The present paper addresses the question of efficient utilization of the master equation results. The MT model, when formulated for simple heat bath conditions, consists of the following equations:

$$\begin{cases} \frac{\partial(\rho e_v)}{\partial t} = \rho_{O_2} \frac{e_v^\star - e_v}{\tau_v} + \dot{\omega}_{O_2} C_{DV} D_e \\ \dot{\omega}_{O_2} = R n_O^2 n_x - D(T_a) n_{O_2} n_x \end{cases} \tag{2}$$

In Eq. (2), e_v and $e_v^\star$ are the O_2 vibrational energy evaluated at T_v and T, respectively, ρ and ρ_{O_2} are the density of the O_2–O mixture and partial density of O_2, D_e is the classical dissociation energy, τ_v is the vibrational relaxation time, and $\dot{\omega}_{O_2}$ is the rate of O_2 generation. According to Park's model [51], the forward RC is computed using the governing temperature $T_a = \sqrt{T T_v}$. The recombination RC is computed through the equilibrium constant K_{eq} using the curve fit parameters provided in [51]: $R = D(T_a)/K_{eq}(T)$. The vibrational energy coupling coefficient C_{DV} corresponds to the loss of vibrational energy normalized by the classical dissociation energy. The system of Eq. (2) describes the transfer of vibrational energy assuming rotational equilibrium.

Lastly, one should discuss how the adjustable parameters, namely, τ_v, D, and C_{DV}, can be obtained from the system of master equations.

Table 1 Summary of QCT modeling effort

System	No. of states	Temperatures studied, K × 10^{-3}	No. of transitions	Computational time, h	Total no. of trajectories	Source
O_2–Ar	5117, $v_{max} = 36$	3–20	6.45 million	1.08×10^5	3.8×10^9	[44,46]
O_2–O	6245, $v_{max} = 46$	0.5–20	9.66 million	1.22×10^6	8.2×10^9	[20]
O_2–N	6136, $v_{max} = 43$	0.5–20	9.28 million	7.20×10^5	1.2×10^{10}	[47]
O_2–N_2	N_2 – 9141, $v_{max} = 53$; O_2 – 5945, $v_{max} = 35$	1–10	In progress	4.32×10^5	1.4×10^8	Present

The vibrational relaxation time, when the complete set of state-specific RCs is available, is obtained by the e-folding method [52]. When such a set of RCs is not available, the relaxation time can be derived from the rate of monoquantum deactivation from the first excited vibrational state, as is done for the O_2–N_2 system in the present work. This relaxation parameter does not account for the contribution of multiquantum jumps and excited vibrational states, for which the relaxation is usually faster than that for $v = 1$.

The dissociation RC, measured in shock-tube experiments, should be referred to as the quasi-stationary dissociation RC. Vibrational thermalization at the moment of onset of dissociation is incomplete, and the QSS dissociation RC is lower than the RC estimated at thermal equilibrium conditions. Hence, it is necessary to reevaluate the QSS dissociation RC as if the vibrational ladder is populated at $T_v = T$. According to Shatalov [53], D^{QSS} and D^{eq} are related through the following empirical relation:

$$D^{\mathrm{QSS}} = D^{\mathrm{eq}} \frac{T}{T_v} \exp\left(\frac{\tilde{D}}{RT}\left(\frac{1}{T} - \frac{1}{T_v}\right)\right) \tag{3}$$

where parameter $\tilde{D} = D_e - \beta RT$ describes the average loss of vibrational energy due to dissociation. The recommended range of β is between one and two, and in the present work, β is set to 3/2.

The average loss of internal energy C_{DV} is estimated as a product of the state-specific dissociation and recombination RCs and the instantaneous populations of corresponding vibrational states [6]. The master equation approach generates time-dependent profiles of C_{DV} that can be used to improve the accuracy of the conventional MT approach in which a constant value of C_{DV} is assumed throughout the relaxation process.

III. Results

A. O_2–O

The interaction of the oxygen molecule with the parent atom is important, not only for the kinetics of hypersonic flow, but also in the chemistry of the upper atmosphere. Although ozone is present only in trace amounts, the strong absorptive properties of harmful UV radiation serve as motivation for the extensive study of ozone during the last several decades [1]. Because this type of interaction involves open-shell electrons, a rigorous quantum-mechanical treatment of the O_3 complex presents a great challenge. One of the main problems associated with the study of O_3 electronic structure is the presence of a potential barrier in the entrance/exit channel of the O_2–O collision. The existence or absence of such a reef structure is known to be responsible for the negative temperature dependence of rates at room temperatures. Although extensive quantum-mechanical studies of ozone in the ground electronic state indicate the existence of a small potential barrier, the trajectory studies using PESs that include such a barrier underestimate experimental rates. When the potential barrier is artificially removed, the experimental data are reproduced accurately. On the other hand, the semi-empirical PES by Varandas and Pais, obtained by the double many-body expansion method [17], has no potential barrier. Rates, obtained on the Varandas and Pais PES, match the experimental data quite accurately. For this reason, the Varandas and Pais PES was used recently to generate a complete set of state-specific transition rates for each internal energy level of oxygen at temperatures between 500 and 20,000 K [20,21]. In this section, the results of the master equation study of this system are reviewed and compared with the widely adopted multitemperature models.

1. *Vibrational and Rotational Relaxation Times*

Experimental investigation of oxygen vibrational relaxation in collisions with atomic oxygen was performed for room temperatures [54,55] as well as at moderate hypersonic temperatures between 1000 and 3500 K [56,57]. These data are summarized in Fig. 1, along with the computed vibrational and rotational relaxation times. These parameters are obtained from the solution of master equations coupled to the set of state-specific rates. In the presence of rotational equilibrium, the VT thermodynamic model provides τ_v, given by a solid line in Fig. 1. The RVT model gives τ_v and τ_r, shown by dashed and dashed-dotted lines in Fig. 1. For reference, the Millikan–White (MW) [58] vibrational relaxation time, with parameters obtained by Park [59] by fitting to the measurements by Kiefer and Lutz [57], is shown by the dashed-dotted line. Error bars of QCT results are less than the symbol size.

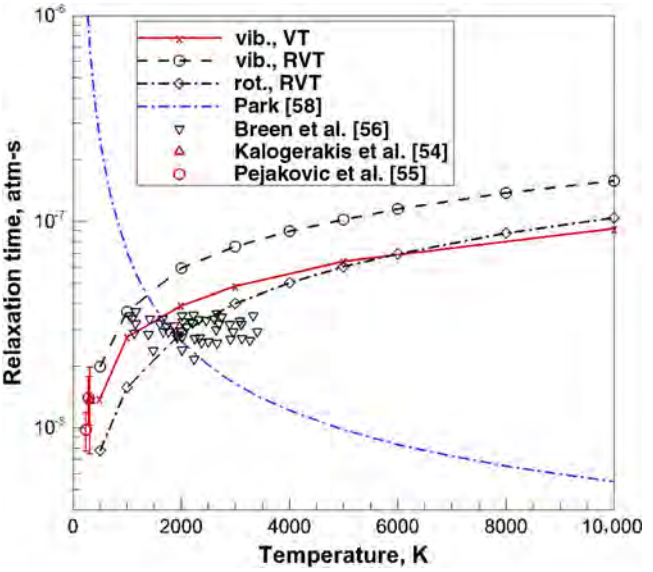

Fig. 1 Vibrational and rotational relaxation times if O_2–O collisions.

Experimental data by Breen et al. [56] was obtained in a conventional shock tube with oxygen atoms generated by an RF discharge in either pure O_2 or an O_2/Ar mixture. Although this technique eliminated uncertainties arising due to ozone thermal decomposition, which serves as a source of oxygen radicals in the work by Kiefer and Lutz [57], Breen et al.'s data [56] are still much scattered. These measurements alone do not allow one to make a conclusion about agreement in temperature dependence of τ_v between QCT data and experiments. Nevertheless, measurements conducted by Pejaković et al. at room temperature [55] clearly indicate that O_2–O vibrational relaxation becomes less efficient with temperature, as predicted by the master equation simulations. The MW τ_v fails to describe the rapid relaxation at low temperatures. This is due to the inapplicability of the Landau–Teller theory to molecular systems that form metastable chemical bonds. Although the question of existence of a barrier in O_3 is not completely settled, the presence of a subtle repulsion in the O_3 entrance/exit channel should have a minor influence on τ_v at temperatures relevant to hypersonic flows.

The vibrational relaxation time in the RVT model is larger than that in the VT model due to the presence of significant rotational nonequilibrium in the considered temperature range. Typically, τ_r is assumed to be much shorter than τ_v at low to moderate hypersonic temperatures [60]. This is not the case for thermalization of internal modes that occurs only via O_2–O collisions. In fact, if only O_2–O collisions are considered to contribute in relaxation, the rotational and vibrational modes should be treated simultaneously because τ_v and τ_r, obtained via the RVT model, are different by a factor of 2 at maximum. In experiments by Breen et al. [56], the molar fraction of atomic oxygen did not exceed 1.84%, hence the effect of O_2–O rotational nonequilibrium should be minimal under these conditions.

Because thermal relaxation and dissociation occur at different timescales, it is possible to consider these two phenomena separately when modeling nonequilibrium chemical reactions at moderate temperatures. However, as temperature increases, the dissociation may start before the complete thermalization of the rovibrational ladder. The complete set of O_2–O QCT transition rates supplemented by the O_2–O_2 set of forced harmonic oscillator (FHO) transition rates was used previously to model vibrational relaxation in shock waves at velocities between 3.07 and 4.44 km/s [61]. These simulations were motivated by recent experimental measurements of laser absorption

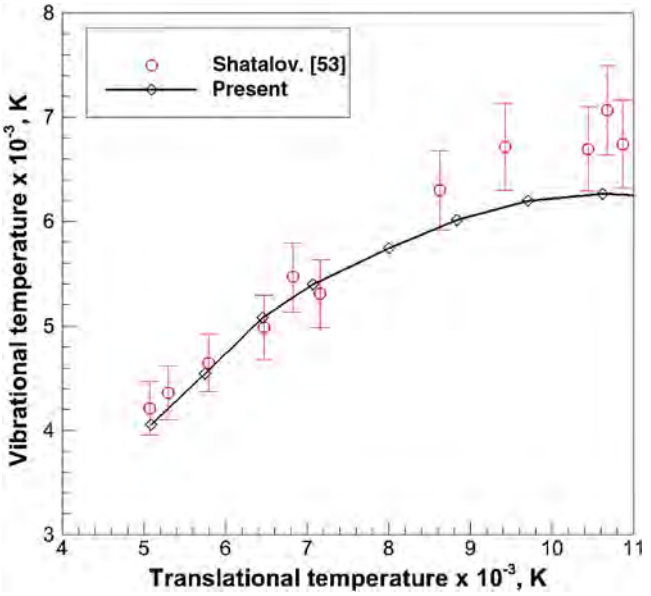

Fig. 2 Variation of vibrational temperature behind the shock front with T.

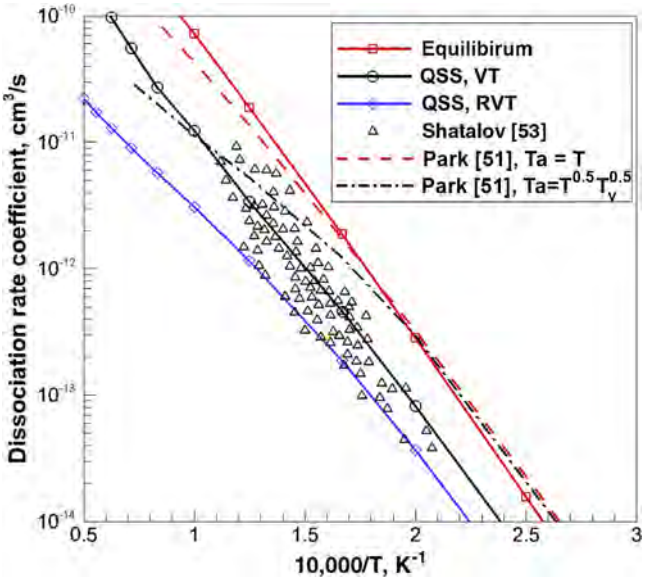

Fig. 3 Equilibrium and QSS dissociation RCs in O_2–O collisions.

in the Schumann–Runge (SR) bands [62]. In these experiments, the absorption of laser radiation at several wavelengths between 230 and 260 nm was interpreted in terms of translational and vibrational temperatures of the nonequilibrium gas. Bound–bound and bound–continuum transitions from ${}^3X_g^-$ to $B^3\Sigma_u^-$ state were considered for all vibrational states, assuming a Boltzmann population of energy levels [63]. One should note that, due to the multitemperature assumption used in [63] to estimate the absorption coefficient, the comparison of experimental data and the state-to-state (STS) model should be done with caution.

The vibrational temperature observed before the onset of dissociation is shown in Fig. 2. The horizontal scale corresponds to the maximum of translational temperature, registered immediately after the shock wave arrives at the optical station. At moderate nonequilibrium conditions, the state-resolved model predicts the vibrational temperature during the quasi-steady regime quite accurately. As temperature increases further, the present model slightly (200–500 K) underestimates the measurements. The disagreement may be caused by uncertainties in the experimental approach related to the non-Boltzmann population of vibrational states as well as due to inaccuracies of the FHO model used to describe O_2–O_2 collisions. It is highly desired to repeat the calculations conducted in [61] when a complete set of O_2–O_2 RCs generated on accurate PESs become available.

2. *Dissociation Rate Coefficient*

The master equation approach provides a time-dependent evolution of the rovibrational distribution. It is possible to define a dissociation rate that takes place during the QSS phase (i.e., when the condition $d\varepsilon_v/dt = 0$ is held). Because the experimental measurements can only access a depletion rate during the QSS phase, the similar result from the master equation simulation is of great importance because it allows direct comparison between theory and experiment.

The QSS dissociation RC for O_2–O collisions is shown in Fig. 3. Three curves with square, circular, and diamond symbols represent RCs estimated under thermal equilibrium conditions (i.e., when $T = T_v = T_r$), as well as during the QSS phase using the VT and RVT models, respectively. For comparison, the experimental measurements are shown by triangular symbols. Also, the Park [51] dissociation rate coefficient D_{Park} is shown by a dashed-dotted line. These data are obtained by computing an effective temperature $T_a = \sqrt{TT_v}$, where vibrational temperature is taken during the QSS phase from heat bath simulations, accounting for both O_2–O and O_2–O_2 collisions [64].

At low translational temperatures, when the QSS vibrational temperature reaches equilibrium conditions, D_{Park} and D_{eq} RCs are in good agreement. However, the QSS dissociation RC is substantially lower than the equilibrium RC. This is because vibrationally excited states that contribute to the dissociation are underpopulated compared with the equilibrium distribution at given T_v. This can be clearly seen from Fig. 4. The cumulative sum of dissociation probability, computed as the product of state-specific population and the corresponding dissociation RC, significantly depends on the contribution of excited vibrational states. The deviation from equilibrium population can be observed for $v > 15 \times (e_v = 2.4$ eV). These states contribute more than 60% in the dissociation probability function. Thus, the depletion rate, computed at the vibrational temperature of the QSS phase, overestimates the actual dissociation rate.

The Park [51] dissociation RC, estimated at T_a, is noticeably higher than the QSS RC at temperatures below 8000 K. At higher temperatures, the Park [51] RC fits the upper interval of experimental data, however, agreement with the QSS VT RC is not achieved. The following section shows that the use of the QSS dissociation RC without traditional coupling by means of T_a produces accurate results when incorporated in the MT model.

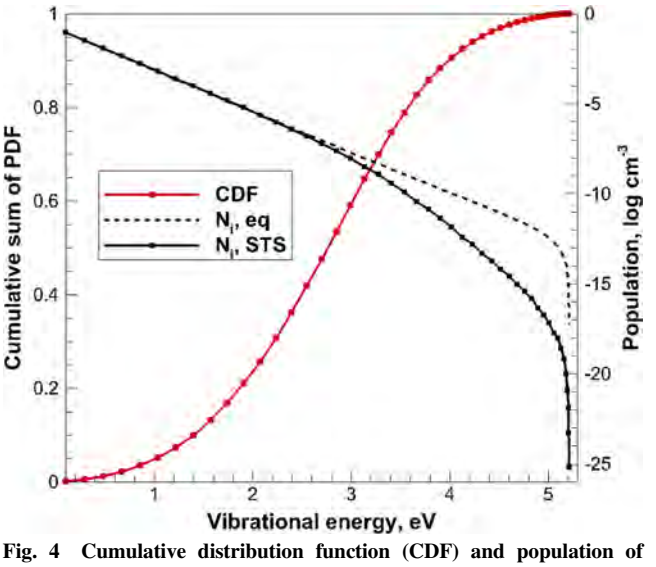

Fig. 4 Cumulative distribution function (CDF) and population of vibrational ladder during the QSS phase, $T = 5000$ K (PDF, probability distribution function).

3. Comparison of State-to-State and MT Methods

Because of the high cost of the STS approach, there is a potential interest to use the information about nonequilibrium populations and state-specific rates to improve the accuracy of the simple and efficient MT approach. In the present work, the solutions from the STS and MT models are compared side-by-side for an ideal heat bath of oxygen at translational temperatures of 5000; 8000; 10,000; and 14,000 K. There are three primary parameters that can be adjusted to fit the solution of the MT approach to that of the STS method. Namely, these are the vibrational relaxation time, dissociation rate coefficient, and the average loss of internal energy due to dissociation. It was shown recently [20] that the O_2–O e-folding relaxation time accurately describes the evolution of vibrational energy when incorporated in the Landau–Teller (LT) equation. Therefore, it is decided to keep the LT term and vibrational relaxation time unadjusted.

The appropriate adjustment of dissociation RC and vibration–dissociation coupling in the MT model parameter should be based on the temporal evolution of these parameters during thermalization. In heating flows, the rate of dissociation is often much larger than the rate of recombination, especially at early stages of thermalization. It is possible to neglect the recombination and define the macroscopic instantaneous dissociation RC in the following manner:

$$D^{\text{inst}} = \frac{\dot{\omega}_{O_2}}{n_{O_2} n_O} \tag{4}$$

The O_2–O instantaneous and QSS dissociation RCs and the vibration–dissociation coupling parameter are shown for considered heat bath conditions in Figs. 5 and 6. In Fig. 5, the symboled lines correspond to the instantaneous RC computed as the ratio of difference in the O_2 number density and the time step, whereas dashed lines correspond to D^{QSS}. At low temperatures, the maximum of D^{inst} corresponds to the plateau at the QSS level. At higher temperatures, the QSS assumption breaks down and the QSS RC is bounded by some minimal and maximal values of instantaneous RCs, shifting toward the lower bound with increasing temperature. In fact, the differences between the minimum and maximum of instantaneous RCs becomes smaller at higher temperatures. One should note that Eq. (4) allows for zero dissociation RCs, which is, of course, unphysical. However, the rapid drop of D^{inst} is observed only after the QSS phase when a system is nearly at complete equilibrium, and so it is of little significance.

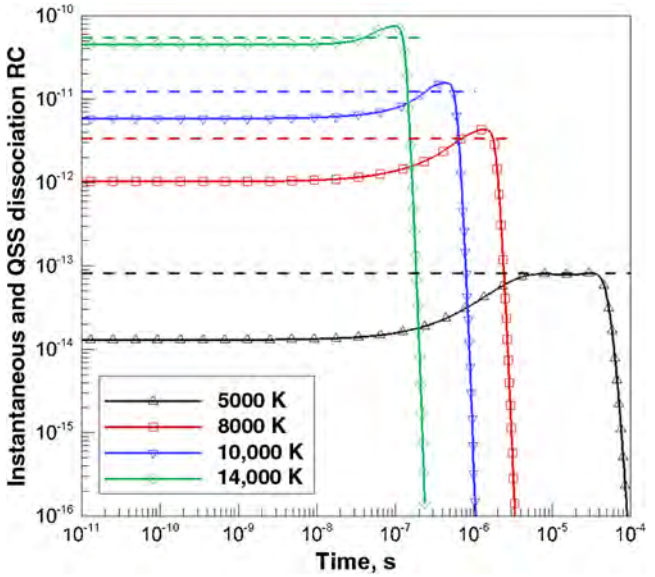

Fig. 5 Instantaneous and QSS dissociation RCs in O_2–O collisions; solid lines describe RC obtained via Eq. (4) and dashed lines correspond to QSS RC.

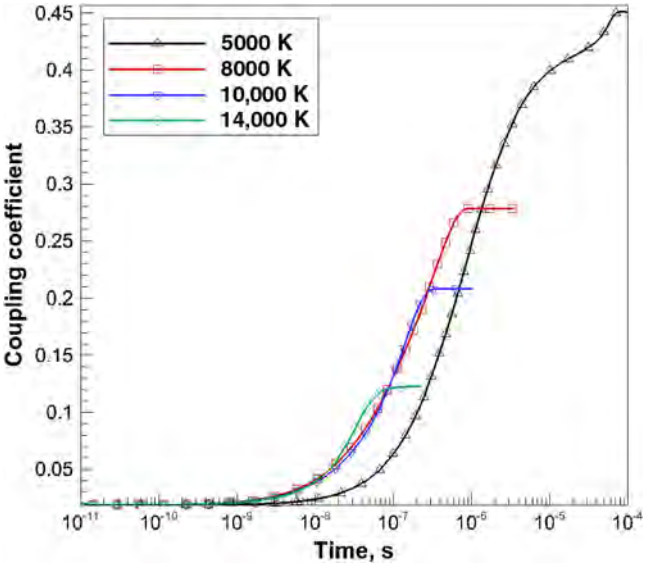

Fig. 6 Vibration–dissociation coupling parameter in O_2–O collisions.

Because little to no dissociation occurs at low temperatures before the QSS phase, it will be appropriate to assume $D(T_a) = D^{\text{QSS}}$ in the MT model. At higher temperatures, the dissociation occurs simultaneously with thermal relaxation, hence, again, it will be accurate to assume the QSS RC as the replacement for the actual dissociation RC in Eq. (2). The most pronounced inaccuracy in the modified MT model will be observed for intermediate temperatures.

Figure 6 illustrates that it is incorrect to assume a constant C_{DV} throughout the entire relaxation process. In fact, this coupling parameter has initially a very small value reaching a nearly constant level during the QSS phase and thereafter. For the sake of simplicity, a linear dependence of C_{DV} on T_v can be proposed:

$$C_{\text{DV}} = C_{\text{DV}}^{\text{QSS}} \times \min\left(\frac{T_v}{T_v^{\text{QSS}}}, 1\right) \tag{5}$$

where $C_{\text{DV}}^{\text{QSS}}$ and T_v^{QSS} are the vibration–dissociation coupling parameter and vibrational temperature during the QSS phase [20,62]. The comparison of the STS method and standard MT approach with dissociation rate, computed according to [51], was previously reported in [20] for temperatures of 5000 and 10,000 K. The comparison of STS, standard, and modified MT approaches is shown in Fig. 7 for translational temperatures of 5000; 8000; 10,000; and 14,000 K. The modified MT approach performs very adequately, compared with the standard MT model. As expected, the least successful agreement is observed for moderate temperatures.

B. O_2–N

The interaction of the oxygen molecule with nitrogen atoms is important in shock-heated air, the chemistry of the upper atmosphere, and the combustion of carbon-based fuels. The formation of nitric oxide in these applications occurs via the Zeldovich mechanism. However, the O_2–N nonreactive channel of the interaction can also be important in modeling flows with a large number of nitrogen atoms. State-specific data on O_2–N collisions become necessary when developing high-fidelity thermochemistry models of nonequilibrium hypersonic flows. Meanwhile, O_2–N collisions are known to occur on multiple PESs of different multiplicity [48]. The lowest $2A'$ PES has a relatively low potential barrier of approximately 0.3 eV and a deep potential minimum that corresponds to $NO_2(X^2A_1)$. To the authors' knowledge, a model of oxygen relaxation in collisions with nitrogen atoms has not been proposed previously.

The experimental study of the O_2–N system is complicated due to the large difference in dissociation energies of oxygen and nitrogen molecules. The presence of fast chemical reactions involving nitric oxide also complicates measurements of the vibrational distribution

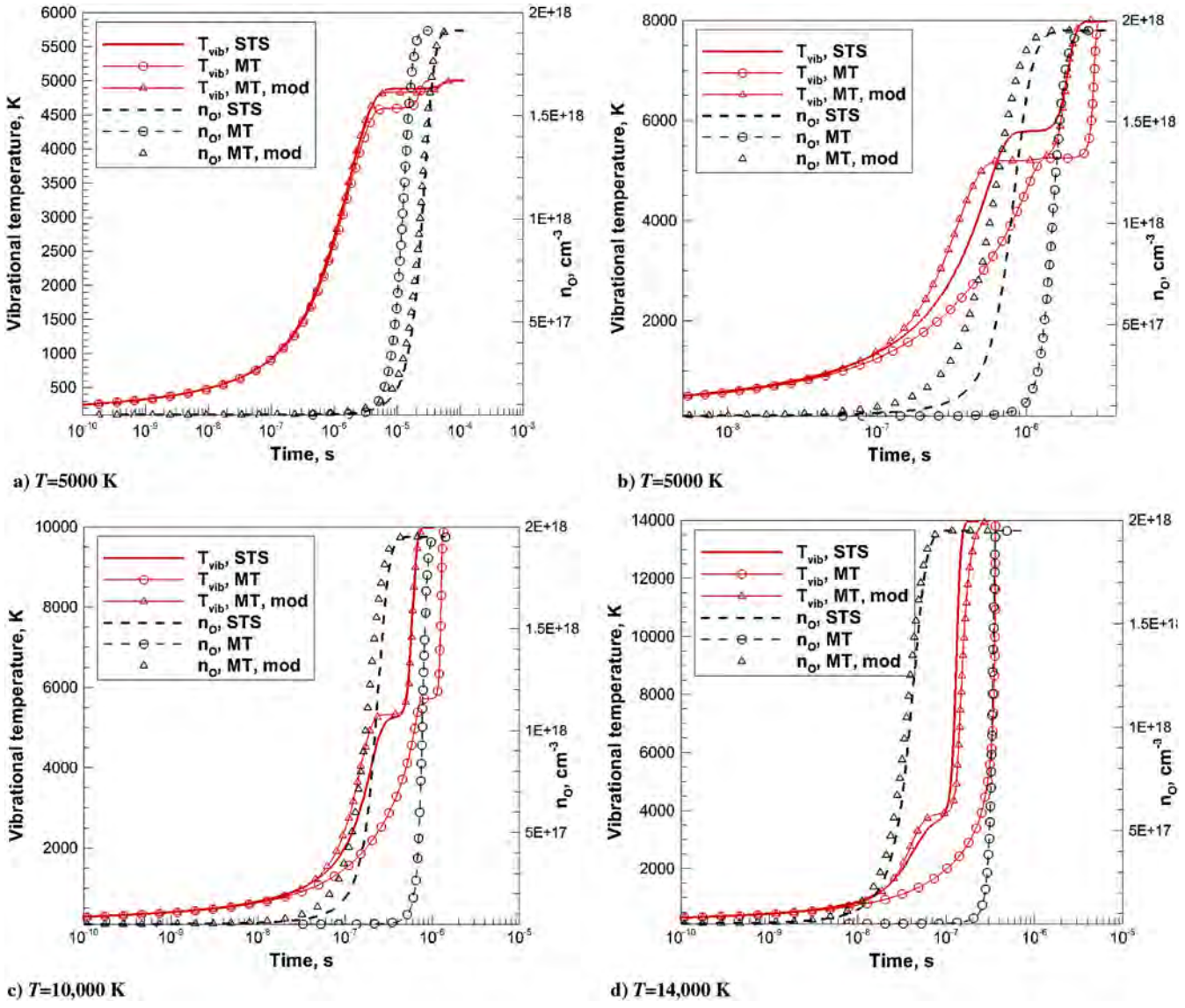

Fig. 7 Comparison of STS and modified MT approaches.

of products. As a result, experimental data on oxygen relaxation in O_2–N collisions are absent. To overcome this difficulty, an equality of relaxation times in O_2–N and N_2–O collisions has been assumed in computational models of hypersonic flows [65]. Although this assumption can be partially justified due to the similar masses of reactants, state-to-state reaction rates are desirable for the implementation of more accurate state-resolved models of hypersonic flows.

The O_2–N vibrational and rotational relaxation times, obtained via the solution of master equations, are shown in Fig. 8. For reference, the experimental data for the N_2–O system [66–68] are shown by symbols. Eckstrom [66] and Breshears and Bird [68] used thermal decomposition of ozone in shock-tube experiments. In the former work, carbon monoxide was used as a tracer of vibrationally exited nitrogen due to fast energy exchange between these two species. The later work adopted a laser schlieren technique, similar to [57], to derive the relaxation time from the postshock density gradient. The main source of uncertainty in these works comes from the presence of impurities and from the ozone decomposition stoichiometry. The data by Eckstrom [66] was estimated to have 50% uncertainty. At lower temperatures, McNeal et al. [67] used a photoionization detector to measure the rate of vibrationally excited nitrogen in the afterglow. All these works have reported much faster relaxation of nitrogen compared with the Landau–Teller theory, which was

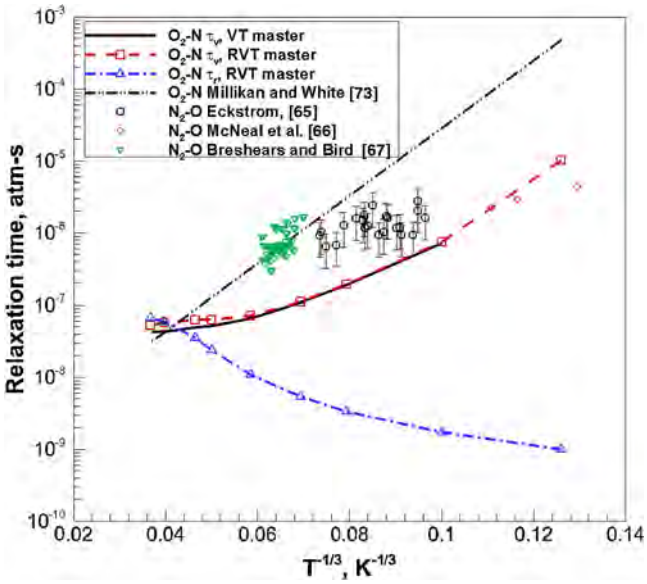

Fig. 8 Vibrational and rotational relaxation times in O_2–N and N_2–O collisions.

attributed to the presence of chemical effect in the metastable N_2O complex.

As one can see, the present QCT results for O_2–Nτ_v lay lower than N_2–Oτ_v. The Millikan–White [58] correlation provides a substantially higher estimation of τ_v as well, indicating that, in O_2–N collisions, the chemical effect may also be important. Because the experimental approach disregarded the presence of rotational nonequilibrium, the measurements should be compared with the results of the VT model. Unlike in O_2–O collisions, rotational thermalization in O_2–N occurs more rapidly than vibrational relaxation up to 8000 K. Hence, the assumption of rotational equilibrium is valid at lower temperatures.

Thermal equilibrium and QSS dissociation RCs in O_2–N collisions are shown in Fig. 9. For reference, the previously recommended two-temperature dissociation RC [59] is shown by symbols. The previous O_2–N dissociation RC [51] is simply assumed to be equal to the O_2–O RC, because there is no experimental data available for the former molecular system. In the present work, the Park [51] O_2–N RC is estimated at T_a, calculated using the QSS vibrational temperature of the O_2 rovibrational manifold in a heat bath of nitrogen atoms [47]. Similar to O_2–O collisions, the Park [51] dissociation RC overestimates the QSS depletion RC, given by solid and dashed-dotted lines for the RVT and VT models. This is due to incomplete thermalization of the ladder during the QSS phase, even at low temperatures of the heat bath. The Park [51] RC is also higher than the equilibrium RC, derived in the present study, indicating that the dissociation in O_2–O collisions proceeds more efficiently than in the O_2–N system. Unlike in O_2–O collisions, the difference in QSS VT and RVT RCs is quite small for low temperatures. This is due to the effect of nearly complete rotational equilibrium that occurs before the onset of dissociation. As expected, the difference between $D_{\mathrm{QSS}}^{\mathrm{RVT}}$ and $D_{\mathrm{QSS}}^{\mathrm{VT}}$ increases at high temperatures.

The instantaneous dissociation RC, computed from Eq. (4), is shown in Fig. 10 for temperatures of 5000; 8000; 10,000; and 14,000 K, along with the QSS dissociation RC, previously reported in [47]. As in the case of O_2–O collisions, the O_2–N instantaneous dissociation RC is not constant throughout the relaxation, due to varying state-specific dissociation RCs of different energy levels and evolving rovibrational distribution in time. D^{inst} levels off with D^{QSS} at temperatures as high as 10,000 K, whereas in O_2–O collisions, this occurs at 5000 K. The difference between minimal and maximal instantaneous RCs for the O_2–N system is significantly larger than for the O_2–O system. For instance, the O_2–O instantaneous RC increases between 1.22 and 6.1 times during relaxation in the range of temperatures between 5000 and 14,000 K. For O_2–N, this increase is between 2.07 and 20.69 times for a similar temperature range. This can be attributed to the efficient "scrambling" of precollisional states in O_2–O and the large probability of exchange reaction even for low-lying vibrational states. As was discussed previously [1], this type of interaction is due to the small O_3 potential barrier. The exchange reaction in O_2–N collisions leads to products other than reactants and does not contribute to the relaxation of oxygen.

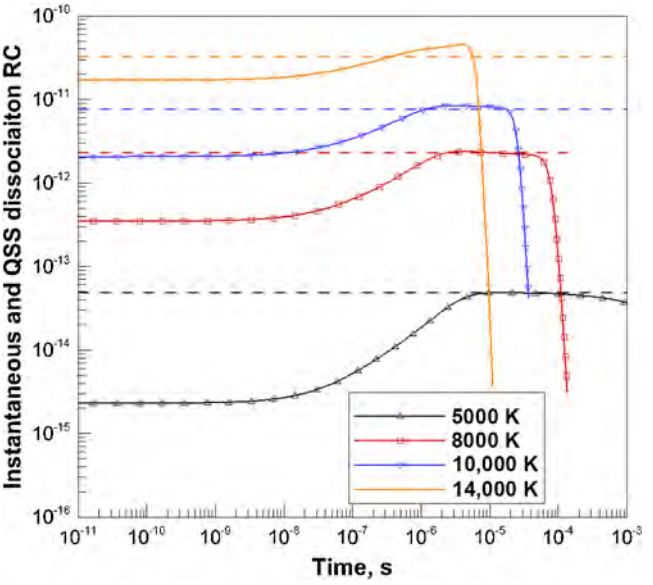

Fig. 10 Instantaneous and QSS dissociation RCs in O_2–N collisions.

The simple use of the QSS RC in the O_2–N MT model, as was done for O_2–O, would lead to an overestimation of the actual RC. To accurately match the solution of master equations, the dissociation RC in the MT model should be modified. From the temporal evolution of instantaneous RCs, one can see that it varies between $D_{\min}$ and roughly D_{QSS}, rapidly increasing at some vibrational temperature that is below the QSS T_v. The following factor accounts for the variation of RCs due to nonequilibrium population of the vibrational ladder:

$$\psi = (D_{\mathrm{QSS}} - D_{\min})\left[\frac{1}{\pi} a \tan\left(\alpha\left(1 - \frac{T_v^0}{T_v}\right)\right) + \frac{1}{2}\right] + D_{\min} \qquad (6)$$

Similar to Eq. (6), the nonequilibrium factor was proposed in [69] for a mixture of N_2 and N. In the original work by Valentini and Schwartzentruber [69], the lower bound of ψ is set to zero. In the present work, the effect of initial dissociation that may take place at high temperatures before the QSS phase is taken into account by limiting the lowest value of ψ at $D_{\min}$ level. In fact, $D_{\min}$ does not depend on the number density of O_2 or N and is defined only by T and T_v. For the variation of initial vibrational temperature T_v between 100 and 1000 K, it is found that $D_{\min}$ varies not more than 10%. The adjustable parameter that triggers dissociation T_v^0 should be chosen for each molecular species individually. For oxygen, in the present work, it is set to 3000 K. The parameter of steepness α is set to two.

The number density of atomic oxygen and T_v, generated by the STS, conventional, and modified MT models are shown in Fig. 11. Indeed, the modification of the MT model with Eq. (6) significantly improves the agreement in species number density at lower temperatures, compared with the standard MT approach. At higher temperatures, the composition is similar for the modified MT and STS methods because the variation of the instantaneous RC is relatively small and the actually RC is quite close to D^{QSS}. Overall, the modification of C^{DV} and D^{QSS} reflected in Eqs. (5) and (6) substantially improves the quality of the MT solution when compared with the reference STS approach.

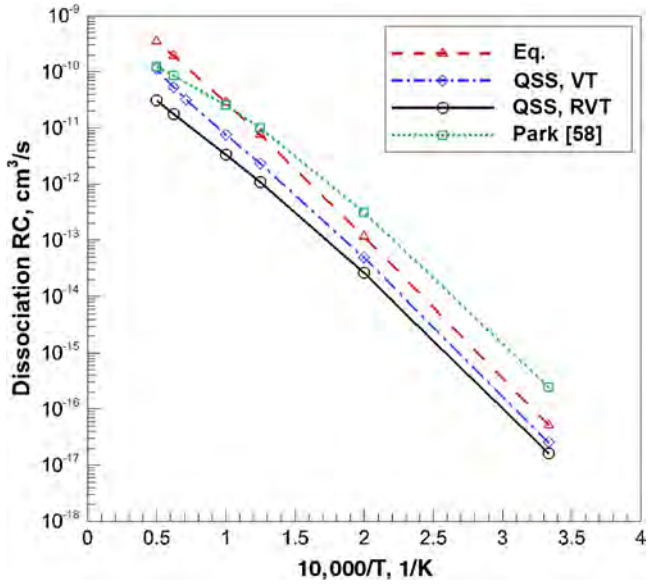

Fig. 9 Thermal equilibrium, QSS VT and RVT dissociation RCs in O_2–N collisions.

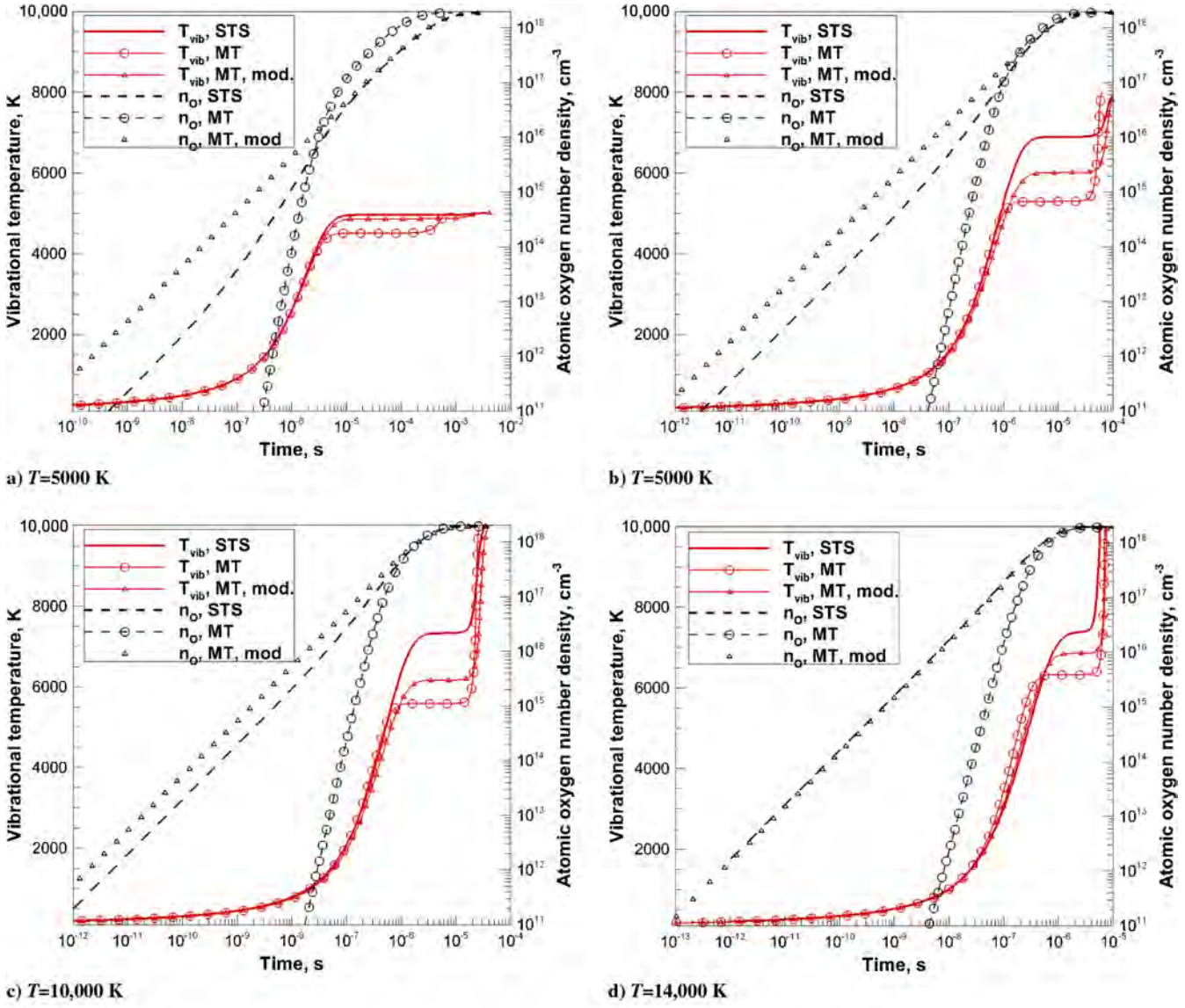

Fig. 11 Comparison of STS and modified MT approaches for O_2–N heat bath simulation.

C. $O_2 - N_2$

The interaction of O_2 with molecular nitrogen is of great importance in hypersonic thermochemistry due to the large difference in the dissociation energy of these species. There are several PESs in the literature that describe the N_2O_2 system. One of the first N_2O_2 PESs was proposed by Aquilanti et al. [2] for studying rigid molecules in their ground vibrational state. This PES was designed specifically for methods of molecular dynamics for the upper atmosphere, however, it has a little use for aerothermodynamics. Bartolomei et al. [70] recently published an improved ab-initio PES with similar restrictions. The VT and VV energy transfer was studied by a semiclassical coupled method by Billing on an empirical PES in the range of temperatures between 250 and 1000 K [26]. Recently, Garcia et al. [45] reported VT and VV rate coefficients using an improved PES for selected vibrational states of oxygen at temperatures up to 7000 K. This PES is based on ab-initio calculations that are interpreted as a combination of bond–bond interactions, namely, van der Waals and electrostatic interaction terms. Unfortunately, the dataset reported in [45] is incomplete and, thus, a master equation simulation still cannot be performed.

An analytical fit to the global ab-initio PES of triplet N_2O_2 was recently published by Varga et al. [31]. This PES was obtained by multistate complete-active space second-order perturbation theory and was specifically designed to describe collisions at high kinetic energies. Most of the multireference calculations of electron correlation energy were conducted in the range of potential energies between 100 and 350 kcal/mol (76% of the total 54,889 data points). It is worth noting that the long-range forces are not described correctly in this PES, thus it may not be suitable for low energy collisions. The following section compares the rate coefficients, generated by trajectory simulations on this PES, with the existing theoretical and experimental data.

1. *VT and VV Rate Coefficients*

Rates of VV and VT energy transfer for $O_2(v = 25)$ were computed by Garcia et al. [45] on two PESs of different fidelity using the SC and QCT methods. In the present work, rate coefficients in [45] are compared with those obtained by the QCT method on the PES of Varga et al. [31]. The VT reaction corresponds to the mono- and double-quantum deactivation of oxygen with nitrogen remaining in the same vibrational state. The VV reaction is described by O_2 monoquantum deactivation with the simultaneous single quantum activation of nitrogen. Rate coefficients of these processes are shown in Table 2.

The present QCT results agree better with the data, obtained on the Garcia et al. [45] PES, based on ab-initio data, than with the data generated using the simpler Billing [26] PES. This is observed for all three types of considered transitions. In fact, the Billing PES produces a systematic overestimation of rates, which may be

Table 2 Vibration-vibration and vibration-translation transition RCs in $O_2(v = 25) - N_2$, in cubic centimeters per second, at $T = T_r = 1000$ K

Source	Transition	Rate coefficient
QCT, Present	$O_2(v-1) + N_2(w)$	4.36×10^{-12}
QCT, Garcia et al. PES [45]	— —	2.3×10^{-12}
SC, Garcia et al. PES [45]	— —	1.1×10^{-12}
QCT, Billing PES [26]	— —	1.2×10^{-11}
SC, Billing PES [26]	— —	3.5×10^{-12}
QCT, Present	$O_2(v-2) + N_2(w)$	8.16×10^{-14}
QCT, Garcia et al. PES [45]	— —	1.1×10^{-13}
SC, Garcia et al. PES [45]	— —	6.0×10^{-14}
QCT, Billing PES [26]	— —	1.5×10^{-12}
SC, Billing PES [26]	— —	3.9×10^{-13}
QCT, Present	$O_2(v-1) + N_2(w+1)$	2.17×10^{-15}
SC, Garcia et al. PES [45]	— —	1.6×10^{-17}
SC, Billing PES [26]	— —	3.7×10^{-16}

explained by the fact that this PES is more repulsive than the Garcia et al. [45] ab-initio PES, and the attraction in N_2O_2 dimer configuration in the Billing PES is less pronounced. As expected, the rates of VT transition, generated in the present work, generally agree better with the results of QCT calculations than with the SC method.

The situation of energy transfer in collisions with oxygen in the ground vibrational states is drastically different. The VT and VV rates of energy exchange in $O_2(v = 0) + N_2(w = 1)$ are shown in Fig. 12. VV RCs correspond to the products $O_2(v' = 1) + N_2(w' = 0)$, whereas the VT RCs describe the production of $O_2(v' = 0) + N_2(w' = 0)$. Results of SC calculations by Garcia et al. [45] are shown by empty symbols. An empirical rate of VV transition, derived by Gilmore et al. [71] from experimental data on transition probabilities of the VV exchange reaction [72,73], is shown by long dashed curve. The experimental approach combines generation of spark interferograms with the following analysis of density profiles, as well as the measurements of infrared emission from CO at 4.6 μ of wavelength, used as a tracer for the N_2 population. The last fact can be justified taking into account the very close fundamental vibrational frequencies of N_2 and CO.

Two important conclusions can be derived from this comparison. First, the agreement between SC and QCT approaches is satisfactory only at temperatures higher than 3000 K. Below this temperature, the QCT method strongly underestimates the RC of VV and VT reactions, compared with the result of SC calculations. There are two possible explanations for this disagreement. First, the QCT and SC calculations were conducted on two different O_2N_2 PESs. Although the difference between these two methods in Table 2 is not as large as for the RCs involving $O_2(v = 0)$ in Fig. 12, only SC calculations on the PES given in [31] could provide an explanation for this difference.

Second, there is a possibility for the failure of the QCT method at low temperatures due to pronounced influence of quantum effects. Previously, it was shown that the QCT approach severely underestimates the RC of $O_2(v = 1)$ monoquantum deactivation in collisions with Ar at hypersonic temperatures [44]. These differences cannot be explained by statistical uncertainty of the results. Similar to O_2–Ar, the QCT method in the present work underestimates selected RCs compared with the SC method that adopts a quantal treatment of the vibrational mode.

Another important observation is related to the disagreement in VV RCs between the SC method and experimental data. This may be attributed to some uncertainties in the PES, used in [45], as well as to the theoretical interpretation of experimental data. Indeed, the analysis of interferograms in [72,73] was outlined assuming that the relaxation of nitrogen in the O_2–N_2 mixture can be represented as a superposition of two processes with different timescales. During a short period of time after the shock passage, oxygen quickly relaxes in collisions with N_2 and O_2 molecules via the VT energy transfer mechanism. After molecular oxygen receives a sufficient amount of vibrational energy from the translational motion of the particles, the energy exchange between N_2 and O_2 starts to play a role. Moreover, in experimental work by White [72], it was assumed that the VT process of N_2 excitation in collisions with oxygen is noticeably slower than the N_2–O_2 VV process, and the latter process should be responsible for the rapid excitation of N_2 in air relative to pure N_2.

The experimental data on vibrational relaxation time in pure oxygen are well known [58] and can be interpreted in terms of the monoquantum deactivation RC form $O_2(v = 1)$. Such data are shown in Fig. 12 with a dashed-dotted line. Indeed, the RC of monoquantum deactivation in pure O_2 is substantially higher than either VT or VV RCs in $O_2(v = 0) + N_2(w = 1)$ collisions obtained via SC and QCT methods. However, the RCs of O_2–N_2 VV transition by Gilmore et al. [71] is comparable to the relaxation RC in pure oxygen and do not comply with the hypothesis about the two-stage N_2 relaxation process in air [72]. Moreover, the RC of VT process, given by empty and filled triangles, is higher than the RC of VV process obtained via the trajectory simulation approach. This indicates that the MW correlation rule for N_2–O_2 collisions, used in [72] to solve for the VV exchange RC, may not be accurate enough for the analysis of the experimental data. Clearly, the most rigorous approach would consist of analysis of interferograms, obtained in [72,73] using the new RCs obtained on accurate PES by means of trajectory propagation methods accounting for quantum effects.

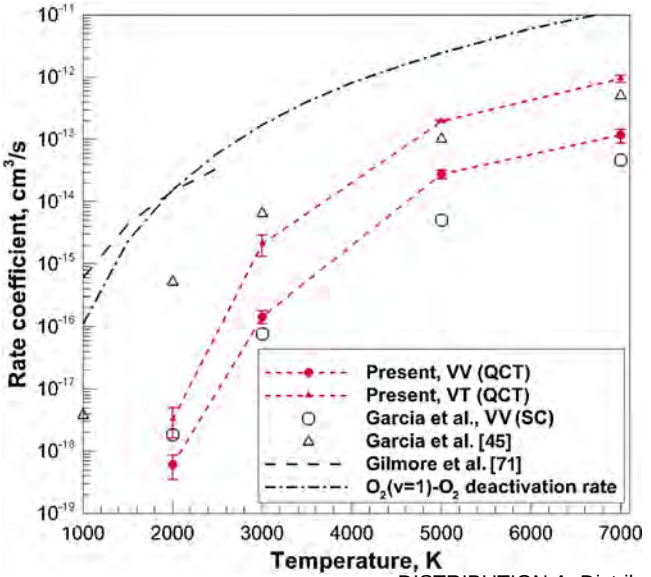

Fig. 12 Transition RCs of $O_2(v = 0) + N_2(w = 1)$ collision.

2. *Vibrational Relaxation and Dissociation of Oxygen*

Because the QCT method is quite accurate in describing the vibrational energy exchange at high translational energies, it can be used for comparison of vibrational relaxation time, derived from the rate of monoquantum deactivation from the first excited vibrational state with existing experimental data. The cross section of monoquantum deactivation, averaged at transrotational temperatures between 4000 and 10,000 K is shown in Fig. 13. The vibrational relaxation times, derived from the cross sections in Fig. 13, are shown in Fig. 14. The dashed line corresponds to the Millikan–White [58] relation with parameters estimated from the vibrational frequency of oxygen and the reduced mass of colliding particles. It is important to note that the MW curve is not obtained by fitting the general expression to experimental results. Circular symbols correspond to O_2 vibrational relaxation times in collisions with N_2 measured in air and in a 5%O_2–95%N_2 mixture by Generalov and Losev [74]. The red line describes the present O_2 relaxation time obtained on the PES by Varga et al. [31].

The experimental data by Generalov and Losev [74] indicates a slower vibrational relaxation time of oxygen in collisions with N_2, compared with the empirical equation by Millikan and White [58]. This overestimation is very modest and probably falls in the uncertainty interval of 15–30% as stated in the original work [74]. The present QCT results are closer to the data of Generalov and Losev [74]

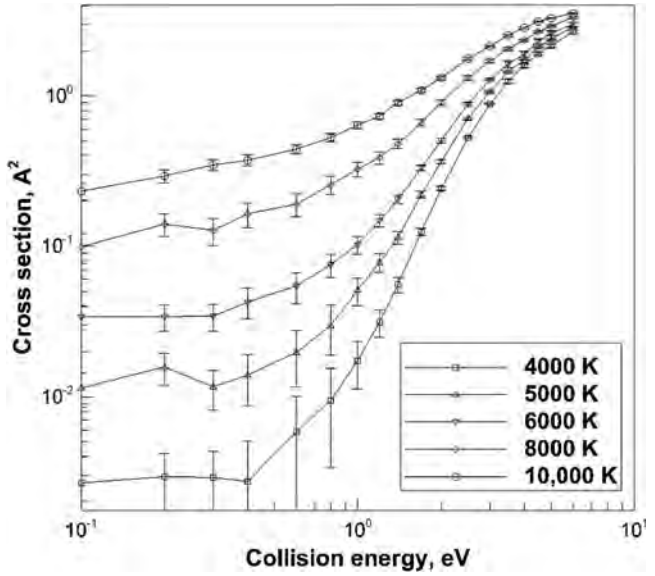

Fig. 13 Cross sections of $O_2(v = 1) - N_2$ monoquantum vibrational deactivation, $T = T_r$.

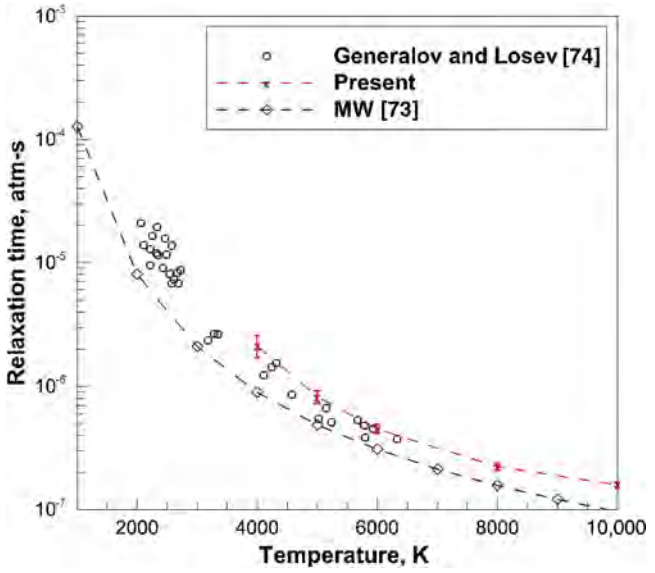

Fig. 14 Vibrational relaxation time of oxygen in collisions with N_2, $T = T_r$.

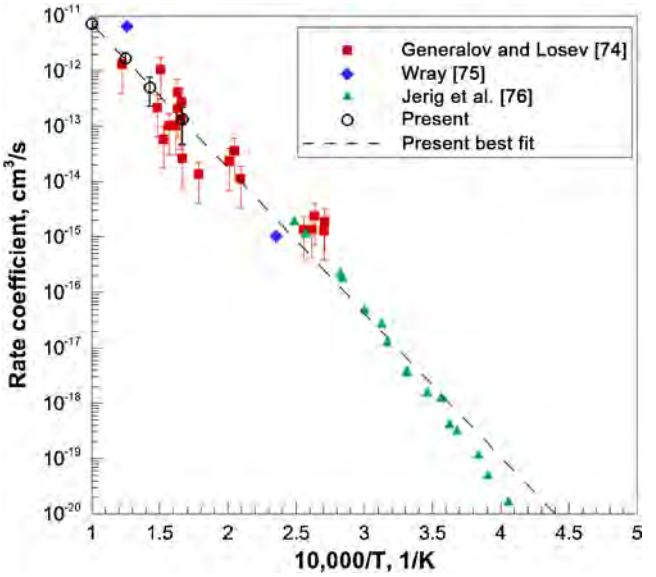

Fig. 15 Thermally equilibrium dissociation RC of oxygen in collisions with N_2.

than to the MW equation. Overall, the present relaxation time is systematically higher than that predicted by the MW correlation. At higher temperatures, namely, at 10,000 K, larger disagreement is seen between the present and MW results. There are several reasons for this. The breakdown of the MW correlation at high temperatures was discussed previously [51]. The uncertainty in relaxation time, derived by means of the QCT method, is related to the accuracy of the PES, implemented in the trajectory simulations, accuracy of the QCT method itself, statistical accuracy, and details of the kinetic model. Although it is extremely difficult to quantify the influence of the first two factors, some things can be said about the influence of the kinetic model. The present relaxation time is derived based on the deactivation RC from the first excited vibrational state. Previous master equation simulations [20,47] for atom–molecule systems indicate that multiquantum processes and kinetics of higher vibrational states tend to decrease the relaxation time at temperatures larger than the characteristic vibrational temperature of the target molecule, which is approximately 2239 K for O_2. The master equation simulation of O_2–N_2 is of great interest and should be conducted in the future.

The dissociation rate of oxygen in collision with a nitrogen molecule was measured previously in shock-tube facilities [74–76]. In the work by Generalov and Losev [74], the rate of dissociation was derived from the initial slope of O_2 concentration after the quasi-stationary distribution was obtained. The rate of oxygen depletion was analyzed by absorption in the SR bands at the wavelength of 224.5 nm. These data are limited to the temperature range between 2700 and 7000 K. In the more recent work by Jerig et al. [76], the rate of dissociation was measured by means of atomic resonance absorption spectroscopy in the range of temperatures between 2400 and 4100 K. This method allows relatively accurate measurements of oxygen atomic concentration in the range of number densities between 10^{12}–10^{14} cm^{-3} at 130.5 nm of wavelength.

The thermal equilibrium dissociation RC of oxygen is shown in Fig. 15. Circular symbols describe the present QCT data, and the dashed line extrapolates the QCT D^{eq} at temperatures below 6000 K. Filled symbols correspond to D^{eq} obtained from the experimental measurements of D^{QSS} [74–76] by means of Eq. (3). As stated in [74], the experimental uncertainty of the dissociation RC, shown by square symbols, can be as high as 70–100%. The lower boundary of this interval is shown in Fig. 15 for the results of Generalov and Losev [74].

The present extrapolated results are in very good agreement with the measurements by Jerig et al. [76]. The shock-tube measurements by Generalov and Losev [74] have much larger scatter, however, the QCT RC is well within the uncertainty range. For extrapolation, the generalized Arrhenius form is used: $D^{eq} = AB^T \exp(-C/T)$. The corresponding coefficients for O_2–N_2 thermal equilibrium dissociation RC are found to be $A = 8.132 \times 10^{-10}$ cm^3/s, $B = -0.131$, $C = 59380$ K. This expression is valid for translational temperatures between 2000 and 10,000 K.

IV. Conclusions

A summary of QCT and master equation studies for O_2–O, O_2–N, and O_2–N_2 molecular systems is given in the present paper. The profiles of vibrational temperature and species number density generated by the conventional MT approach are compared with that of the STS approach. Modification of the governing parameters, namely, dissociation RC and C_{DV}, is proposed to improve the accuracy of the MT method. Specifically, it is recommended to use the QSS dissociation RC rather than the equilibrium RC and the temperature-dependent approximation of C_{DV} to avoid serious discrepancies between MT and STS approaches at high temperatures.

The O_2–N_2 vibrational relaxation time and dissociation RC based on QCT simulations are given for the first time in the literature using a high-fidelity ab-initio six-dimensional PES. The present QCT data are in very good agreement with the experimental measurements by

General and Losev [74]. At the same time, the difficulties and inaccuracies of the QCT approach are recognized when attempting to generate state-specific rates for temperatures below 4000 K. This can be attributed to the failure of the QCT method to describe quantum effects at low temperatures and for low-lying vibrational states. At these temperatures, the QCT method strongly underestimates the true RCs, which can obtained by a more rigorous approach at higher computational cost. Because these temperatures are still of interest for hypersonic simulations, one can recommend the combination of semi- and quasi-classical trajectory approaches to access the wide range of collisional energies.

Acknowledgment

The authors gratefully acknowledge funding for this work through U.S. Air Force Office of Scientific Research Grant FA9550-12-1-0483.

References

[1] Schinke, R., Grebenshchikov, S. Y., Ivanov, M., and Fleurat-Lessard, P., "Dynamical Studies of the Ozone Isotope Effect: A Status Report," *Annual Review of Physical Chemistry*, Vol. 57, No. 1, 2006, pp. 625–661. doi:10.1146/annurev.physchem.57.032905.104542

[2] Aquilanti, V., Bartolomei, M., Carmona-Novillo, E., and Pirani, F., "The Asymmetric Dimer N_2–O_2: Characterization of the Potential Energy Surface and Quantum Mechanical Calculation of Rotovibrational Levels," *Journal of Chemical Physics*, Vol. 118, No. 5, 2003, pp. 2214–2222. doi:10.1063/1.1533015

[3] Varandas, A., and Pais, A., "Double Many-Body Expansion Potential Energy Surface for $O_4(^3A)$, Dynamics of the $O(^3P) + O_3(^1A_1)$ Reaction, and Second Virial Coefficients of Molecular Oxygen," *Theoretical and Computational Models for Organic Chemistry*, Springer–Verlag, New York, 1991, pp. 55–78.

[4] Bender, J. D., Valentini, P., Nompelis, I., Schwartzentruber, T., and Candler, G. V., "Characterization of Vibrational and Rotational Energy Transfer in $N_2 + N_2$ Dissociative Collisions Using the Quasiclassical Trajectory Method," *45th AIAA Thermophysics Conference*, AIAA Paper 2015-3253, June 2015.

[5] Bender, J. D., Valentini, P., Nompelis, I., Paukku, Y., Varga, Z., Truhlar, D. G., Schwartzentruber, T., and Candler, G. V., "An Improved Potential Energy Surface and Multi-Temperature Quasiclassical Trajectory Calculations of $N_2 + N_2$ Dissociation Reactions," *Journal of Chemical Physics*, Vol. 143, No. 5, 2015, Paper 054304. doi:10.1063/1.4927571

[6] Panesi, M., Jaffe, R. L., Schwenke, D. W., and Magin, T. E., "Rovibrational Internal Energy Transfer and Dissociation of $N_2(^1\Sigma_g^+)$–$N(^4S_u)$ System in Hypersonic Flows," *Journal of Chemical Physics*, Vol. 138, No. 4, 2013, Paper 044312. doi:10.1063/1.4774412

[7] Panesi, M., Munafo, A., Magin, T., and Jaffe, R., "Nonequilibrium Shock-Heated Nitrogen Flows Using a Rovibrational State-to-State Method," *Physical Review E: Statistical, Nonlinear, and Soft Matter Physics*, Vol. 90, No. 1, 2014, Paper 013009. doi:10.1103/PhysRevE.90.013009

[8] Bruno, D., Capitelli, M., Esposito, F., Longo, S., and Minelli, P., "Direct Simulation of Non-Equilibrium Kinetics Under Shock Conditions in Nitrogen," *Chemical Physics Letters*, Vol. 360, No. 1, 2002, pp. 31–37. doi:10.1016/S0009-2614(02)00772-8

[9] Esposito, F., Capitelli, M., and Gorse, C., "Quasi-Classical Dynamics and Vibrational Kinetics of $N + N_2(v)$ System," *Chemical Physics*, Vol. 257, Nos. 2–3, 2000, pp. 193–202.

[10] Esposito, F., and Capitelli, M., "QCT Calculations for the Process $N_2(v) + N \rightarrow N_2(v') + N$ in the Whole Vibrational Range," *Chemical Physics Letters*, Vol. 418, No. 4, 2006, pp. 581–585. doi:10.1016/j.cplett.2005.11.036

[11] Kim, J. G., and Boyd, I. D., "State-Resolved Master Equation Analysis of Thermochemical Nonequilibrium of Nitrogen," *Chemical Physics*, Vol. 415, March 2013, pp. 237–246. doi:10.1016/j.chemphys.2013.01.027

[12] Bose, D., and Candler, G. V., "Thermal Rate Constants of the $N_2 + O \rightarrow NO + N$ Reaction Using Abinitio $3A''$ and $3A'$ Potential Energy Surfaces," *Journal of Chemical Physics*, Vol. 104, No. 8, 1996, pp. 2825–2833. doi:10.1063/1.471106

[13] McClinton, C. R., "X-43 Scramjet Power Breaks the Hypersonic Barrier: Dryden Lectureship in Research for 2006," *44th AIAA Aerospace Sciences Meeting and Exhibit*, AIAA Paper 2006-1, Jan. 2006.

[14] Yamashita, K., Morokuma, K., Le Quéré, F., and Leforestier, C., "New Ab Initio Potential Surfaces and Three-Dimensional Quantum Dynamics for Transition State Spectroscopy in Ozone Photodissociation," *Chemical Physics Letters*, Vol. 191, No. 6, 1992, pp. 515–520. doi:10.1016/0009-2614(92)85582-U

[15] Siebert, R., Fleurat-Lessard, P., Schinke, R., Bittererová, M., and Farantos, S., "The Vibrational Energies of Ozone up to the Dissociation Threshold: Dynamics Calculations on an Accurate Potential Energy Surface," *Journal of Chemical Physics*, Vol. 116, No. 22, 2002, p. 9749. doi:10.1063/1.1473664

[16] Tyuterev, V. G., Tashkun, S., Jensen, P., Barbe, A., and Cours, T., "Determination of the Effective Ground State Potential Energy Function of Ozone from High-Resolution Infrared Spectra," *Journal of Molecular Spectroscopy*, Vol. 198, No. 1, 1999, pp. 57–76. doi:10.1006/jmsp.1999.7928

[17] Varandas, A., and Pais, A., "A Realistic Double Many-Body Expansion (DMBE) Potential Energy Surface for Ground-State O_3 from a Multiproperty Fit to Ab Initio Calculations, and to Experimental Spectroscopic, Inelastic Scattering, and Kinetic Isotope Thermal Rate Data," *Molecular Physics*, Vol. 65, No. 4, Nov. 1988, pp. 843–860. doi:10.1080/00268978800101451

[18] Webster, H., III, and Bair, E. J., "Ozone Ultraviolet Photolysis. IV. $O_2 + O(^3P)$ Vibrational Energy Transfer," *Journal of Chemical Physics*, Vol. 56, No. 12, 1972, pp. 6104–6108. doi:10.1063/1.1677161

[19] Andrienko, D., and Boyd, I. D., "Investigation of Oxygen Vibrational Relaxation by Quasi-Classical Trajectory Method," *Chemical Physics*, Vol. 459, Sept. 2015, pp. 1–13. doi:10.1016/j.chemphys.2015.07.023

[20] Andrienko, D. A., and Boyd, I. D., "Rovibrational Energy Transfer and Dissociation in O_2–O Collisions," *Journal of Chemical Physics*, Vol. 144, No. 10, 2016, Paper 104301. doi:10.1063/1.4943114

[21] Esposito, F., and Capitelli, M., "The Relaxation of Vibrationally Excited O_2 Molecules by Atomic Oxygen," *Chemical Physics Letters*, Vol. 443, No. 4, 2007, pp. 222–226. doi:10.1016/j.cplett.2007.06.099

[22] Esposito, F., Armenise, I., Capitta, G., and Capitelli, M., "$O + O_2$ State-to-State Vibrational Relaxation and Dissociation Rates Based on Quasiclassical Calculations," *Chemical Physics*, Vol. 351, Nos. 1–3, 2008, pp. 91–98. doi:10.1016/j.chemphys.2008.04.004

[23] Kulakhmetov, M., Gallis, M., and Alexeenko, A., "Effect of $O_2 + O$ Ab Initio and Morse Additive Pairwise Potentials on Dissociation and Relaxation Rates for Nonequilibrium Flow Calculations," *Physics of Fluids*, Vol. 27, No. 8, 2015, Paper 087104. doi:10.1063/1.4928198

[24] Coletti, C., and Billing, G. D., "Vibrational Energy Transfer in Molecular Oxygen Collisions," *Chemical Physics Letters*, Vol. 356, No. 1, 2002, pp. 14–22. doi:10.1016/S0009-2614(02)00279-8

[25] Billing, G. D., and Kolesnick, R., "Vibrational Relaxation of Oxygen. State to State Rate Constants," *Chemical Physics Letters*, Vol. 200, No. 4, 1992, pp. 382–386. doi:10.1016/0009-2614(92)87008-D

[26] Billing, G. D., "VV and VT Rates in N_2–O_2 Collisions," *Chemical Physics*, Vol. 179, No. 3, 1994, pp. 463–467. doi:10.1016/0301-0104(94)87022-5

[27] Park, H., and Slanger, T., "$O_2(X, v = 8$–$22)$300 K Quenching Rate Coefficients for O_2 and N_2, and $O_2(X)$ Vibrational Distribution from 248 nm O_3 Photodissociation," *Journal of Chemical Physics*, Vol. 100, No. 1, 1994, pp. 287–300. doi:10.1063/1.466997

[28] Price, J., Mack, J., Rogaski, C., and Wodtke, A., "Vibrational-State-Specific Self-Relaxation Rate Constant. Measurements of Highly Vibrationally Excited $O_2(v = 19$–$28)$," *Chemical Physics*, Vol. 175, No. 1, 1993, pp. 83–98. doi:10.1016/0301-0104(93)80230-7

[29] Varandas, A., "Are Vibrationally Excited Molecules a Clue for the O_3 Deficit Problem and HO_x Dilemma in the Middle Atmosphere?" *Journal of Physical Chemistry A*, Vol. 108, No. 5, 2004, pp. 758–769. doi:10.1021/jp036321p

[30] Bender, J., Nompelis, I., Valentini, P., Schwartzentruber, T., Candler, G. V., Doraiswamy, S., Paukku, Y. K., Yang, K. R., Varga, Z., and Truhlar, D. G., "Quasiclassical Trajectory Analysis of the $N_2 + N_2$ Reaction Using a New Ab Initio Potential Energy Surface," *11th AIAA/ASME Joint Thermophysics and Heat Transfer Conference*, AIAA Paper 2014-2964, June 2014.

[31] Varga, Z., Meana-Pañeda, R., Song, G., Paukku, Y., and Truhlar, D. G., "Potential Energy Surface of Triplet N_2O_2," *Journal of Chemical Physics*, Vol. 144, No. 2, 2016, Paper 024310. doi:10.1063/1.4939008

[32] Jaffe, R., Schwenke, D., and Chaban, G., "Vibrational and Rotational Excitation and Dissociation in N_2–N_2 Collisions from Accurate Theoretical Calculations," *10th AIAA/ASME Joint Thermophysics and Heat Transfer Conference*, AIAA Paper 2010-4517, June 2010.

[33] Paukku, Y., Yang, K. R., Varga, Z., and Truhlar, D. G., "Global Ab Initio Ground-State Potential Energy Surface of N_4," *Journal of Chemical Physics*, Vol. 139, No. 4, 2013, Paper 044309. doi:10.1063/1.4811653

[34] Koura, K., "Monte Carlo Direct Simulation of Rotational Relaxation of Diatomic Molecules Using Classical Trajectory Calculations: Nitrogen Shock Wave," *Physics of Fluids*, Vol. 9, No. 11, 1997, pp. 3543–3549. doi:10.1063/1.869462

[35] Secrest, D., and Johnson, B. R., "Exact Quantum-Mechanical Calculation of a Collinear Collision of a Particle with a Harmonic Oscillator," *Journal of Chemical Physics*, Vol. 45, No. 12, 1966, pp. 4556–4570. doi:10.1063/1.1727537

[36] Light, J. C., "Quantum Calculations in Chemically Reactive Systems," *Methods of Computational Physics*, Vol. 10, Academic Press, New York, 2012, pp. 111–142.

[37] Meyer, H.-D., Manthe, U., and Cederbaum, L. S., "The Multi-Configurational Time-Dependent Hartree Approach," *Chemical Physics Letters*, Vol. 165, No. 1, 1990, pp. 73–78. doi:10.1016/0009-2614(90)87014-I

[38] Billing, G. D., "Semiclassical Theory for Diatom-Diatom Collisions," *Chemical Physics Letters*, Vol. 97, No. 2, 1983, pp. 188–192. doi:10.1016/0009-2614(83)85014-3

[39] Cacciatore, M., Kurnosov, A., and Napartovich, A., "Vibrational Energy Transfer in N_2–N_2 Collisions: A New Semiclassical Study," *Journal of Chemical Physics*, Vol. 123, No. 17, 2005, Paper 174315. doi:10.1063/1.2101445

[40] Miller, W. H., "Semiclassical Nature of Atomic and Molecular Collisions," *Accounts of Chemical Research*, Vol. 4, No. 5, 1971, pp. 161–167. doi:10.1021/ar50041a001

[41] Heller, E. J., "Time-Dependent Approach to Semiclassical Dynamics," *Journal of Chemical Physics*, Vol. 62, No. 4, 1975, pp. 1544–1555. doi:10.1063/1.430620

[42] Truhlar, D. G., and Muckerman, J. T., "Reactive Scattering Cross Sections III: Quasiclassical and Semiclassical Methods," *Atom-Molecule Collision Theory*, Springer–Verlag, New York, 1979, pp. 505–566.

[43] Miller, W. H., "Classical-Limit Quantum Mechanics and the Theory of Molecular Collisions," *Advances in Chemical Physics*, Vol. 25, No. 1, 1974, pp. 69–177.

[44] Ulusoy, I., Andrienko, D., Boyd, I., and Hernandez, R., "Quantum and Quasi-Classical Collisional Dynamics of O_2–Ar at High Temperatures," *Journal of Chemical Physics*, Vol. 144, No. 23, 2016, Paper 234311. doi:10.1063/1.4954041

[45] Garcia, E., Kurnosov, A., Lagana, A., Pirani, F., Bartolomei, M., and Cacciatore, M., "Efficiency of Collisional $O_2 + N_2$ Vibrational Energy Exchange," *Journal of Physical Chemistry B*, Vol. 120, No. 8, 2015, pp. 1476–1485.

[46] Kim, J. G., and Boyd, I. D., "Thermochemical Nonequilibrium Modeling of Electronically Excited Molecular Oxygen," *11th AIAA/ASME Joint Thermophysics and Heat Transfer Conference*, AIAA Paper 2014-2963, June 2014.

[47] Andrienko, D., and Boyd, I. D., "Thermal Relaxation of Molecular Oxygen in Collisions with Nitrogen Atoms," *Journal of Chemical Physics*, Vol. 145, No. 1, 2016, Paper 014309. doi:10.1063/1.4955199

[48] Sayós, R., Oliva, C., and Gonzalez, M., "New Analytical (2A′, 4A′) Surfaces and Theoretical Rate Constants for the $N(^4S) + O_2$ Reaction," *Journal of Chemical Physics*, Vol. 117, No. 2, 2002, pp. 670–679. doi:10.1063/1.1483853

[49] Raff, L. M., Thompson, D. L., Sims, L., and Porter, R. N., "Dynamics of the Molecular and Atomic Mechanisms for the Hydrogen-Iodine Exchange Reaction," *Journal of Chemical Physics*, Vol. 56, No. 12, 1972, pp. 5998–6027. doi:10.1063/1.1677149

[50] Panesi, M., and Lani, A., "Collisional Radiative Coarse-Grain Model for Ionization in Air," *Physics of Fluids*, Vol. 25, No. 5, 2013, Paper 057101. doi:10.1063/1.4804388

[51] Park, C., *Nonequilibrium Hypersonic Aerothermodynamics*, Wiley, New York, 1989.

[52] Park, C., "Rotational Relaxation of N_2 Behind a Strong Shock Wave," *Journal of Thermophysics and Heat Transfer*, Vol. 18, No. 4, 2004, pp. 527–533. doi:10.2514/1.11442

[53] Shatalov, O., "Molecular Dissociation of Oxygen in the Absence of Vibrational Equilibrium," *Combustion, Explosion, and Shock Waves*, Vol. 9, No. 5, 1973, pp. 610–613. doi:10.1007/BF00742888

[54] Kalogerakis, K. S., Copeland, R. A., and Slanger, T. G., "Measurement of the Rate Coefficient for Collisional Removal of $O_2(X^3\Sigma_g^-, v = 1)$ by $O(^3P)$," *Journal of Chemical Physics*, Vol. 123, No. 19, 2005, Paper 194303. doi:10.1063/1.2110227

[55] Pejaković, D. A., Campbell, Z., Kalogerakis, K. S., Copeland, R. A., and Slanger, T. G., "Collisional Relaxation of $O_2(X^3\sum_g^-, v = 1)$ and $(a^1\Delta_g, v = 1)$ by Atmospherically Relevant Species," *Journal of Chemical Physics*, Vol. 135, No. 9, 2011, Paper 094309.

[56] Breen, J., Quy, R., and Glass, G., "Vibrational Relaxation of O_2 in the Presence of Atomic Oxygen," *Journal of Chemical Physics*, Vol. 59, No. 1, 1973, pp. 556–557. doi:10.1063/1.1679846

[57] Kiefer, J. H., and Lutz, R. W., "The Effect of Oxygen Atoms on the Vibrational Relaxation of Oxygen," *Symposium (International) on Combustion*, Vol. 11, Elsevier, New York, 1967, pp. 67–76.

[58] Millikan, R. C., and White, D. R., "Systematics of Vibrational Relaxation," *Journal of Chemical Physics*, Vol. 39, No. 12, 1963, pp. 3209–3213. doi:10.1063/1.1734182

[59] Park, C., "Review of Chemical-Kinetic Problems of Future NASA Missions. I—Earth Entries," *Journal of Thermophysics and Heat Transfer*, Vol. 7, No. 3, 1993, pp. 385–398. doi:10.2514/3.431

[60] Capitelli, M., Ferreira, C. M., Osipov, A. I., and Gordiets, B. F., *Plasma Kinetics in Atmospheric Gases*, Springer–Verlag, New York, 2000.

[61] Neitzel, K., Andrienko, D., and Boyd, I. D., "Modeling Fidelity for Oxygen Nonequilibrium Thermochemistry in Reflected Shock Tube Flows," *45th AIAA Thermophysics Conference*, AIAA Paper 2015-2509, June 2015.

[62] Ibraguimova, L., Sergievskaya, A., Levashov, V. Y., Shatalov, O., Tunik, Y. V., and Zabelinskii, I., "Investigation of Oxygen Dissociation and Vibrational Relaxation at Temperatures 4000–10,800 k," *Journal of Chemical Physics*, Vol. 139, No. 3, 2013, Paper 034317. doi:10.1063/1.4813070

[63] Bykova, N., and Kuznetsova, L., "Study of the Absorption Characteristics of Molecular Oxygen in the Schumann-Runge System at High Temperatures: I. Calculations of Absorption Spectra," *Optics and Spectroscopy*, Vol. 105, No. 5, 2008, pp. 668–673. doi:10.1134/S0030400X08110040

[64] Andrienko, D. A., and Boyd, I. D., "High Fidelity Modeling of Thermal Relaxation and Dissociation of Oxygen," *Physics of Fluids*, Vol. 27, No. 11, 2015, Paper 116101. doi:10.1063/1.4935241

[65] Park, C., "Thermochemical Relaxation in Shock Tunnels," *Journal of Thermophysics and Heat Transfer*, Vol. 20, No. 4, 2006, pp. 689–698. doi:10.2514/1.22719

[66] Eckstrom, D., "Vibrational Relaxation of Shock-Heated N_2 by Atomic Oxygen Using the IR Tracer Method," *Journal of Chemical Physics*, Vol. 59, No. 6, 1973, pp. 2787–2795. doi:10.1063/1.1680410

[67] McNeal, R. J., Whitson, M. E., and Cook, G. R., "Temperature Dependence of the Quenching of Vibrationally Excited Nitrogen by Atomic Oxygen," *Journal of Geophysical Research*, Vol. 79, No. 10, 1974, pp. 1527–1531. doi:10.1029/JA079i010p01527

[68] Breshears, W., and Bird, P., "Effect of Oxygen Atoms on the Vibrational Relaxation of Nitrogen," *Journal of Chemical Physics*, Vol. 48, No. 10, 1968, pp. 4768–4773. doi:10.1063/1.1668060

[69] Valentini, P., Schwartzentruber, T. E., Nompelis, I., and Candler, G. V., "Ab Initio Based Model for High Temperature Nitrogen Rovibrational

Excitation and Dissociation," *54th AIAA SCITECH Conference*, AIAA Paper 2016-0500, Jan. 2016.

[70] Bartolomei, M., Carmona-Novillo, E., Hernández, M. I., Campos-Martnez, J., and Moszynski, R., "Global Ab Initio Potential Energy Surface for the $O_2(^3\Sigma_g^-) + N_2(^1\Sigma_g^+)$ Interaction. Applications to the Collisional, Spectroscopic, and Thermodynamic Properties of the Complex," *Journal of Physical Chemistry A*, Vol. 118, No. 33, 2014, pp. 6584–6594. doi:10.1021/jp503182h

[71] Gilmore, F. R., Bauer, E., and McGowan, J. W., "A Review of Atomic and Molecular Excitation Mechanisms in Nonequilibrium Gases up to 20,000°K," *Journal of Quantitative Spectroscopy and Radiative Transfer*, Vol. 9, No. 2, 1969, pp. 157–183. doi:10.1016/0022-4073(69)90084-3

[72] White, D., "Shock-Tube Study of Vibrational Exchange in N_2–O_2 Mixtures," *Journal of Chemical Physics*, Vol. 49, No. 12, 1968, pp. 5472–5476. doi:10.1063/1.1670074

[73] White, D. R., and Millikan, R. C., "Vibrational Relaxation in Air," *AIAA Journal*, Vol. 2, No. 10, 1964, pp. 1844–1846. doi:10.2514/3.2687

[74] Generalov, N., and Losev, S., "Vibrational Excitation and Decomposition of Molecular Oxygen and Carbon Dioxide Behind Shock Waves," *Journal of Quantum Spectroscopy and Radiative Transfer*, Vol. 6, No. 1, 1966, pp. 101–125. doi:10.1016/0022-4073(66)90066-5

[75] Wray, K. L., "Chemical Kinetics of High Temperature Air," Avco-Everett Research Lab., Avco Corp., Everett, MA, 1961.

[76] Jerig, L., Thielen, K., and Roth, P., "High-Temperature Dissociation of Oxygen Diluted in Argon or Nitrogen," *AIAA Journal*, Vol. 29, No. 7, 1991, pp. 1136–1139. doi:10.2514/3.10714

AIAA SciTech Forum
7-11 January 2019, San Diego, California
AIAA Scitech 2019 Forum

10.2514/6.2019-2281

Effect of Thermochemistry Modeling on Hypersonic Flow Over a Double Cone

Michael E. Holloway*, Kyle M. Hanquist†, and Iain D. Boyd‡
Department of Aerospace Engineering, University of Michigan, Ann Arbor, MI 48109

The influence of different assumptions for thermochemistry modeling in hypersonic flow over a double-cone geometry is investigated. The double-cone geometry is simple but produces a complex shock wave/boundary layer interaction and nonequilibrium flow physics. This interaction significantly impacts the aerothermodynamic loading, in terms of surface pressure and heat transfer. Therefore, it is important that these interactions can be predicted with physical accuracy and numerical efficiency. A CFD analysis is used to study the double-cone in three different thermochemical cases: nonequilibrium flow, equilibrium flow, and frozen flow for five different mixtures of nitrogen and oxygen. Specific areas of interest include the thermochemistry model effects on the flow field and surface properties. The resulting aerodynamic loads are compared to experiments and indicate that thermochemistry modeling assumptions play a significant role in determining surface properties. It is also shown that heat loading is more sensitive to thermochemical modeling than drag and suggests that an accurate measurement of surface heat transfer is of particular interest. Careful analysis also reveals that high enthalpy and pure oxygen flows are particularly sensitive to the thermochemistry model assumed.

Nomenclature

Symbols

C	=	Forward rate
e	=	Specific energy, J/kg
h	=	Planck's constant, m^{2}kg/s
h_o	=	Total specific enthalpy, J/kg
k	=	Boltzmann constant, m^{2}kg/s^2-K
K	=	Reaction rate, s^{-1}
m	=	Mass, kg
P	=	Pressure, Pa
Q_{el}	=	Electronic partition function
t	=	Time, s
T	=	Temperature, K
v	=	Velocity, m/s
X	=	Equilibrium molecular density (kg/m^3)
X_i	=	CFD molecular density (kg/m^3)
α	=	Degree of dissociation
θ	=	Characteristic temperature, K
ζ	=	Degrees of freedom
λ	=	Mean free path, m
ρ	=	Density, kg/m^3
τ	=	Relaxation time, s

Subscripts

d	Dissociation
el	Electron/electronic energy mode
r	Rotational energy mode
tr	Translational-rotational energy mode
vib	Vibrational energy mode
∞	Freestream

Superscripts

a	Atom
aa	Molecule
$*$	Equilibrium

Abbreviations

2T	Two temperature
CFD	Computational fluid dynamics
RE	Radiative Equilibrium

I. Introduction

For the past several decades there has been an interest in sustained hypersonic flight for commercial and military use. This interest is not only in the United States, but around the world. NASA, the European Space Agency, Russia, China, and JAXA have all funded civilian and military programs involving hypersonic flight. A couple of examples

*PhD Candidate, Department of Aerospace Engineering, AIAA Student Member, mhollo@umich.edu
†Postdoctoral Research Fellow, Department of Aerospace Engineering, AIAA Member, hanquist@umich.edu
‡James E. Knott Professor of Engineering, Department of Aerospace Engineering, Fellow AIAA, iainboyd@umich.edu

include NASA's X-43A [1], which flew at Mach 9.68 for 10.5 seconds of powered flight and AFRL's X-51A, which flew near Mach 5 for over 200 seconds [2].

The development of hypersonic vehicles relies heavily on computational simulations due to the extreme challenge of replicating the high enthalpy flows experimentally. It has become apparent that the combination of experimental and theoretical data is key in improving computational models of nonequilibrium flow. The accuracy of these models becomes very important when they are used in conditions where oxygen molecules do not dissociate completely, such as sustained hypersonic flight that operates between Mach 5 to Mach 10 [3].

One of the most important aspects of hypersonic aerothermodynamics is how the thermochemistry affects the surface properties, which produces significant changes in the shock wave interaction with the boundary-layer. This interaction significantly affects aerothermodynamic loading, in terms of surface pressure and surface heat transfer. Therefore, it is important that these interactions can be predicted with physical accuracy and numerical efficiency.

A simple geometry that creates shock wave boundary layer interaction and nonequilibrium effects is the double-cone, shown in Fig. 1. The double-cone has been studied extensively throughout the past two decades [5–9]. In order to assess the accuracy of nonequilibrium models in predicting aerothermodynamic loads in hypersonic flight, this study specifically focuses on hypersonic shock wave laminar boundary layer interactions. Though the hypersonic shock wave boundary layer interactions in transitional and turbulent flows are important, the laminar boundary layer restriction allows for a straightforward assessment of the nonequilibrium thermochemistry models without the added complexity and cost of modeling the transitional and turbulent boundary layers [5].

Figure 1. Double cone geometry [4]

A set of widely used double-cone experiments for code validation was conducted at the Calspan-University of Buffalo Research Center (CUBRC) [10, 11]. The double-cone experimental flow field consists of an attached shock at the leading edge of the first cone and a detached shock generated downstream by the second cone. This shock-shock interaction causes a separation in the boundary layer. The separated shock then interacts with the rear shock to form a triple point. The flow field structure is shown in Fig. 2.

In order to determine the sensitivity of the flow and surface properties to thermochemistry modeling, several different double-cone cases are studied. Each case consists of different mixtures of nitrogen and oxygen with different freestream properties.

The following manuscript will describe the numerical approach used in this study, describe each test case condition, examine the resulting flow properties for each thermochemistry model, discuss any differences in surface properties, and study the extent of nonequilibrium in each case. The article ends with some conclusions and options for future work.

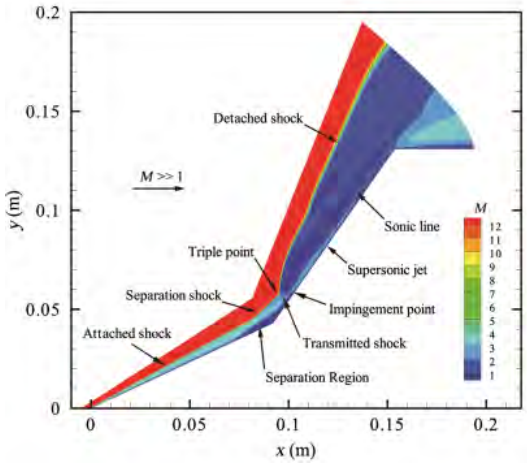

Figure 2. Flow field structure [9]

II. Numerical Approach

The numerical simulations presented in this study are performed using the CFD code LeMANS, which was developed at the University of Michigan to simulate hypersonic reacting flows [12]. A complete overview of LeMANS can be found in [13].

LeMANS is a multi-dimensional, parallel code that solves the Navier-Stokes equation with second-order spatial accuracy on structured and unstructured computational grids. LeMANS includes thermochemical nonequilibrium effects and the flow is modeled assuming that the continuum approximation is valid. LeMANS couples the Navier-Stokes equations with thermodynamic and transport property models [12]. Also included in the code are models for finite rate chemistry and energy relaxation models [12]. LeMANS solves the flow field by integrating differential equations spatially and temporally. The finite volume method is implemented to integrate spatially. A flux vector splitting scheme is

implemented to calculate the flux of inviscid components across cell faces and a central scheme is used for the viscous fluxes [12]. The viscous stresses are modeled by assuming the flow is Newtonian and applying Stokes' hypothesis. LeMANS also has multi-temperature modeling capability for thermochemical nonequilibrium. LeMANS has been verified and validated using a wide range of hypersonic conditions.

This study investigates three different thermochemical regimes: nonequilibrium, equilibrium, and frozen. Thermochemistry involves both chemical reactions, such as dissociation and recombination, and energy transfer between different energy modes, and for the purpose of this study, between the translational and vibrational modes.

LeMANS uses the standard Millikan-White expression to model the vibrational relaxation time along with the high-temperature correction of Park [14,15]. The vibrational relaxation time is then used in the Landau-Teller equation, Eq. 1.

$$\frac{de_v(t)}{dt} = \frac{e_{vib}(t,T) - e_{vib}(t,T_{vib})}{\tau_{vib}} \tag{1}$$

Chemistry is modeled using rate coefficients expressed in modified Arrhenius form, as shown in Eq. 2, where C and η are usually defined from experimental measurements. Increasing C increases the rate of the particular reaction pushing it closer to equilibrium. Decreasing C will slow the reaction pushing it towards a frozen state.

$$K = CT^{\eta} exp\left(-\frac{\theta_d}{T}\right) \tag{2}$$

The *nonequilibrium* case uses standard rates in the chemistry and the vibrational-translational energy transfer equations. The *equilibrium* case increases the leading coefficient C in Eq. 2 by six orders of magnitude and assumes vibrational equilibrium, $T_{vib} = T_{tr}$. The *frozen* flow case decreases the leading coefficient by six orders of magnitude and the vibrational relaxation time is increased by six orders of magnitude. The thermochemical nonequilibrium effects are modeled using the two temperature (2T) model for thermal nonequilibrium and the chemical reactions are accounted for in the source terms of the species continuity equations. In this case there are two temperatures: translational, T_{tr}, and vibrational, T_{vib}. LeMANS assumes that the rotational temperature, T_r, can be represented by T_{tr} and that the vibrational, electronic, and electron translational energy modes can be represented by T_{vib}.

In the current study, either an isothermal or radiative equilibrium wall condition is employed. The radiative wall condition is accomplished by setting the radiative flux equal to the convective heating crossing the wall to solve for surface temperatures. An in depth description of the wall conditions can be found in [13].

III. Results

A. Test Case Descriptions

Each double-cone case and the freestream conditions considered in this study are shown in Table 1 [11, 16, 17]. Run 90 is studied to determine if thermochemistry modeling is significant for oxygen at low enthalpy. Run 86 is chosen to study the significance of modeling thermochemistry in a high enthalpy oxygen case. Run 46 is studied to determine if nitrogen is sensitive to thermochemistry models at high enthalpy. Runs 1 and 43 are air cases at low and high enthalpy, respectively. Each case is also chosen for their good agreement between experimental results and past nonequilibrium models; reasonable agreement on the front cone indicates that the data is valid. The geometry specifications of the double-cone are shown in Fig. 3 and consists of a 25°first cone and a 55°second cone. The computational grid consists of approximately 300,000 cells with 636 cells along the wall for which the solutions have been demonstrated to be independent. Due to the short run time of the experiments, each case is modeled as an isothermal wall to better match the CUBRC results. However, such conditions are not representative of actual flight, so Run 90 is also modeled using the radiative equilibrium wall boundary condition to assess any sensitivity on the surface properties and sensitivity to thermochemistry modeling.

B. Flowfield Results

Contours of translational temperature from the nonequilibrium and equilibrium solutions for the isothermal wall Run 90 case are shown in Fig. 4. Each case demonstrates steady flow results. These temperature contours are representative of the other nonequilibrium and equilibrium Runs. For each Run, as illustrated in Fig. 4, higher flow temperatures occur for the nonequilibrium case.

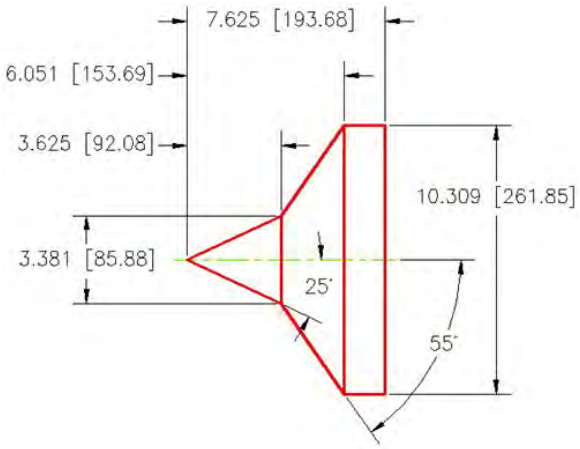

Figure 3. Double-cone model (dimensions in inches [mm]) [4]

Table 1. Freestream properties and composition given in terms of species mass-fractions [11, 16, 17]

Run:	Mach	h_0 (MJ/kg)	ρ_∞ (g/m^3)	T_∞ (K)	$T_{v\infty}$ (K)	T_{wall} (K)	v_∞ (m/s)	N_2	N	O_2	O	NO
90*	10.37	3.99	1.8342	190.1	1001	300	2731	0.00	0.00	0.9986	0.0016	0.00
88	8.2	8.78	1.0613	569.8	697.6	300	3853	0.00	0.00	0.9482	0.0518	0.00
46	11.54	8.4	1.958	281.7	3072	296.3	3946.9	0.99842	0.00158	0.00	0.00	0.00
1	12.2	5.44	0.499	175	175	300	3246	0.765	0.00	0.235	0.00	0.00
43	8.87	10.2	2.134	576	576	296.2	4218.1	0.73704	0.00	0.17160	0.02659	0.06477

*Run 90 is also simulated with the RE wall condition

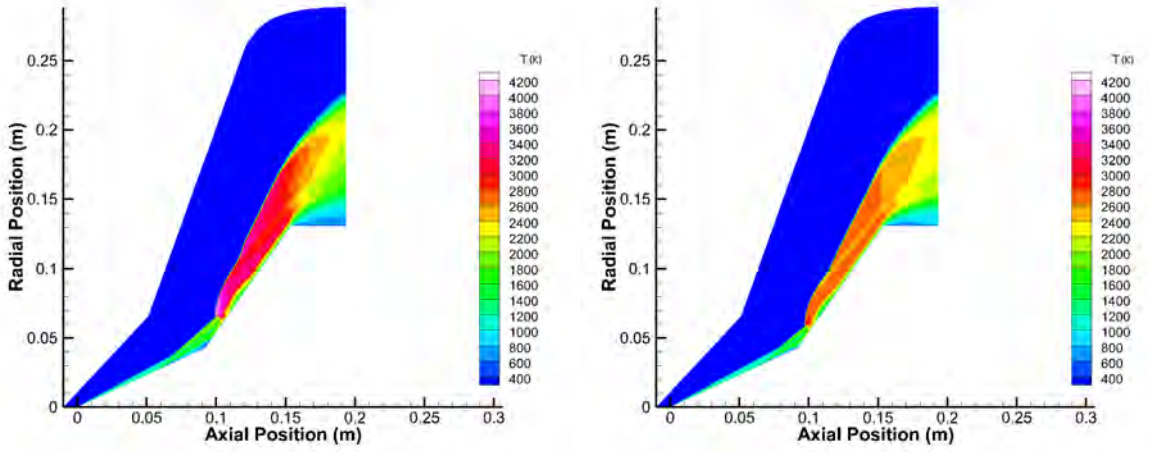

a) Temperature contours (Run 90 nonequilibrium) **b) Temperature contours (Run 90 equilibrium)**

Figure 4. Results for the Nonequilibrium and Equilibrium cases

The translational temperature contours for the frozen flow Run 90 isothermal wall case are shown in Fig. 5a at 100,000 iterations. This case produces unsteady flow, as shown by the time variation in surface pressure, illustrated in Fig. 5b. When compared to the nonequilibrium solution in Fig. 4, the frozen case shows higher flow temperatures and earlier points of flow separation.

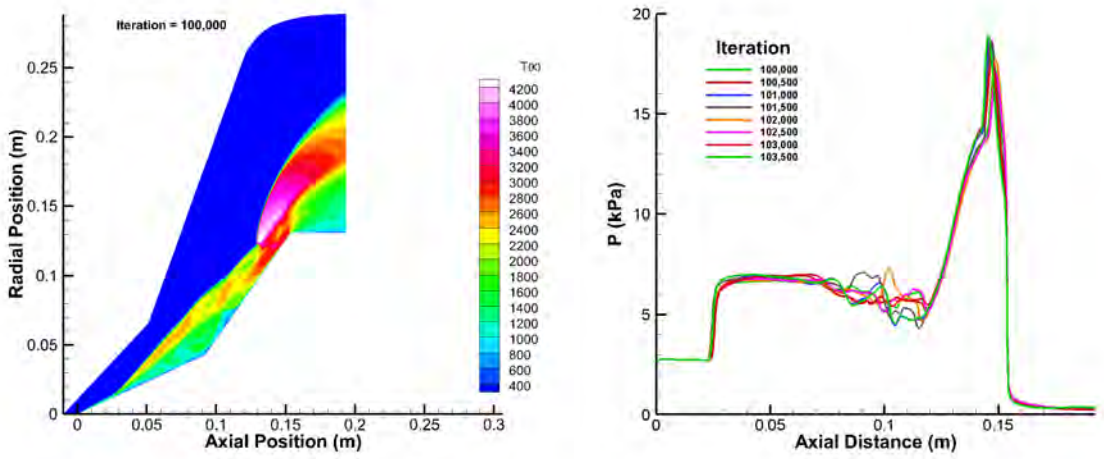

a) Temperature contours at 100,000 iterations **b) Surface pressure at different time steps**

Figure 5. Results for the Frozen flow case (Run 90)

C. Surface Properties

The effects that each thermochemistry modeling approach has on the surface of the double-cone, in terms of pressure and heat transfer, are discussed below. The unsteady flow cases use time-averaged results. The experimental results were produced at CUBRC [11, 16, 17]. An in-depth evaluation of the resulting drag and heat load is also discussed.

Run 90 is a low enthalpy oxygen case. The surface properties are shown in Fig. 6. The frozen solution is unsteady for the isothermal wall conditions and steady for the RE wall condition. The nonequilibrium, isothermal wall surface properties produced by LeMANS are consistent with Nompelis et al. [17], however, the LeMANS simulation better captures the experimental data in the separated flow region. The results show that there are clear differences between the three thermochemistry approaches. The radiative wall condition also produces differences when thermochemistry modeling is varied. While the radiative wall condition slightly affects surface pressure, it significantly reduced surface heat transfer by as much as 55%. The separation location is also affected. These differences suggest that the specific approach taken to modeling thermochemistry is important for low enthalpy oxygen flows. Further, the use of a cold wall in the experiments has a significant effect on heat transfer in comparison to a more realistic heated wall condition.

Run 88 is a high enthalpy oxygen case. The surface properties are shown in Fig. 7. The frozen solution is steady. The nonequilibrium surface properties produced by LeMANS are again consistent with Nompelis et al. [17]. The nonequilibrium results match the measurements well on the front cone. The results show that the nonequilibrium and equilibrium solutions are similar, however, these two cases are much different than the frozen case simulation. These results suggest that thermochemistry modeling is necessary in a high enthalpy, frozen oxygen flow situation.

Run 46 is a high enthalpy nitrogen case. The surface properties are shown in Fig. 8. The nonequilibrium surface properties produced by LeMANS are again consistent with prior CFD analysis of Nompelis et al. [16]. The nonequilibrium results also show some agreement with the experimental data on the front cone. The thermochemistry models show poor agreement with the experimental results. The frozen case is again unsteady and the results are time-averaged. The results produced by LeMANS show clear differences between the equilibrium, nonequilibrium and frozen cases, and the nonequilibrium case does not agree with the measurements. These results indicate that this high enthalpy nitrogen flow is a particularly good test case for assessment of detailed thermochemistry models.

Run 1 is a low enthalpy air case. The surface properties are shown in Fig. 9. The frozen solution is steady. The nonequilibrium surface properties produced by LeMANS are consistent with the CFD simulation presented by CUBRC in [11]. The nonequilibrium pressure calculated by LeMANS shows little agreement with the experimental values in the separated region. The computational heat transfer slightly under predicts the experimental heat transfer values on the forward cone, but shows good agreement with experimental values in the separated flow region. The surface properties produced by LeMANS shows clear, though small, differences in each thermochemistry model. The results indicate that separation occurs earliest in the frozen case and latest for the equilibrium case. These solution also show lower spikes in pressure and heat load for the equilibrium case and larger spikes for the frozen case. The simulations for Run 1 show mixed agreement with the experimental values and relatively small differences in ther-

mochemistry models. While this case may not show the most dramatic differences, it is interesting in that the frozen and nonequilibrium cases are more similar to one another, with the equilibrium solution showing more significant differences.

Run 43 is a high enthalpy air case. The surface properties are shown in Fig. 10. The frozen solution is again unsteady and the results are time-averaged. The surface properties produced by LeMANS are again consistent with prior CFD analysis of Nompelis et al. [16]. While the equilibrium and nonequilibrium results appear similar, the equilibrium solution shows a higher spike in pressure and heat transfer in the separated flow region. However, these two solutions differ greatly from the frozen case indicating that this high enthalpy air flow is a particularly interesting case for showcasing the assessment of detailed thermochemistry models.

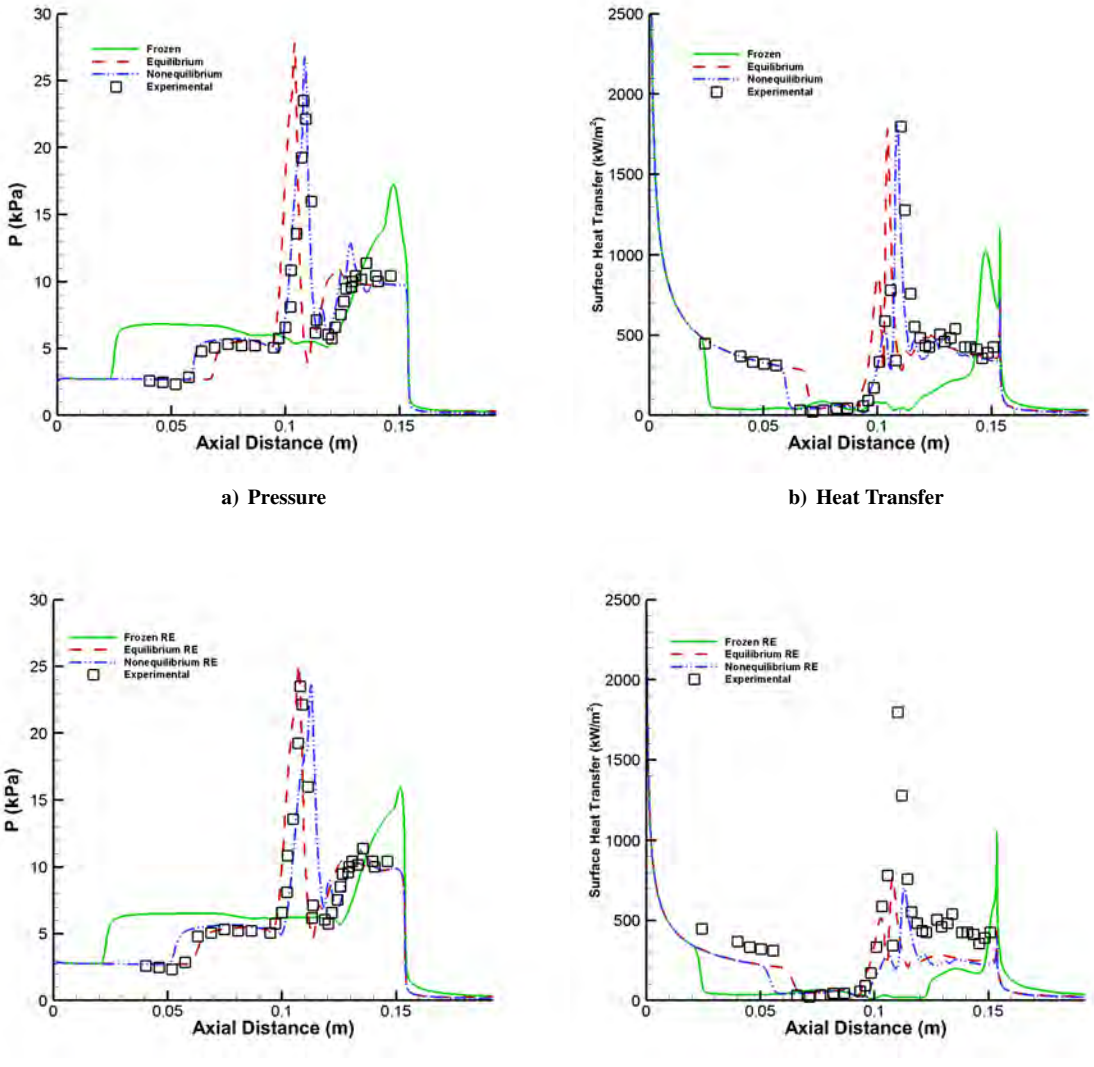

a) Pressure

b) Heat Transfer

c) Pressure RE

d) Heat Transfer RE

Figure 6. Run 90 surface properties. Including the RE wall condition.

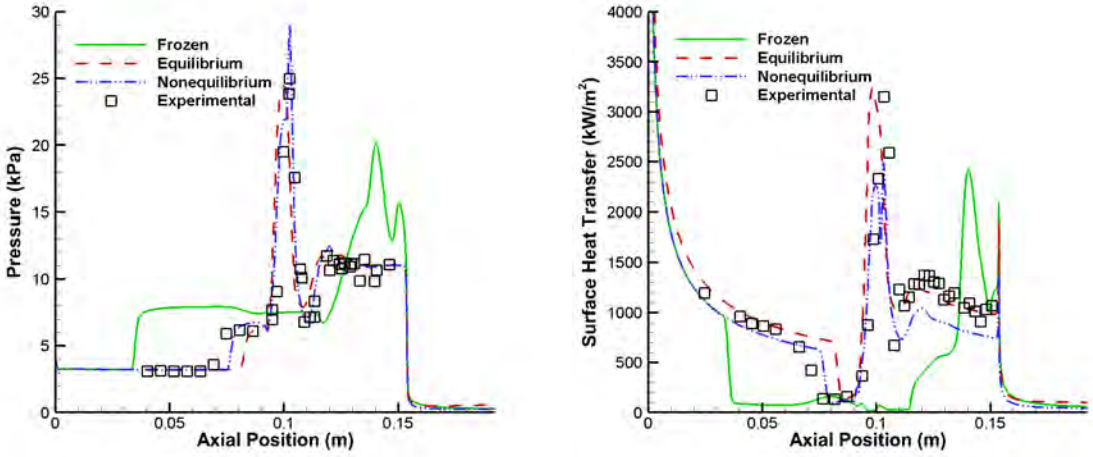

a) Surface pressure b) Surface heat transfer

Figure 7. Run 88 surface properties

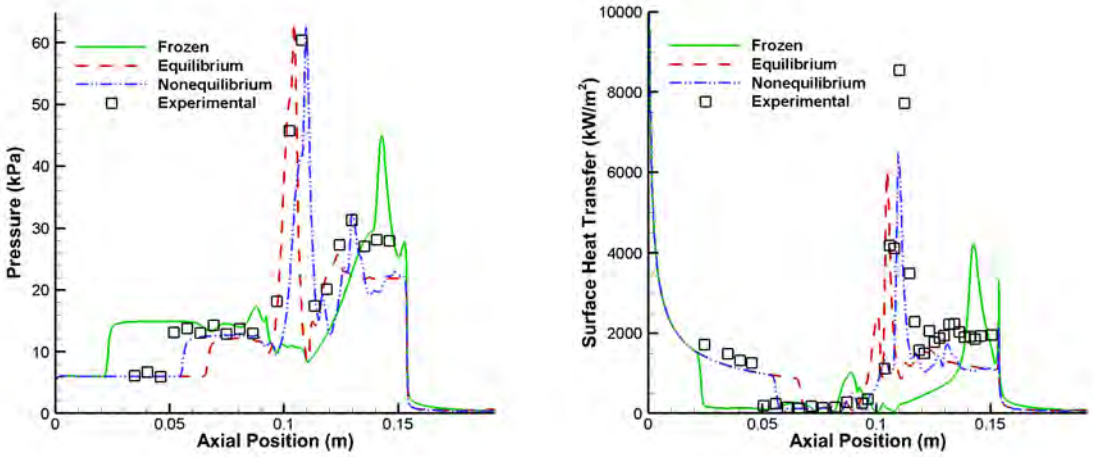

a) Surface pressure b) Surface heat transfer

Figure 8. Run 46 surface properties

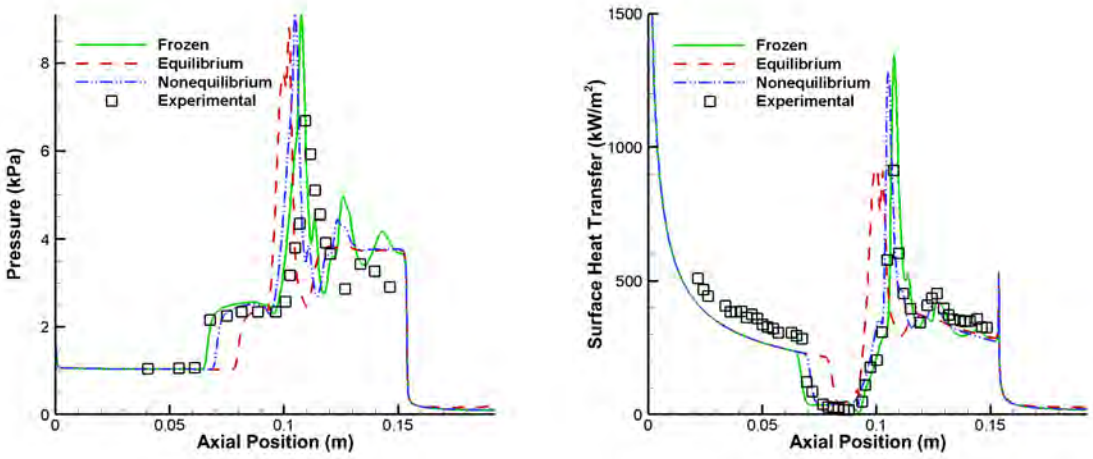

a) Surface pressure b) Surface heat transfer

Figure 9. Run 1 surface properties

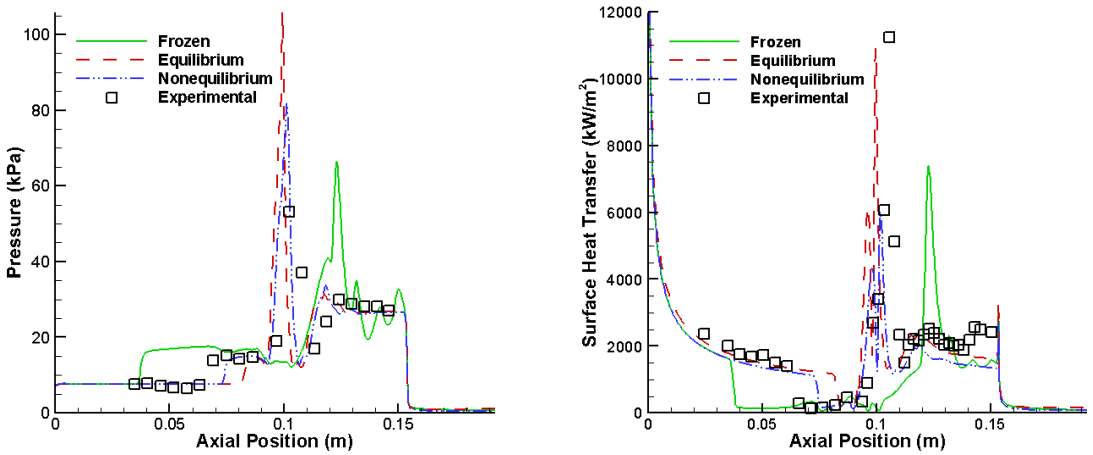

a) Surface pressure b) Surface heat transfer

Figure 10. Run 43 surface properties

The location of the onset of separation for each case is shown in Table 2. The table shows that the separation point occurs earliest for the frozen solutions and latest for the equilibrium solutions. The difference in separation point location is a few centimeters. The validation in the location of separation points shows sensitivity to the thermochemistry modeling.

The CUBRC separation points were determined by averaging the data point before the pressure rise and the data point where a pressure rise is first seen. There are significant differences in the separation points computed with the nonequilibrium approach and the CUBRC experiments, except for Run 90.

D. Aerothermodynamic Loading

The resulting pressure and shear stress values along the double-cone surface are integrated over the surface area to calculate the total drag, shown in Table 3. For all six cases, the percentage difference in drag between the equilibrium and nonequilibrium solutions is less than 2% suggesting that the details of thermochemistry modeling are relatively unimportant for this parameter. With the exception of Run 1, frozen thermochemistry significantly over predicts drag

Table 2. Axial Location of Separation (m)

Run:	Nonequilibrium	Equilibrium	Frozen	CUBRC
90	0.058	0.067	0.023	0.058
90 (RE Wall)	0.050	0.060	0.021	
88	0.075	0.080	0.033	0.066
46	0.054	0.064	0.021	0.048
1	0.069	0.078	0.065	0.064
43	0.073	0.080	0.036	0.066

in comparison to the nonequilibrium thermochemistry approach. For the Run 90 case, use of the radiative equilibrium wall has no effect on drag with equilibrium thermochemistry, but leads to a significant increase in drag difference with the frozen flow approach.

Table 3. Total Drag (N)

Run:	Nonequilibrium	Equilibrium	Frozen	% Difference Noneq./Eq.	% Difference Noneq./Frozen
90	526	524	508	0.48	3.52
90 (RE Wall)	525	522	489	0.48	7.09
88	597	597	623	0.10	4.26
46	1170	1160	1154	1.15	1.68
1	206	203	210	1.81	1.59
43	1430	1430	1451	0.43	1.37

The resulting surface heat transfer values are integrated over the surface area to calculate the total heat load for each case, shown in Table 4. Run 90 shows large percent differences in the heat loading, especially between the nonequilibrium and frozen cases. The percent difference between the nonequilibrium and equilibrium case almost doubles when the RE wall condition is applied while the frozen case remains relatively unchanged. Run 88 shows the most extreme changes in heat load when the thermochemistry models are altered. Run 46 also shows significant differences in heat load when the thermochemistry models are altered. Run 1 shows that the difference in heat load between nonequilibrium and equilibrium flow is much greater than the difference between nonequilibrium and frozen flow. However, these percent differences are minimal when compared to the previous five cases, indicating that this parameter is less sensitive for a low enthalpy air case. Run 43 shows large differences between nonequilibrium and equilibrium flow when compared to the frozen solution. However, unlike Run 1, Run 43 shows a significant increase between the nonequilibrium and equilibrium solution. Run 43 is especially interesting when Table 4 is compared to Fig. 10b. Though the nonequilibrium and frozen surface properties look dramatically different, when integrated the total heat load is only slightly altered. These results show that thermochemistry models have a very significant effect on heat load for high and low enthalpy oxygen flows, high enthalpy nitrogen flows, and high enthalpy air flows. Most importantly, these results stress the importance of carefully considering thermochemistry models when dealing with all high enthalpy freestream properties. Tables 3 - 4 also indicates that heat loading is much more sensitive to thermochemical modeling than drag.

Table 4. Heat Load (kW)

Run:	Nonequilibrium	Equilibrium	Frozen	% Diff Noneq./Eq.	% Diff Noneq./Frozen
90	29.2	31.2	21.6	6.62	29.9
90 (RE Wall)	18.0	20.3	13.3	12.0	30.0
88	67.2	88.1	55.7	27.0	18.7
46	91.4	95.2	82.6	4.07	10.1
1	25.0	26.0	25.1	3.92	0.399
43	118	147	116	21.5	2.31

E. Extent of Nonequilibrium

To characterize the extent of nonequilibrium, a study of the thermal and chemical properties for Runs 46, 88, 90, and 90 RE wall are performed. The extent of thermal nonequilibrium is characterized by the temperature ratio T_{tr}/T_v. The extent of chemical nonequilibrium is characterized by the density ratio between equilibrium chemistry and that calculated by LeMANS under the nonequilibrium thermochemistry approach. The equilibrium chemistry value is calculated using the Law of Mass Action, Eq. 3, in which α^* is the degree of dissociation which is equal to the atomic mass fraction. The constants used in Eq. 3 are shown in Table 5.

$$\frac{(\alpha^*)^2}{1-\alpha^*} = \frac{exp\left(-\frac{\theta_d}{T}\right)}{\rho}\left\{m_a\left(\frac{\pi m_a k}{h^2}\right)^{\frac{3}{2}}\theta_r\sqrt{T}\left[1-exp\left(-\frac{\theta_v}{T}\right)\right]\frac{(Q_{el}^a)^2}{Q_{el}^{aa}}\right\} \tag{3}$$

Table 5. Values for Eq. 3

Species	θ_d (K)	θ_r (K)	θ_v (K)	Q_{el}^a	Q_{el}^{aa}
O_2	59500	2.08	2280	9	3
N_2	113000	2.9	3390	4	1

For simplicity, the extent of nonequilibrium is evaluated only for the pure oxygen and pure nitrogen cases. The extent of thermal nonequilibrium is shown in Fig. 11. Each Run shows significant amounts of thermal nonequilibrium even in the freestream. In Run 90, Figs. 11a-11b, the two sets of contours are similar indicating weak dependence on the specific wall surface model. Here, the total region of thermal nonequilibrium is the largest and this correlates with the largest differences in heat loads predicted by the frozen and nonequilibrium flow models. The contours for Run 88, Fig. 11c, show the highest levels of nonequilibrium temperature ratio and this is the condition with the widest range of heat load values. In Run 46, Fig. 11d, the temperature ratio remains less than one on the first cone but then displays similar trends to Run 90 on the second cone. There is no obvious correlation with the fact that Run 46 has relatively low variation in heat load between the three thermochemistry approaches.

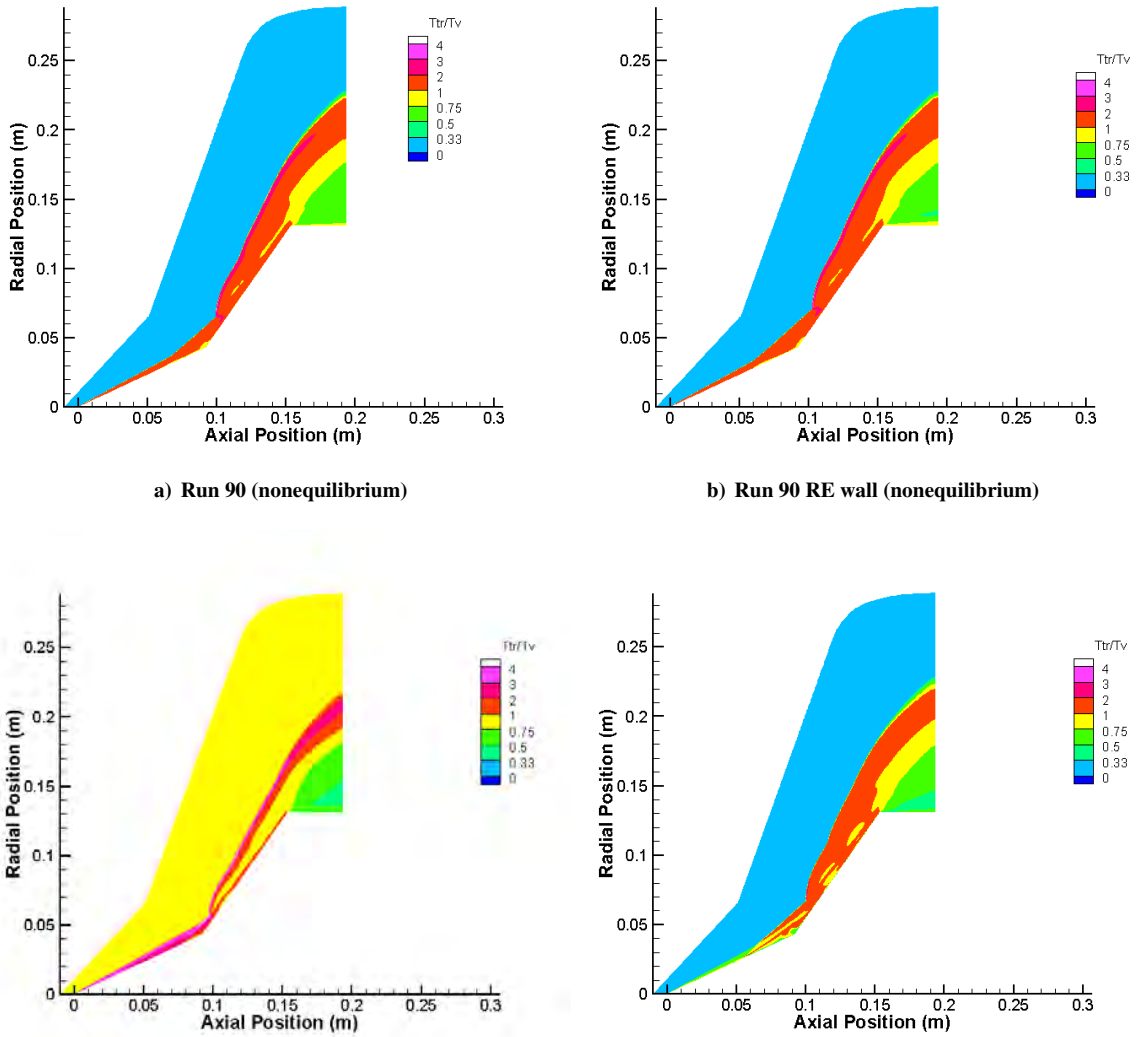

a) Run 90 (nonequilibrium)

b) Run 90 RE wall (nonequilibrium)

c) Run 88 (nonequilibrium)

d) Run 46 (nonequilibrium)

Figure 11. Extent of thermal nonequilibrium

The extent of chemical nonequilibrium is shown in Fig. 12. Runs 90 and 46, Figs. 12a, 12b, and 12d, display significant regions of chemical nonequilibrium behind the second detached shock, but in each case equilibrium is recovered at the cone surfaces. This suggests that chemical nonequilibrium plays a minor role in the surface properties for these cases. Run 88, Fig. 12c, has the strongest degree of chemical nonequilibrium and it is maintained all the way to the surface. This is the case that also has the widest spread in integrated heat load between the different thermochemistry models.

Overall, the analysis of thermal and chemical nonequilibrium provides a conclusion that is not unexpected: the conditions of Run 88, for which there is the greatest variation in surface properties for the three different modeling approaches, is the one with the highest enthalpy and, because it is also a pure oxygen flow, the highest level of thermochemical activity. However, it is worth noting that Run 46 in nitrogen has a similar enthalpy to Run 88, but significantly less thermochemical activity and clearly reduced variation in heat load with thermochemical model. With a 50% difference in vibrational energy spacing between nitrogen and oxygen, and an almost 100% difference in chemical bond strength, it is clear that any general evaluation of the role of the importance of thermochemistry modeling must account for the specific thermochemical properties of the gas involved.

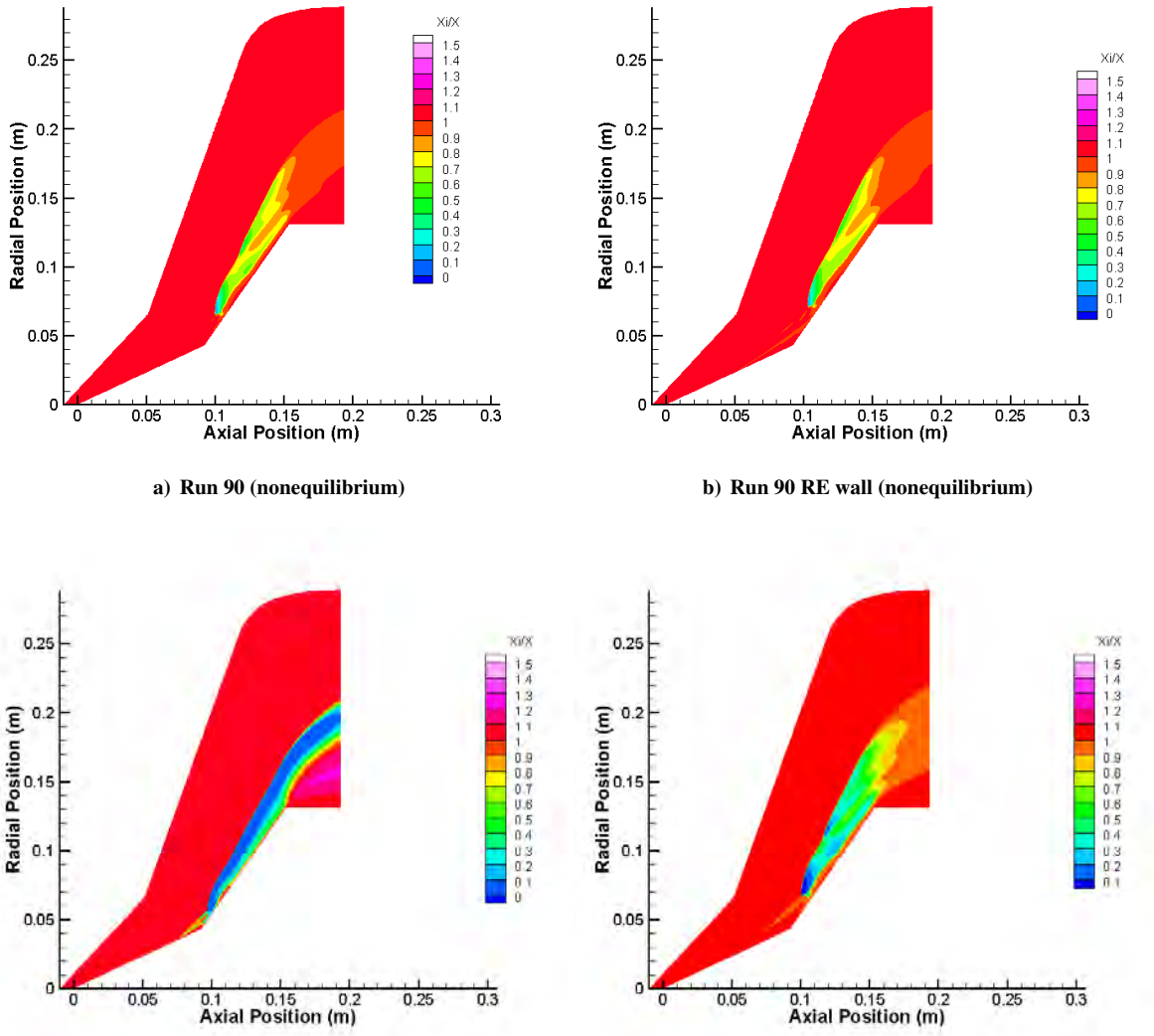

a) Run 90 (nonequilibrium)

b) Run 90 RE wall (nonequilibrium)

c) Run 88 (nonequilibrium)

d) Run 46 (nonequilibrium)

Figure 12. Extent of chemical nonequilibrium

IV. Conclusion

The influence of different assumptions for thermochemistry modeling in hypersonic flow over a double-cone was studied. These results showed that the flow properties of frozen thermochemistry models have greater translational temperatures while equilibrium models have the lowest. The possibility of unsteady flow is also observed in some frozen cases. The surface property analysis demonstrated a delay in flow separation when the thermochemistry model moved closer to equilibrium. It also showed the significant sensitivity to thermochemistry modeling for all high enthalpy cases and low enthalpy oxygen cases. In general, the drag analysis showed that similar results were obtained with the nonequilibrium and equilibrium approaches while frozen thermochemistry produced larger differences. The heat load analysis demonstrated significant differences between the equilibrium, nonequilibrium, and frozen thermochemistry models and that high enthalpy oxygen cases are especially sensitive. Lastly, the extent of nonequilibrium study gives the impression that thermal nonequilibrium is more sensitive than chemical nonequilibrium. It also suggests that the extent of nonequilibrium is proportional to the freestream enthalpy and that the wall model has no effect on the amount of nonequilibrium in the flow field.

These results indicate that some of the double-cone cases investigated at CUBRC are much more sensitive to the details of thermochemistry than others. For example, high enthalpy oxygen flow appears to be the most sensitive of

the cases considered. In addition, sensitivity to thermochemistry varies across different aspects of the flows. While the total drag is relatively insensitive to thermochemistry, the separation point is more sensitive, and the total heat load showed variations of up to $\pm$ 30% between the different thermochemistry models.

Future work will continue to try and identify flow conditions under which high-fidelity thermochemistry modeling is needed. Studies will expand the investigation to consider other types of flow configurations. In addition, detailed comparisons will be made between the standard nonequilibrium model employed here, and quantum-state resolved thermochemistry models. Effects of turbulence will also be considered.

Acknowledgements

The authors acknowledge funding through the U.S. Air Force Office of Scientific Research Grant FA9550-16-1-0291.

References

[1] Voland, R. T., Huebner, L. D., and McClinton, C. R., "X-43A hypersonic vehicle technology development," *Acta Astronautica*, Vol. 59, No. 1-5, 2006, pp. 181–191.

[2] Rondeau, C. M. and Jorris, T. R., "X-51A Scramjet demonstrator program: waverider ground and flight test," Tech. rep., Air Force Flight Test Center Edwards AFB CA Test Wing (412th) Operations Group (412th)/Flight Test Squadron (413th), 2013.

[3] Neitzel, K., Andrienko, D., and Boyd, I. D., "Aerothermochemical nonequilibrium modeling for oxygen flows," *Journal of Thermophysics and Heat Transfer*, Vol. 31, No. 3, 2017, pp. 634–645.

[4] Holden, M. S., Wadhams, T. P., MacLean, M. G., and Dufrene, A. T., "Measurements of Real Gas Effects on Regions of Laminar Shock Wave/Boundary Layer Interaction in Hypervelocity Flows for "Blind'Code Validation Studies," *21st AIAA Computational Fluid Dynamics Conference*, 2013, p. 2837.

[5] Gaitonde, D. V., Canupp, P. W., and Holden, M. S., "Heat transfer predictions in a laminar hypersonic viscous/inviscid interaction," *Journal of Thermophysics and Heat Transfer*, Vol. 16, No. 4, 2002, pp. 481–489.

[6] Roy, C. J., Gallis, M. A., Bartel, T. J., and Payne, J. L., "Navier-Stokes and direct simulation Monte Carlo predictions for laminar hypersonic separation," *AIAA journal*, Vol. 41, No. 6, 2003, pp. 1055–1063.

[7] Nompelis, I., *Computational study of hypersonic double-cone experiments for code validation*, 2004.

[8] Nompelis, I. and Candler, G., "Investigation of hypersonic double-cone flow experiments at high enthalpy in the lens facility," *45th AIAA Aerospace Sciences Meeting and Exhibit*, 2007, p. 203.

[9] Hao, J., Wang, J., and Lee, C., "Numerical Simulation of High-Enthalpy Double-Cone Flows," *AIAA Journal*, 2017, pp. 1–5.

[10] Holden, M. S. and Wadhams, T., "P.,"Code Validation Study of Laminar Shock/Boundary Layer and Shock/Shock Interactions in Hypersonic Flow Part A: Experimental Measurements," AIAA 2001-1031," *39th AIAA Aerospace Sciences Meeting and Exhibit, Reno, NV, January*, 2001, pp. 8–12.

[11] MacLean, M., Holden, M., and Dufrene, A., "Comparison Between CFD and Measurements for Real-Gas Effects on Laminar Shock Wave Boundary Layer Interaction, 1," *Oral Presentation*, 2014.

[12] Martin, A., Scalabrin, L. C., and Boyd, I. D., "High performance modeling of atmospheric re-entry vehicles," *Journal of Physics: Conference Series*, Vol. 341, No. 1, 2012, pp. 012002.

[13] Scalabrin, L. C., "Numerical simulation of weakly ionized hypersonic flow over reentry capsules," *PhD thesis, University of Michigan*, 2007.

[14] Millikan, R. C. and White, D. R., "Systematics of vibrational relaxation," *The Journal of chemical physics*, Vol. 39, No. 12, 1963, pp. 3209–3213.

[15] Park, C., "Review of chemical-kinetic problems of future NASA missions, I: Earth entries," *Journal of Thermophysics and Heat transfer*, Vol. 7, No. 3, 1993, pp. 385–398.

[16] Nompelis, I., Candler, G., and Holden, M., "Computational investigation of hypersonic viscous/inviscid interactions in high enthalpy flows," *36th AIAA Thermophysics Conference*, 2003, p. 3642.

[17] Nompelis, I. and Candler, G., "Numerical investigation of double-cone flow experiments with high-enthalpy effects," *48th AIAA Aerospace Sciences Meeting Including the New Horizons Forum and Aerospace Exposition*, 2010, p. 1283.

AIAA SciTech Forum
7-11 January 2019, San Diego, California
AIAA Scitech 2019 Forum

10.2514/6.2019-0795

Measurements of Oxygen Vibrational Relaxation and Dissociation Using Ultraviolet Laser Absorption in Shock Tube Experiments

Jesse W. Streicher*, Ajay Krish†, Shengkai Wang‡, David F. Davidson§, and Ronald K. Hanson¶
Stanford University, Stanford, California 94305, USA

Vibrational relaxation and dissociation rates have been measured for oxygen with a variety of collision partners through the use of an ultraviolet laser diagnostic on shock tube facilities. Current results, measured behind incident shock waves for vibrational relaxation and behind reflected shock waves for dissociation, have probed non-equilibrium air chemistry at high oxygen concentrations and at high temperatures. In particular, vibrational relaxation rates for oxygen by collision with argon (Ar) and oxygen (O_2) were measured over temperatures between 2000 and 4000 K. These measurements show agreement with the Millikan and White correlations, but with lower scatter than previous measurements. In addition to vibrational relaxation, the dissociation rates for oxygen by collision with argon and oxygen were measured up to 9000 and 8000 K, respectively. The O_2-Ar and O_2-O_2 dissociation rates show good agreement with previous measurements and models, but with lower scatter.

I. Nomenclature

A	=	preexponential constant in Arrhenius equation
b	=	preexponintial temperature dependence in Arrhenius equation
E_a	=	activation energy, $kcal/mol$
E_V	=	energy in the vibrational mode, J
E_V^*	=	equilibrium energy in the vibrational mode, J
h	=	specific enthalpy, J/kg
I	=	laser beam intensity exiting shock tube, W
I'	=	laser beam intensity entering shock tube, W
I_0	=	incident intensity ratio
I_t	=	transmitted intensity ratio
k_d	=	dissociation rate coefficient (for second order), $cm^3/mol \cdot s$
K_{eq}	=	equilibirum constant for dissociation reaction, mol/cm^3
n_j	=	number density of species j, mol/cm^3
P	=	pressure, atm
P_i	=	initial post-shock pressure, atm
R	=	1.9858775, universal gas constant, $cal/mol \cdot K$
t	=	time, s
T_{eq}	=	equilibrium temperature, K
T_R	=	rotational temperature, K
T_T	=	translational temperature, K
$T_{T,i}$	=	initial post-shock translational temperature, K
T_V	=	vibrational temperature, K
v"	=	lower state vibrational level
v	=	specific volume, m^3/kg

*Graduate Research Assistant, Department of Mechanical Engineering; jessewst@stanford.edu
†Graduate Research Assistant, Department of Mechanical Engineering; krish2@stanford.edu
‡Post-Doctoral Scholar, Department of Mechanical Engineering; sk.wang@stanford.edu
§Senior Research Engineer, Department of Mechanical Engineering; dfd@stanford.edu (Corresponding Author)
¶Professor, Department of Mechanical Engineering; rkhanson@stanford.edu. Fellow AIAA.

X_{O_2} = mole fraction of oxygen
α = absorbance
θ_V = characteristic vibrational temperature, K
μ = reduced mass, $Dalton$
τ_{VT} = relaxation time due to vibrational–translational intermolecular energy transfer, s
τ_{mix} = vibrational relaxation time of oxygen in a mixture of gases, s

II. Introduction

Hypersonic vehicle flight in air is characterized by very high temperatures and chemical non-equilibrium behind bow shocks. Because the energy transfer from these high-temperature flows influences many aspects of high-speed vehicle design, there is a critical need for experimental validation of the chemical kinetics behavior in high-enthalpy hypersonic flows. While many organizations have achieved high-speed flight capabilities, the fundamental physics behind air rovibrational-dissociation and rovibrational-translational relaxation processes are not yet well understood [1–5]. These processes can play a major role in the thermal balance around a hypersonic vehicle, since hypersonic flows typically do not reach chemical or vibrational equilibrium before encountering the surface of the vehicle [6]. Because of the thermal non-equilibrium of the gases in these flows, the rates of these processes must be quantified to more accurately predict heat transfer between non-equilibrium flow and ablative surfaces.

While in some temperature regimes these processes occur on distinct, separate time scales, in many applications they are coupled [7]. The regime in which coupling occurs is not well understood and requires experimental validation of the interactions between vibrational relaxation and dissociation. Direct measurements of these processes in both the coupled and uncoupled regimes will help to validate the heat transfer and fluid flow models used by aircraft designers. Laser absorption diagnostics provide a fast and sensitive method to access unique conditions of these non-equilibrium flows – including the difference between the translational and vibrational temperatures. Because of these criteria, an ultraviolet laser diagnostic, tuned to probe specific quantum states of oxygen, provides unique measurement capabilities for these studies [8, 9]

III. Methods

To measure oxygen vibrational relaxation and dissociation at conditions relevant to hypersonic flight, understanding must be developed for the spectroscopy used to probe the energy levels of oxygen, the experimental setup used to achieve temperatures and pressures of interest, and the models through which the experimental results are interpreted. In this case, an ultraviolet, rovibronic absorption model is presented which applies to both the vibrational relaxation and dissociation measurements. Additionally, a description of the shock tube experimental setup is given which applies to both types of measurements. Finally, separate models for vibrational relaxation and dissociation are presented to provide context for measurements made in regimes where vibrational relaxation and dissociation are uncoupled.

A. Absorption Model

Ultraviolet laser absorption spectroscopy applied to oxygen allows for sensitive probing of energy levels at fast measurement rates, because molecules absorb light corresponding to discrete transitions between energy levels. To make quantitative measurements using absorption spectroscopy, the spectrum must be appropriately modeled in the frequency range of interest. The oxygen absorption transitions investigated in the current work are the ultraviolet transitions in the Schumann-Runge system, specifically at wavelengths between 130 and 270 nm [10, 11]. In this system, oxygen transitions from the ground electronic state ($X^3\Sigma_g^-$) to the second excited electronic level ($B^3\Sigma_u^-$). Fine structure within this band arises from discrete vibrational and rotational levels as well as spin-splitting effects (Fig. 1a) [12]. Since the laser used was spectrally broad compared to these features, much of the hyperfine structure in the Schumann-Runge system is not resolved using the current laser system (Fig. 1b) [8].

In these oxygen bands, the absorption process can result in a combination of discrete and continuous features due to bound-bound and bound-unbound transitions, respectively. This complicates the model of the spectrum as at longer wavelengths continuum features become an increasing fraction of the total absorbance. Additionally, the tendency of the upper state to dissociate along repulsive potential energy curves leads to predissociation, which further complicates the analysis [13, 14]. The absorption model developed for this work follows the procedure developed for previous measurements of oxygen vibrational relaxation and dissociation [8, 9, 15].

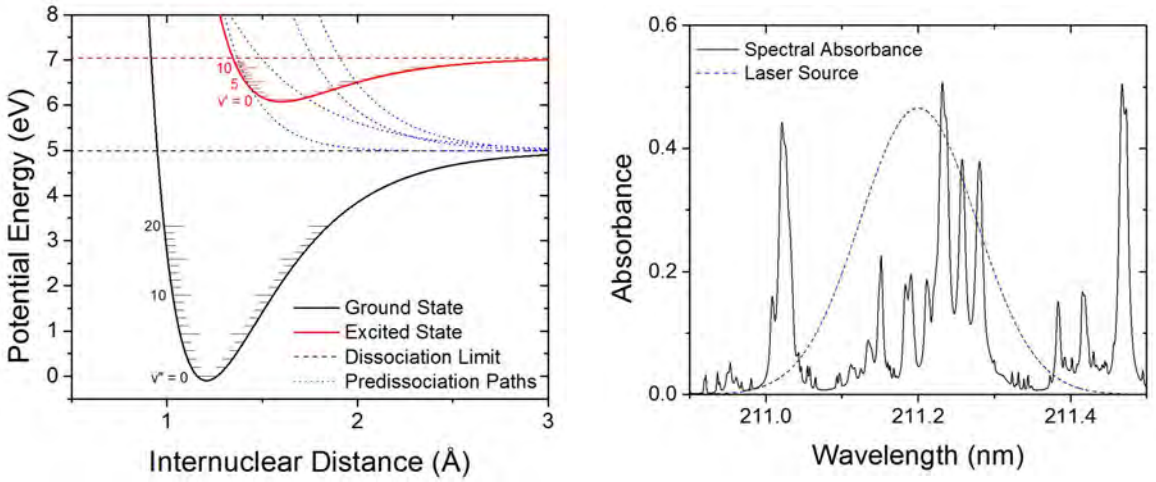

(a) (b)

Fig. 1 Potential energy curves relevant to the Schumann-Runge system (a) and associated absorbance characteristics (b). The ground energy ($X^3\Sigma_g^-$) state transitions to the second excited electronic level ($B^3\Sigma_u^-$). From the excited state, oxygen can decay along the repulsive curves (shown in blue) causing predissociation. Transitions to portions of the upper-state potential energy surface above the dissociation limit cause bound-unbound transitions. The profile of the laser used in these experiments is shown for comparison with absorbance features.

To account for the effects of bound-unbound transitions in the course of experiments, absorbance values, measured immediately behind the shock wave, were used to correct the spectral model. These values were used since there are well-known relations for pressure and temperature across a shock and at early times the gas composition is well known. From these corrections, it was found that bound-unbound transitions play a very minor role at temperatures below 5000 K, but at higher temperatures the spectral model underpredicted absorbance by up to factor of two. The corrected spectral model was used to analyze and interpret the experimental results.

B. Experimental Setup

The conditions necessary to study non-equilibrium air chemistry behind the bow shock of a hypersonic vehicle can be replicated in a shock tube. A shock tube can replicate pressure and temperature conditions which parallel those of both hypersonic and re-entry vehicles, and the passage of a shock wave provides a useful zero-time against which dissociation and vibrational relaxation rates can be measured. When combined with laser absorption spectroscopy, shock tubes can provide high-quality chemical kinetics measurements.

For the current measurements, a 532 nm continuous wave (CW) laser was used to pump a pulsed Ti:Sapphire laser system (Mira HP, Coherent Inc.) (Fig. 2) [16]. The output from this system was frequency quadrupled (FHG, Coherent Inc.) to generate tunable UV light between 210-230 nm with a pulse width of less than 2 ps and a repetition rate of 76 MHz. For the cases presented here, the system was tuned to 211.2 nm to probe the fourth excited vibrational level of the ground state of oxygen (v" = 4). The fundamental output of the Ti:Sapphire laser system had a Gaussian spectral profile with a FWHM of 0.45 nm as measured by a Bristol 721 wavemeter in spectrum analyzer mode. The FWHM output from the Ti:Sapphire laser system would correspond to a FWHM of 0.11 nm for the UV output of the fourth harmonic generator. The measured FWHM falls within the predicted bounds of 0.07 - 0.18 nm, based on the calculated Fourier transform limit and the linewidth measured with a monochromator (Spex 750M) completed in previous work [8, 9]. In these experiments, the fundamental wavelength output of the Ti:Sapphire laser was monitored using the aforementioned Bristol wavemeter. The laser beam was focused at the center of the shock tube to a beam waist less than 0.3 mm with a 25 cm focal length lens to achieve high time resolution measurements.

The beam was split into a reference and transmitted beam to account for intensity fluctuations. In this case, the reference beam was routed to a detector before passing through the test gas while the transmitted beam was routed through the test gas. In all cases, the transmitted beam passed through two UV grade fused silica windows before being focused onto a large collection area detector (New Focus 2032) with a variable bandwidth of either 150 or 900 kHz

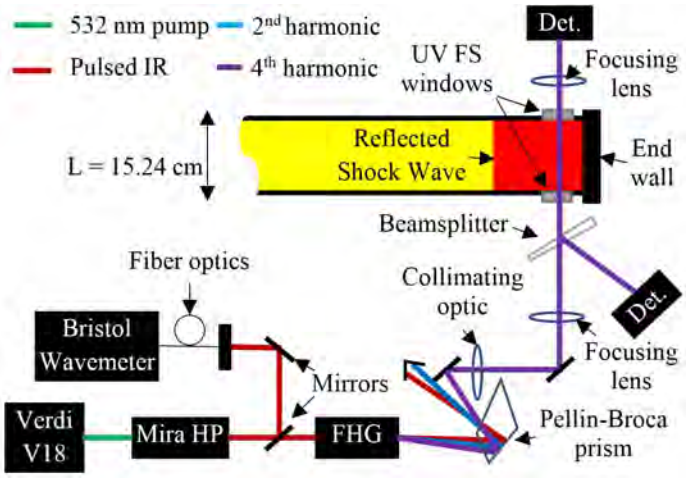

Fig. 2 Layout of UV laser system and shock tube used for vibrational relaxation and dissociation experiments.

that depended on the gain setting. The use of a reference and transmitted beam allowed for a common-mode-rejection scheme for calculating the absorbance (α) from the beam intensity before (I') and after (I) passing through the test gas using Beer's Law (Eq. 1).

$$\frac{I_t}{I_0} = \frac{(I/I')}{(I/I')_0} = e^{-\alpha} \tag{1}$$

In this case, the incident intensity ratio (I_0) was measured before the shock experiment since oxygen has no appreciable absorbance at this wavelength at room temperature. The transmitted intensity ratio (I_t) was measured during the vibrational relaxation and dissociation shock experiments.

While the optical setup was the same, vibrational relaxation experiments were measured behind incident shock waves, whereas the dissociation experiments were measured behind reflected shock waves. This was done to reduce the effects of density change for the vibrational relaxation, and to achieve higher temperatures for the dissociation experiments. For the incident shock vibrational relaxation experiments, the laser measurements were made a distance of 5 cm from the end wall to extend test time. For the reflected shock dissociation experiments, the laser measurements were made a distance of 2 cm from the end wall.

C. Vibrational Relaxation Model

The passage of a shock wave in a gas causes a sudden change in the translational energy modes of a gas. While the translational and rotational energies redistribute to the typical Boltzmann distribution over a few collisions, the vibrational modes transition more slowly from their pre-shock distribution [17]. This leads to a gas which is characterized by two different temperatures, $T_T = T_R$ and T_V for translation/rotation and vibration, respectively. To restore equilibrium, collisions transfer intermolecular energy through rotational–translational, vibrational–translational (VT), and vibrational–vibrational (VV) processes. These transfer processes are called relaxation, and the transfer which equilibrates the vibrational energy with the rotational and translational energy is called vibrational-translational relaxation.

The vibrational-translational process is usually described using the Bethe-Teller equation for a relaxing molecule (Eq. 2) [18]. In this equation, the rate at which relaxation occurs is proportional to the difference between the current vibrational energy (E_V) and the equilibrium vibrational energy (E_V^*). When the vibrational energy is in equilibrium, the vibrational temperature (T_V) is equal to the rotational and translational temperatures ($T_T = T_R$).

$$\frac{dE_v}{dt} = \frac{E_V^*(T_T) - E_V(T_V)}{\tau_{VT}(T_T)} \tag{2}$$

$$ln(P\tau_{VT}) = (-18.42) + (1.16 \times 10^{-3})\mu^{1/2}\theta_V^{4/3}[T_T^{-1/3} - (0.015)\mu^{1/4}] \tag{3}$$

$$\frac{1}{\tau_{VT}^{mix}} = \frac{X_{O_2}}{\tau_{VT}^{O_2-O_2}} + \frac{1 - X_{O_2}}{\tau_{VT}^{O_2-Ar}} \tag{4}$$

Millikan and White developed an expression for VT relaxation that relates the natural logarithm of the pressure multiplied by the vibrational relaxation time to the reduced mass (μ), the characteristic vibrational temperature (θ_V), and the translational temperature (T_T) (Eq. 3) [19]. This relationship correlates well with previous vibrational relaxation measurements [20–22]. In addition to vibrational relaxation due to one collision partner, the relaxation time due to a mixture of gases can be calculated using a mixture rule (Eq. 4). This is particularly relevant to air since it is a multicomponent mixture and determination of the relaxation time requires the use of a mixture rule.

Because the vibrational relaxation experiments were performed behind incident shocks, an additional concern is the distinction between particle time and lab time. Particle time refers to the fact that particles passing through the path of the laser beam were shock heated on a time scale which is longer than that observed by the laser due to the bulk motion of the gas [23]. This is relevant behind the incident shock as the gas has bulk motion toward the end wall. Behind the reflected shock, the gas is very nearly stagnant so lab time and particle time are the same. In cases where there is large density change behind the reflected shock, bulk motion may again need to be taken into account. In the limit of low oxygen concentration where gas density change during the vibrational relaxation process is negligible, the ratio of particle time to lab time is simply the density ratio across the incident shock wave. In the cases of high oxygen concentration, the density change was analyzed using a steady incident shock code developed by collaborators at the University of Michigan [24]. In all cases, the particle time was used to determine the time constant of vibrational relaxation (τ).

D. Dissociation Model

The dissociation of oxygen in high temperature gas can be described by a temperature-dependent form of the Arrhenius relation (Eq. 5). In this expression, there is a separate dissociation rate parameter for the reaction of oxygen with a variety of individual collision partners (Eq. 6). Using the aforementioned absorption model together with a chemical model, quantitative measurements of mole fraction time-histories of oxygen can be determined from experimental data. The time history can then be used to determine the preexponential factor (A) for the Arrhenius expression. Experiments at a variety of temperatures can also allow for measurement of the preexponential temperature dependence (b) and activation energy (E_a) for the Arrhenius expression.

$$k_d = AT^b exp(-\frac{E_a}{RT}) \tag{5}$$

$$O_2 + M \longleftrightarrow O + O + M \qquad\qquad (M = O_2, Ar, O) \tag{6}$$

$$\frac{dn_{O_2}}{dt} = k_d^{O_2-O_2}\left(\frac{n_O^2 * n_{O_2}}{K_{Eq}} - n_{O_2}^2\right) + k_d^{O_2-Ar}\left(\frac{n_O^2 * n_{Ar}}{K_{Eq}} - n_{O_2}n_{Ar}\right) + k_d^{O_2-O}\left(\frac{n_O^3}{K_{Eq}} - n_{O_2}n_O\right) \tag{7}$$

The most general case of oxygen dissociation in argon must include contributions from the reactions with molecular oxygen, argon, and atomic oxygen (Eq. 7). The general case also includes contributions from the recombination reactions through the equilibrium constant (K_{Eq}). However, depending on the mixture under study some of the reactions contribute less than others. For example, dilute experiments in argon isolate the oxygen/argon reaction rate, whereas higher oxygen concentrations provided data for molecular and atomic oxygen. Finally, measurements at early times isolate the forward reaction.

To effectively model the dissociation experiments behind reflected shocks, the data were analyzed subject to energy conservation. For the initial post-shock conditions, the vibrational equilibrium temperature was found using an in-house code which combines a frozen shock solver and a vibrational relaxation model [9, 23]. The composition was determined from either manometric mixing or specified compositions from a manufacturer, whereas the pressure profile was directly measured with a Kistler^{TM} pressure transducer. With the initial temperature, composition, and a prescribed pressure profile, the chemistry rate equation could be solved subject to the enthalpy constraint (Eq. 8).

$$dh = vdP \tag{8}$$

The use of the enthalpy constraint is in contrast to the common constant-internal energy or constant-pressure approximations commonly used in reflected shock wave experiments. The enthalpy was calculated from polynomial fit coefficients which included both sensible and chemical enthalpy components for temperatures up to 20,000 K [25]. The impact of both temperature and composition change was needed to determine dissociation rates from absorbance data.

IV. Results

Measurements were made, behind incident shock waves, of the vibrational relaxation of oxygen over a temperature range of 2000-4000 K and, behind reflected shock waves, of the dissociation of oxygen over a temperature range of 3000-9000 K. These measurements were made in a variety of oxygen and argon mixtures to isolate the effects of collisions with argon and oxygen. For the temperatures and pressures studied, vibrational relaxation and dissociation occurred on distinct time scales which allowed for separate measurements for each process.

A. Vibrational Relaxation Results

The vibrational relaxation of oxygen was studied for collisions with both argon and oxygen. These experiments were measured behind incident shocks to reduce the effects of density change over the course of experiments. The measurements for collisions between oxygen and argon were made in a manufacturer-provided mixture of 1% oxygen in argon, whereas the measurements for collisions in pure oxygen were made in a manufacturer-provided pure oxygen gas sample. An additional set of experiments were performed in a manometrically prepared mixture of 10% oxygen in argon, which provided validation of the mixture rule (Eq. 4).

The value for the vibrational relaxation time constant (τ_{VT}) for collisions with either oxygen or argon was found by fitting an exponential rise to the measured absorbance profile (Fig. 3). In the case of these experiments, the largest source of error was due to fitting uncertainty, with a slight contribution due to the uncertainty in the initial temperature. Specifically, the pressure —as determined by the Kistler pressure transducer —was measured to less than ± 2.5% uncertainty, the initial temperature —as determined by the incident shock speed and shock jump relations —was measured to less than ± 3% uncertainty, and the absorbance fit was measured to less than 12% uncertainty. This combination of uncertainties led to a typical uncertainty in the measured time constant of ± 15%.

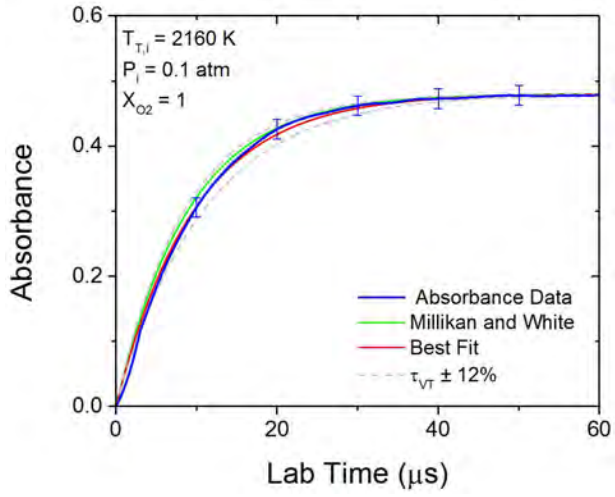

Fig. 3 Comparison of measured absorbance trace for a vibrational relaxation incident shock experiment at 211.2 nm with initial conditions of 2160 K and 0.1 atm in pure oxygen. Measured absorbance trace shows agreement with the values predicted by the Millikan and White correlation [19].

By multiplying the measured vibrational relaxation time by the pressure, the data can be related through a Landau-Teller diagram (Fig. 4a). For the 2000-4000 K measurement range of these experiments, the measured vibrational relaxation rates show agreement with values predicted by the Millikan and White correlation and lower scatter than previous measurements (Fig. 4b) [8, 20–22]. Ultimately, experiments over a wide range of temperatures and measurement techniques all show very close agreement with the Millikan and White correlations [19].

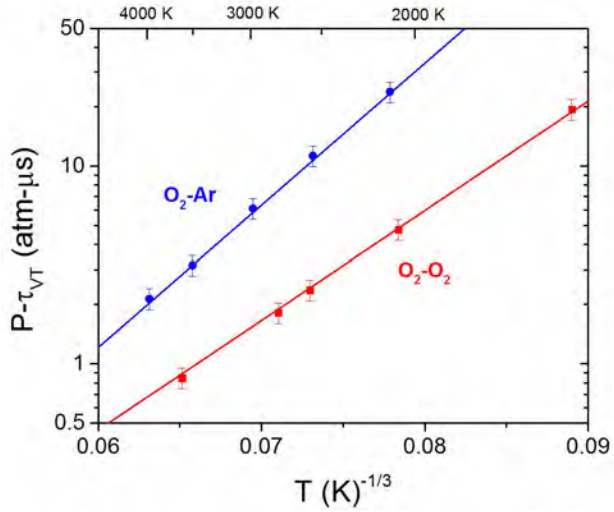

(a)

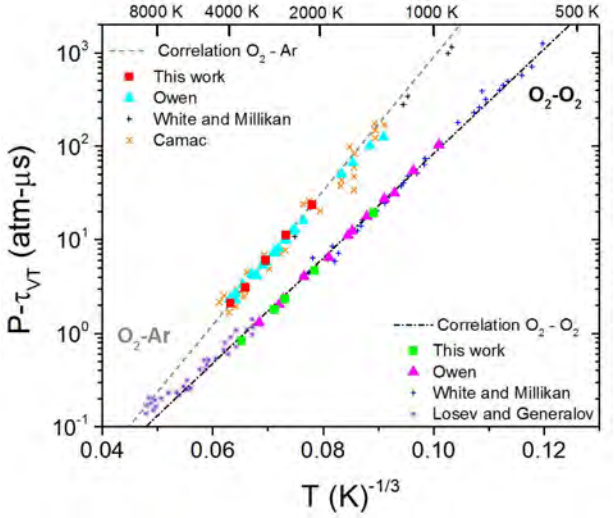

(b)

Fig. 4 Landau-Teller diagrams for this work (a) and comparison with literature values (b). These results agree well with the values predicted by the Millikan and White correlations and show less scatter than previous studies for collisions with both argon and oxygen [8, 19–22].

B. Dissociation Results

The dissociation of oxygen was studied for collisions with argon and oxygen. These experiments were measured behind reflected shocks to access higher temperatures. The measurements for O_2-Ar dissociation were made in a manufacturer-provided mixture of 2% oxygen in argon, whereas the measurements for O_2-O_2 were made in manometrically prepared mixtures of 21% oxygen in argon and 50% oxygen in argon. The non-dilute experiments were run at two different initial oxygen concentrations to compare the role of density change over the course of experiments.

Similar to the vibrational relaxation experiments, the largest source of error was due to fitting uncertainty, with a slight contribution due to the uncertainty in the initial temperature. Again, the pressure was measured to less than ± 2.5% uncertainty and the initial temperature was measured to less than ± 3% uncertainty. In the case of the 2% oxygen in argon experiments, the fitting error was calculated to be less than ± 9%. Typical root-sum-squared uncertainty was determined to be ± 10% based on the uncertainty sources mentioned above.

In the 21% and 50% oxygen-argon experiments, additional uncertainty arose from uncertainty in the oxygen-argon rate and uncertainty in the temperature change over the experiment. Because the oxygen dissociation rate data were

taken from early-time measurements, the temperature change contributed slightly less than in the atomic oxygen data. For the O_2-O_2 reaction, the uncertainty in the experimental fit was calculated to be less than ± 24% with a temperature change uncertainty contributing ± 7%. Overall this resulted in a ± 27% uncertainty for the O_2-O_2 dissociation rate.

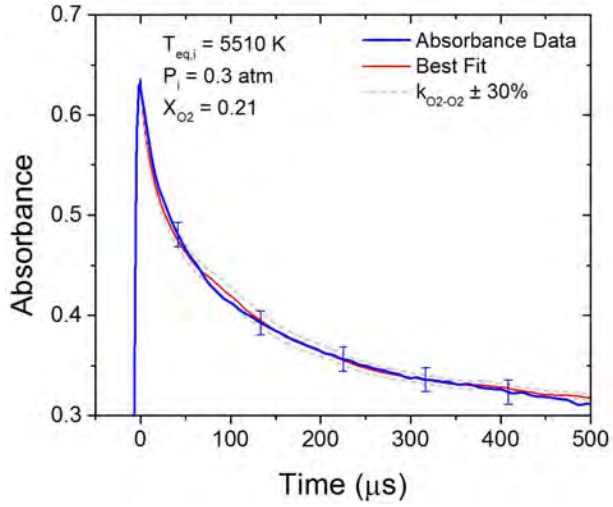

Fig. 5 Comparison of measured absorbance trace for a dissociation reflected shock experiment at 211.2 nm with initial conditions of 5510 K and 0.3 atm in a mixture of 21% oxygen in argon. Rate constant data for O_2-O_2 was inferred from data at early times. Perturbations of $k_{O_2-O_2}$ by ± 30% are shown.

The value for the dissociation constant (k_d) for collisions with argon and oxygen was found by fitting an exponential decay to measured absorbance profiles (Fig. 5). The best-fit absorbance profile was found by modeling the chemistry constrained by the enthalpy equation and the measured pressure (Eq. 7 and 8). For the 2% oxygen in argon experiments, the reaction rate for oxygen-argon collisions could be determined directly from an exponential fit, since there was much less temperature change over the experiment. This set of experimental results were then used in the 21% and 50% experiments to constrain the oxygen-argon reaction rate (k_{d,O_2-Ar}). For the 21% and 50% experiments, the rate for molecular oxygen (k_{d,O_2-O_2}) was measured at early times.

The results for all the dissociation experiments completed in this study were compiled into an Arrhenius diagram which relates the dissociation rate to the inverse of temperature (Fig. 6a). As expected, the measured rate for oxygen-argon collisions is slower than that of oxygen-oxygen. Finally, each reaction rate was compared to literature values for the rate coefficient.

For the O_2-Ar reaction rate, the measured values in this study agreed with previously measured values, but with lower scatter (Fig. 6b). While measurements in this study were not completed to temperatures as high as prior studies, the reduced scatter and uncertainty in these measurements provide a valuable comparison to model results. Additional studies to higher temperatures will require investigation into the coupling of vibrational relaxation and dissociation.

For the O_2-O_2 reaction rate, the measured values agree with both low- and high-temperature results from literature, but with lower scatter than previous measurements (Fig. 6c). These measurements agree within experimental error to models proposed by Baulch et al. and Park at temperatures less than 6000 K, but at higher temperatures, these measurements are in better agreement with the expressions proposed by Park [30, 31].

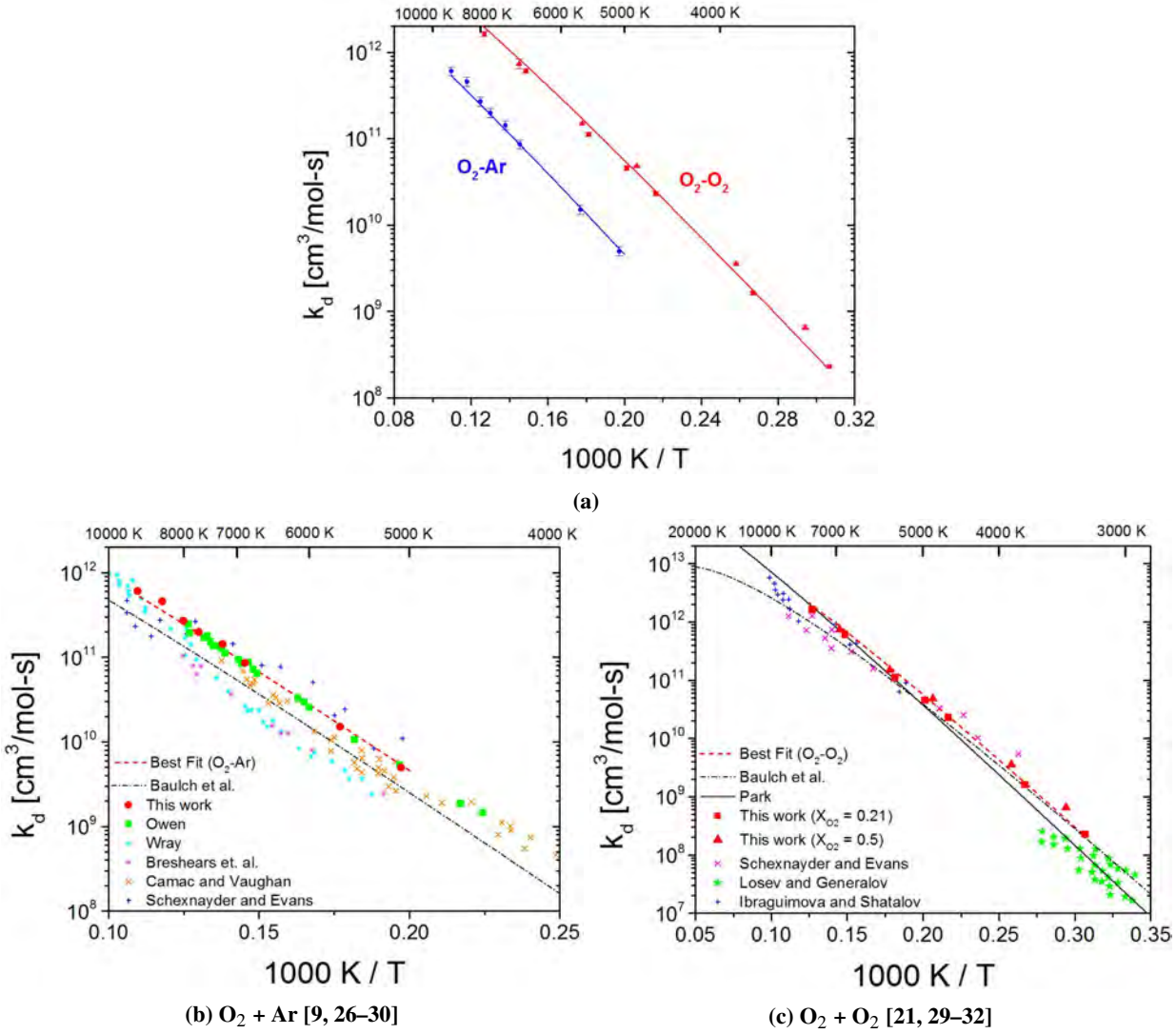

Fig. 6 Arrhenius diagrams for this work (a) and comparison with literature values for O_2-Ar (b) and O_2-O_2 (c) [9, 21, 26–32].

V. Conclusion

Oxygen vibrational relaxation and dissociation rates were measured using an ultraviolet laser diagnostic on shock tube facilities. These measurement were made to isolate reactions with argon and oxygen. These experiments, measured behind incident shock waves for vibrational relaxation and behind reflected shock waves for dissociation, have probed non-equilibrium air chemistry at increased oxygen concentrations and at high temperatures.

In line with the current UV laser absorption measurement, a spectral model was developed for oxygen in the Schumann-Runge bands near 211.2 nm. This model was used for quantitative measurements on a shock tube using a pulsed, tunable, ultraviolet laser diagnostic. Finally, the shock tube absorption results were interpreted via models for vibrational relaxation and dissociation to measure non-equilibrium rates relevant to hypersonic flows.

This work has measured the vibrational relaxation of oxygen behind incident shocks in the 2000-4000 K range for collisions with argon and oxygen. These measurements show agreement with the Millikan and White correlations, but with lower scatter than many previous measurements. This work has also measured dissociation rates for oxygen behind reflected shocks in the 3000-9000 K range for collisions with argon and oxygen. The O_2-Ar and O_2-O_2 dissociation rates were measured up to 9000 and 8000 K respectively with lower scatter than previous studies.

Acknowledgments

The authors would like to thank Dr. K. Hanquist and Prof. I. Boyd in the aerospace engineering department at the University of Michigan for assistance in modeling test conditions behind incident shock wave using their two-temperature code. This work was supported by the Air Force Office of Scientific Research through AFOSR grant FA9550-16-1-0291 with contract monitor Dr. I. Leyva.

References

[1] Hank, J., Murphy, J., and Mutzman, R., "The X-51A Scramjet Engine Flight Demonstration Program," *15th AIAA International Space Planes and Hypersonic Systems and Technologies Conference*, , No. May, 2008, pp. 1–13.

[2] Walker, S., Sherk, J., Shell, D., Schena, R., Bergmann, J., and Gladbach, J., "The DARPA/AF Falcon Program: The Hypersonic Technology Vehicle #2 (HTV-2) Flight Demonstration Phase," *15th AIAA International Space Planes and Hypersonic Systems and Technologies Conference*, Vol. 2, No. May, 2008, pp. 1–9.

[3] Dolvin, D., "Hypersonic International Flight Research and Experimentation Technology Development and Flight Certification Strategy," *16th AIAA/DLR/DGLR International Space Planes and Hypersonic Systems and Technologies Conference*, 2009.

[4] Kimmel, R.L., and Adamczak, D., "Hypersonic International Flight Research and Experimentation (HIFiRE) Fundamental Science and Technology Development Strategy," , No. May, 2008, pp. 1–11.

[5] Urzay, J., "Supersonic Combustion in Air-Breathing Propulsion Systems for Hypersonic Flight," *Annual Revew of Fluid Mechanics*, Vol. 50, No. 1, 2018, pp. 593–627.

[6] Martin, A., Scalabrin, L. C., and Boyd, I. D., "High performance modeling of atmospheric re-entry vehicles," *Journal of Physics: Conference Series*, Vol. 341, No. 1, 2012.

[7] Josyula, E., and Bailey, W. F., "Vibration-Dissociation Coupling Using Master Equations in Nonequilibrium Hypersonic Blunt-Body Flow," *Journal of Thermophysics and Heat Transfer*, Vol. 15, No. 2, 2001, pp. 157–167.

[8] Owen, K. G., Davidson, D. F., and Hanson, R. K., "Oxygen Vibrational Relaxation Times: Shock Tube/Laser Absorption Measurements," *Journal of Thermophysics and Heat Transfer*, Vol. 30, No. 4, 2016, pp. 791–798.

[9] Owen, K. G., Davidson, D. F., and Hanson, R. K., "Measurements of Oxygen Dissociation Using Laser Absorption," *Journal of Thermophysics and Heat Transfer*, Vol. 30, No. 2, 2016, pp. 274–278.

[10] Bykova, N. G., and Kuznetsova, L. A., "Study of the absorption characteristics of molecular oxygen in the Schumann-Runge system at high temperatures: I. Calculations of absorption spectra," *Optics and Spectroscopy*, Vol. 105, No. 5, 2008, pp. 668–673.

[11] Krupenie, P. H., "The Spectrum of Molecular Oxygen," *Journal of Physical and Chemical Reference Data*, Vol. 423, No. 1972, 2015.

[12] Blake, A. J., "An Atmospheric Absorption Model for the Schumann-Runge Bands of Oxygen," *Journal of Geophysical Research*, Vol. 84, No. 8, 1979, pp. 1–6.

[13] Lewis, B. R., Berzins, L., Carver, J. H., and Gibson, S. T., "Rotational variation of predissociation linewidth in the Schumann-Runge bands of16O2," *Journal of Quantitative Spectroscopy and Radiative Transfer*, Vol. 36, No. 3, 1986, pp. 187–207.

[14] Ben-Aryeh, Y., "Broadening and shifts of molecular spectral lines by predissociation," *Journal of Quantitative Spectroscopy and Radiative Transfer*, Vol. 13, No. 12, 1973, pp. 1441–1463.

[15] Herzberg, G., *Molecular Spectra and Molecular Structure I. Spectra of Diatomic Molecules*, 2nd ed., Krieger Publishing Company, Malabar, FL, 1950.

[16] Hong, Z., Lam, K. Y., Davidson, D. F., and Hanson, R. K., "Broad-linewidth laser absorption measurements of oxygen between 211 and 235nm at high temperatures," *Journal of Quantitative Spectroscopy and Radiative Transfer*, Vol. 112, No. 17, 2011, pp. 2698–2703.

[17] Blackman, V., "Vibrational relaxation in oxygen and nitrogen," *Journal of Fluid Mechanics*, Vol. 1, No. 1, 1956, pp. 61–85.

[18] Bethe, H., and Teller, E., "Deviations From Thermal Equilibrium in Shock Waves," , 1941.

[19] Millikan, R. C., and White, D. R., "Systematics of vibrational relaxation," *The Journal of Chemical Physics*, Vol. 39, No. 12, 1963, pp. 3209–3213.

[20] White, D. R., and Millikan, R. C., "Vibrational relaxation of oxygen," *The Journal of Chemical Physics*, Vol. 39, No. 7, 1963, pp. 1803–1806.

[21] Losev, S. A., and Generalov, N. A., "A Study of the Excitation of Vibrations and Dissociation of Oxygen Molecules at High Temperatures," *Soviet Physics Doklady*, Vol. 6, 1962, p. 1081.

[22] Camac, M., "O2 vibration relaxation in oxygen-argon mixtures," *The Journal of Chemical Physics*, Vol. 34, No. 2, 1961, pp. 448–459.

[23] Gaydon, A. G., and Hurle, I. R., *The Shock Tube in High Temperature Chemical Physics*, Reinhold, 1963, p. 13–14.

[24] Andrienko, D. A., and Boyd, I. D., "High fidelity modeling of thermal relaxation and dissociation of oxygen," *Physics of Fluids*, Vol. 27, No. 11, 2015.

[25] McBride, B. J., Zehe, M. J., and Gordon, S., "NASA Glenn Coefficients for Calculating Thermodynamic Properties of Individual Species," *Technical report NASA*, Vol. 211556, No. September, 2002, p. 291.

[26] Camac, M., and Vaughan, A., "O2dissociation rates in O2-Ar mixtures," *The Journal of Chemical Physics*, Vol. 34, No. 2, 1961, pp. 460–470.

[27] Wray, K. L., "Shock-tube study of the coupling of the O2-Ar rates of dissociation and vibrational relaxation," *The Journal of Chemical Physics*, Vol. 37, No. 6, 1962, pp. 1254–1263.

[28] Breshears, W. D., Bird, P. F., and Kiefer, J. H., "Density Gradient Measurements of O2 Dissociation in Shock Waves," *The Journal of Chemical Physics*, Vol. 55, No. 8, 1971, pp. 4017–4026.

[29] Schexnayder Jr., C. J., and Evans, J. S., "Measurements of the Dissociation Rate of Molecular Oxygen," *NASA Technical Report R-108*, 1961.

[30] Baulch, D. L., Drysdale, D. D., Duxbury, J., and Grant, S. J., *O2 M → O O M*, University of Leeds, 1976, Vol. 3, p. 11–32.

[31] Park, C., *Nonequilibrium hypersonic aerothermodynamics*, 1989.

[32] Ibraguimova, L. B., Shatalov, O. P., and Tunik, Y. V., "Equilibrium and non-equilibrium rate constants of oxygen dissociation at high temperatures," *AIP Conference Proceedings*, Vol. 1501, No. 1, 2012, pp. 1094–1101.

Shock-Tube Measurements of Vibrational Relaxation Times in Oxygen and Nitrogen Mixtures Using Ultraviolet Laser Absorption Spectroscopy

Jesse W. Streicher*, Ajay Krish†, and Ronald K. Hanson‡
Stanford University, Stanford, California 94305, USA

Vibrational relaxation times were measured behind reflected shocks in shock-tube experiments for mixtures of 10% and 21% oxygen (O_2) in nitrogen (N_2) at temperatures of 2000-4000 K and sub-atmospheric pressures. To determine relaxation times, a tunable, pulsed ultraviolet laser absorption diagnostic probed time-histories involving the fourth (v'' = 4) and fifth (v'' = 5) vibrational levels of the ground electronic state of O_2. By taking the ratio of absorbance involving these vibrational levels, the vibrational temperature time-histories were isolated from the absorbance time-histories. Finally, the temperature time-histories were fit to determine the vibration-translation (V-T) and vibration-vibration (V-V) relaxation times of O_2 with N_2. Data for $\tau_{VT}^{O_2-N_2}$ exceeds the Millikan and White correlation by about 70% but shows reasonable agreement with previous data, and data for $\tau_{VV}^{O_2-N_2}$ also exceeds the semi-empirical relational developed by Berend et al. by 70%. The V-V relaxation times also determined the probability of vibrational energy transfer, ${}^{N_2}_{O_2}Q^{1,0}_{0,1}$, and these results exhibit lower scatter than previous studies. While previous studies used interferometry, emission, and broadband UV absorption, this study demonstrates the first application of laser absorption spectroscopy to the determination of vibrational relaxation times in mixtures of O_2 and N_2.

I. Nomenclature

E_V	=	energy in the vibrational mode, J
E_V^*	=	equilibrium energy in the vibrational mode, J
h	=	specific enthalpy, J/kg
I	=	laser beam intensity exiting shock tube, W
I'	=	laser beam intensity entering shock tube, W
I_0	=	incident intensity ratio
I_t	=	transmitted intensity ratio
L	=	absorbing path length, cm
$[M]$	=	concentration of collision partner, mol/cm^3
n_j	=	number density of species j, cm^{-3}
P	=	pressure, atm
${}^iP^{1,0}$	=	Probability per collision of V-T energy transfer, $coll^{-1}$
${}^i_jQ^{1,0}_{0,1}$	=	Probability per collision of V-V energy transfer from species i to species j, $coll^{-1}$
R	=	universal gas constant, J/K
t	=	time, s
T_{tr}	=	translational/rotational temperature, K
T_v^j	=	vibrational temperature of species j, K
v	=	specific volume, m^3/kg
v"	=	lower-state vibrational level
X_j	=	normalized vibrational energy difference of species j, $\frac{E_V^*-E_V}{E_V^*}$
Z	=	bimolecular collision frequency, $cm^3/mol \cdot s$

*Graduate Research Assistant, Department of Mechanical Engineering; jessewst@stanford.edu
†Graduate Research Assistant, Department of Mechanical Engineering; krish2@stanford.edu
‡Professor, Department of Mechanical Engineering; rkhanson@stanford.edu. Fellow AIAA.

α = absorbance
Θ_V = characteristic vibrational temperature, K
θ_j = normalized vibrational temperature of species j, $\frac{\Theta_{V,j}}{T_V}$
μ = reduced mass, $Dalton$
σ = absorption cross-section, cm^2
τ_{VT}^{i-j} = vibration–translation relaxation time for intermolecular energy transfer to species i from species j, s
τ_{VV}^{i-j} = vibration–vibration relaxation time for intermolecular energy transfer to species i from species j, s
Ψ_j = mole fraction of species j, $\frac{N_j}{N}$

II. Introduction

Vibrational nonequilibrium behind shock waves influences the thermal state of air throughout the flow-field around hypersonic and reentry vehicles. At sufficiently high temperatures, this nonequilibrium leads to a coupling between vibrational relaxation and dissociation [1–3]. Though hypersonic flight has been achieved by many organizations, uncertainty in vibrational energy transfer rates continues to limit the design of hypersonic vehicles [4–8]. Specifically, discrepancies between computational models and ground tests demonstrate the need for experimental validation of the elementary vibrational energy transfer and chemical kinetic rate parameters used in these models. A recent example of this discrepancy between models and experiments arose when comparing heat flux measurements and CFD predictions in double cone experiments [9–14]. Experimentally validating vibrational energy transfer rates by measuring vibrational relaxation times increases the predictive capabilities of CFD models. This work isolated low-uncertainty vibrational relaxation times for use in state-to-state models and for implementation in CFD codes.

The various pathways for exchanging translational and vibrational energy between O_2 and N_2 present a major difficulty when studying vibrational relaxation in air. Along with the four vibrational-translation exchanges rates and the one vibration-vibrational exchange rate, the vibrational energies of both O_2 and N_2 change significantly and at different rates. Isolating any one of these rates requires careful experimental planning and sensitive diagnostics. Self-exchange V-T relaxation times prove relatively straightforward to measure in samples of pure O_2 or pure N_2, but the exchange between O_2 and N_2 presents a larger diagnostic challenge. Previous measurements of vibrational relaxation times in mixtures of O_2 and N_2 used interferometry, emission, and broadband UV light absorption [15–24]. With the exception of the broadband UV aborption studies, all previous work relied on measuring relaxation times across a wide range of mixture compositions. These studies necessitated assumptions of the N_2-O_2 V-T exchange rates to isolate the V-V relaxation times. Though these data have been used for many years, they lack the specificity needed for state-to-state models and exhibit high scatter. The use of an ultraviolet laser diagnostic to measure vibrational relaxation times in mixtures of O_2 and N_2 probes specific vibrational levels of O_2 with lower uncertainty and scatter.

III. Methods

In the following sections, the experimental setup describes the equipment used to measure absorbance time-histories, the vibrational relaxation model explains the rate equations for vibrational energy transfer, and the data analysis shows how experimental data lead to vibrational relaxation times.

A. Experimental Setup

A 15.24 cm internal diameter, electropolished, stainless steel, pressure-driven shock tube produced the required temperature and pressure conditions to study vibrational relaxation in O_2-N_2 mixtures (Fig. 1). The driver section was filled with mixtures of helium and nitrogen, whereas the driven section was filled with either a mixture of 10% or 21% O_2 in N_2 prepared manometrically. A thin plastic diaphragm separated these two sections. The diaphragm thickness and driver gas composition were changed to obtain shocks of the desired strength. Before each experiment, rotary pumps and a turbomolecular pump evacuated the driven section to ultimate pressures of less than 2×10^{-5} Torr as measured by a hot-filament ionization gauge. This ionization gauge also measured the leak rate before each shock experiment. Typical leak rates were 2×10^{-4} Torr/min with no case exceeding 4×10^{-4} Torr/min.

In each experiment, pressure measurements determined the initial shock velocity and monitored the pressure time-history. The initial fill pressure was measured using a 0-100 Torr capacitance manometer, whereas a 0-3000 psia capacitance manometer measured the diaphragm burst pressure. For this study, the fill pressures ranged from 0.35 to 6.00 Torr, and the burst pressures typically fell between 38-42 psia. Four piezoelectric pressure transducers,

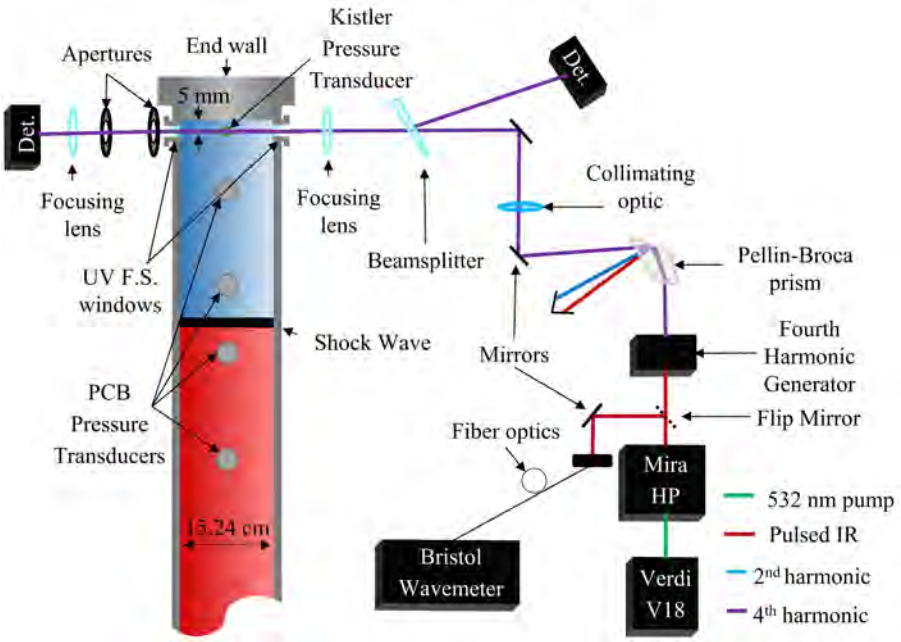

Fig. 1 Layout of the pulsed, tunable UV laser system and shock tube. Common-mode rejection accounted for intensity fluctuations of the laser system. Focusing optics restricted the beam to a narrow beam waist that allowed for high time resolution.

spaced along the length of the shock tube, measured the shock velocity (Fig. 1). These four transducers provided three shock velocity measurements that were extrapolated to the end wall and accounted for shock attenuation. Typical shock attenuation rates were less than 0.5%/m. The measured shock velocity, interpreted with an in-house reflected shock code, allowed calculation of the post-reflected shock initial translational/rotational temperature to within 1% accuracy [25]. After the passage of the incident and reflected shock, a low-noise piezoelectric pressure transducer measured the experimental pressure time-history.

To measure absorbance, a tunable, pulsed UV laser system probed multiple vibrational levels of oxygen in shock-tube experiments. A 532 nm continuous-wave laser pumped a Ti:Sapphire crystal, yielding pulsed IR light between 700-1000 nm that was then frequency-quadrupled to generate tunable UV light between 210-250 nm (Fig. 1). The UV output had a pulse width of less than 2 ps and a repetition rate of 76 MHz. For the cases presented here, the system was tuned to 211.2 nm to probe the fourth excited vibrational level of the ground electronic state of oxygen (v" = 4) and to 221.6 nm to probe the fifth (v" = 5). An absorbance model informed these wavelength choices and assisted with interpreting the absorbance results [26–30]. As the laser system was pulsed, the laser output was spectrally broad compared to spectral features and needed monitoring. The fundamental output of the laser had a Gaussian spectral profile with a full-width at half-maximum (FWHM) between 0.4 - 0.5 nm as measured by a Bristol 721 wavemeter in spectrum analyzer mode. The fourth harmonic had a Gaussian spectral profile with a FWHM between 0.07 - 0.18 nm, based on the calculated Fourier transform limit and the linewidth measured with a monochromator [28]. In addition to the FWHM, the fundamental wavelength was monitored using the same Bristol wavemeter, and measurements of the output profile were taken before and after each shock experiment to account for any drift over the course of the experiment [26].

The setup was optimized to reduce non-ideal optical effects that limit shock tube studies. For example, the laser beam was focused at the center of the shock tube to a beam waist less than 0.3 mm with a 25 cm focal length lens to achieve high time resolution measurements. Accounting for beam thickness, beam skew, shock thickness, and shock curvature, the time resolution of the shock passage was better than 2 μs. Additionally, apertures placed at the exit window and before each detector reduced the effects of emission. A similar setup was previously used to study the vibrational relaxation and dissociation of oxygen [27, 28, 31]. To counter fluctuations in the laser output power, the detectors were arranged in a common-mode rejection setup in which the reference beam was routed to a detector before passing through the test gas while the transmitted beam was routed through the test gas. The transmitted beam passed through two UV grade fused silica windows before focusing onto a large collection area detector with a variable

bandwidth of either 150 or 900 kHz that depended on the gain setting. This study employed the low-gain setting to access the 900 kHz bandwidth. From this common-mode rejection scheme, the absorbance (α) was calculated from the beam intensity before (I') and after (I) passing through the test gas using the Beer-Lambert relation for a common-mode rejection setup (Eq. 1).

$$\frac{I_t}{I_0} = \frac{(I/I')_t}{(I/I')_0} = \exp(-\alpha) = \exp(n_i \sigma L) \tag{1}$$

Since the laser power could fluctuate over the course of the experiment, the absorbance was calculated by comparing the transmitted intensity ratio, $(I/I')_t$, to a non-absorbing incident intensity ratio, $(I/I')_0$. For both ratios, the intensity measured after passing through the shock tube (I) was normalized by the intensity measured prior to passing through the shock tube (I'). The incident intensity ratio (I_0) was measured before the shock experiment as oxygen has no appreciable room-temperature absorbance at experimental wavelengths. The transmitted intensity ratio (I_t) was measured during the vibrational relaxation experiments. Ultimately, the common-mode rejection setup allows for the measurement of absorbance for a laser system with fluctuations of output power.

B. Vibrational Relaxation Model

Vibrational nonequilibirum behind the passage of a shock wave arises because the translational and rotational energies rapidly redistribute to new Boltzmann distributions over a few collisions, while the vibrational modes transition more slowly from their pre-shock distribution [24]. This causes the energy states of the gas to be characterized by two different temperatures, T_{tr} and T_v, for translation/rotation and vibration respectively. To restore equilibrium, molecules undergo vibration–translation (V-T), and vibration–vibration (V-V) energy transfer processes. These transfer processes are called relaxation, and the transfer that equilibrates the vibrational energy with the rotational and translational energies is called vibrational relaxation. In air, the vibrational relaxation occurs via contributions from both V-T and V-V transfer processes, but the V-V transfer especially impacts the system by speeding up the relaxation of N_2 through V-V transfer with O_2.

The V-T process is described by the Bethe-Teller equation for a relaxing molecule (Eq. 2) [32]. In this equation, the rate at which relaxation proceeds is proportional to the difference between the current vibrational energy (E_V) and the equilibrium vibrational energy (E_V^*). When the vibrational energy is in equilibrium, the vibrational temperature is equal to the rotational and translational temperatures ($T_v = T_{tr}$). Millikan and White developed an expression for V-T relaxation that relates the natural logarithm of the pressure multiplied by the vibrational relaxation time ($P\tau_{VT}$) to the reduced mass (μ), the characteristic vibrational temperature (Θ_V), and the translational temperature (T_{tr}) (Eq. 3) [15]. This correlation works well for many diatomic species, though it has been observed to break down at higher temperatures [15, 33]. Additionally, some collision partner combinations – O_2-O_2 V-T times in particular – require corrections to the 1.16×10^{-3} term [15].

$$\frac{dE_V}{dt} = \frac{E_V^*(T_{tr}) - E_V(T_v)}{\tau_{VT}(T_{tr})} \tag{2}$$

$$\ln(P\tau_{VT}) = (-18.42) + (1.16 \times 10^{-3})\mu^{1/2}\Theta_V^{4/3}[T_{tr}^{-1/3} - (0.015)\mu^{1/4}] \tag{3}$$

The combination of V-T and V-V processes is typically described through a combination of non-dimensionalized differential equations (Eqs. 4, 5) [16, 19, 23, 24]. In these equations, the first term on the right represents the contribution due to V-T transfer. Specifically the terms in parenthesis represents the mixture rule for V-T relaxation times, and X_{O_2} denotes the non-dimensional value of the vibrational energy difference. In fact, the Bethe-Teller equation can be expressed in a non-dimensional form using this first term (Eq. 2). The second term in Eqs. 4 and 5 represents the V-V energy exchange. While generally a complex mathematical expression, the rate of V-V energy exchange is clearly determined by the composition (Ψ), the characteristic vibrational temperatures (θ), and a relaxation time ($\tau_{VV}^{O_2-N_2}$). In this case, the rate of vibrational transfer between O_2 and N_2 depends on non-dimensional vibrational energy of both species. When one species equilibrates faster than the other, the V-V exchange term account for transfer from the more equilibrated species to the less equilibrated species. In air, O_2 vibrationally relaxes through V-T collisions much faster than N_2. In this case, the V-V exchange involves energy transfer from O_2 to N_2 through V-V exchange. This V-V exchange significantly increases the rate of N_2 relaxation.

$$-\frac{dX_{O_2}}{dt} = \left(\frac{\Psi_{O_2}}{\tau_{VT}^{O_2-O_2}} + \frac{\Psi_{N_2}}{\tau_{VT}^{O_2-N_2}}\right)X_{O_2} - \frac{\Psi_{N_2}}{\tau_{VV}^{O_2-N_2}}\left(\frac{X_{N_2}(1-X_{O_2})}{1-e^{-\theta_{O_2}}} - \frac{X_{O_2}(1-X_{N_2})}{1-e^{-\theta_{N_2}}}\right)(1-e^{-\theta_{O_2}}) \tag{4}$$

$$-\frac{dX_{N_2}}{dt} = \left(\frac{\Psi_{N_2}}{\tau_{VT}^{N_2-N_2}} + \frac{\Psi_{O_2}}{\tau_{VT}^{N_2-O_2}}\right)X_{N_2} + \frac{\Psi_{O_2}}{\tau_{VV}^{O_2-N_2}}\frac{e^{\theta_{N_2}}}{e^{\theta_{O_2}}}\left(\frac{X_{N_2}(1-X_{O_2})}{1-e^{-\theta_{O_2}}} - \frac{X_{O_2}(1-X_{N_2})}{1-e^{-\theta_{N_2}}}\right)(1-e^{-\theta_{N_2}}) \tag{5}$$

In the above equations, the V-V relaxation process was expressed in terms of vibrational transfer to O_2 from N_2 using $\tau_{VV}^{O_2-N_2}$. However, this choice was somewhat arbitrary, as these equations could instead use the vibrational transfer to N_2 from O_2 using $\tau_{VV}^{N_2-O_2}$. These two quantities directly relate to each other through the probability of vibrational energy transfer, ${}_j^iQ_{0,1}^{1,0}$. Vibrational relaxation times are often expressed in terms of quantum transition probabilities, but for V-V exchange, the probabilities relate via the normalized characteristic vibrational temperature, θ_j (Eqs. 6 - 8).

$$\tau_{VT}^{i-j} = \frac{1}{Z[M]^iP^{1,0}} \tag{6}$$

$$\tau_{VV}^{i-j} = \frac{1}{Z[M]_j^iQ_{0,1}^{1,0}} \tag{7}$$

$${}_j^iQ_{0,1}^{1,0} = {}_i^jQ_{0,1}^{1,0} \times \frac{e^{\theta_i}}{e^{\theta_j}} \tag{8}$$

Both the V-T and V-V relaxation times relate to the bimolecular collision frequency factor, Z, the concentration of collision partner, [M], and the probability of vibrational energy transfer (Eqs. 6, 7) [23]. For V-T relaxation, the relevant probability is the probability of collisional de-excitation from the first to the ground vibrational state, ${}^iP^{1,0}$. In contrast, the relevant probability for V-V relaxation is the probability of collisional de-excitation of species i with the collisional excitation of species j. The inverse process, de-excitation of j with excitation of i, directly relates via the characteristic vibrational temperatures of the two species (Eq. 8). This explains the extra ratio of exponential terms in Eq. 5. Because the characteristic temperature of O_2 (2270 K) is lower than that of N_2 (3390 K), the probability ${}_{N_2}^{O_2}Q_{0,1}^{1,0}$ is less than the probability ${}_{O_2}^{N_2}Q_{0,1}^{1,0}$ and the V-V relaxation time $\tau_{VV}^{O_2-N_2}$ is greater than $\tau_{VV}^{N_2-O_2}$. In this work, the V-V relaxation times are presented as $\tau_{VV}^{O_2-N_2}$, whereas the probabilities are presented as ${}_{O_2}^{N_2}Q_{0,1}^{1,0}$ to provide a direct comparison to previous work [23].

C. Data Analysis

Experiments collected absorption time-histories from two silicon optical detectors, shock velocity measurements from four piezoelectric pressure transducers, and pressure time-histories from a low-noise piezoelectric pressure transducer. The following sections detail how the data were reduced to determine vibrational temperature time-histories, relaxation times, and the associated uncertainty in each of these measurements.

1. Time-Histories

For each experiment, laser intensity was measured using two silicon optical detectors arranged in a common-mode rejection scheme (Fig. 1). The signals from each detector were further interpreted via the Beer-Lambert relation to determine absorbance time-histories (Eq. 1). However, the determination of vibrational temperature from absorbance time-histories required the measurement of absorbance at two wavelengths that probed different vibrational levels. Previous spectroscopic analysis determined that 211.2 nm involves a high percentage of transitions originating in v" = 4, wheres 221.6 involves a high percentage of transitions originating in v" = 5 [26]. Additionally, the absorption cross-section, σ, in the Schumann-Runge system was determined to be a strong function of vibrational temperature with only a very slight dependence on translational temperature. Therefore these wavelengths were identified as a sensitive combination to measure vibrational temperature between 2000 and 4000 K. The vibrational temperature was measured using the ratio of absorbance at these two wavelengths, and the ratio was interpreted via the aforementioned absorption model (Eq. 9) [26].

$$Ratio = \frac{\alpha_{\lambda_1}}{\alpha_{\lambda_2}} = \frac{\sigma_{\lambda_1}(T_v, T_{tr})}{\sigma_{\lambda_2}(T_v, T_{tr})} \tag{9}$$

Since the laser system could only track one wavelength during a given experiment, the measurement of vibrational temperature required closely matched shock experiments. Careful reproduction of initial conditions ensured close temperature and pressure agreement for each pair of matched experiments. Typical shock experiments matched to within 25 K with no pair of matched shocks differing by more than 40 K. Similarly, the pressures matched to within 0.005 atm. Matching these experiments significantly reduced the uncertainty in the absorbance ratio, thereby reducing vibrational temperature uncertainty.

In addition to measuring the vibrational temperature, translational/rotational temperature was tracked using energy conservation. As previously mentioned, the initial value of T_{tr} was determined with the shock-jump equations assuming frozen chemistry and frozen vibrational modes [25]. The translational temperature evolved behind the reflected shock due to the endothermic vibrational relaxation process, but also due to non-ideal pressure effects in the shock tube. In this case, the measured pressure time-history was used to update the energy equation through changes in enthalpy (Eq. 10).

$$dh = vdP \tag{10}$$

Coefficients from the NASA Glenn polynomials determined the mixture enthalpy for this calculation[34]. However, these polynomials assume thermal equilibrium, so contributions due to vibrational energy were adjusted to reflect the non-equilibrium experimental conditions. This adjustment required subtracting the vibrational energy at T_{tr} and then adding the contributions at T_v. While the vibrational temperature of O_2 was directly probed with the laser absorption diagnostic, this calculation relied on the Millikan and White correlation values of V-T relaxation times for $\tau_{VT}^{N_2-O_2}$ and $\tau_{VT}^{N_2-N_2}$ to determine the vibrational temperature of N_2.

2. Relaxation Times

While the vibrational relaxation of air involves five relaxation times, this study fit vibrational temperature time histories to obtain data for $\tau_{VT}^{O_2-N_2}$ and $\tau_{VV}^{O_2-N_2}$. Results from previous experimental studies were leveraged to obtain a functional form of the two self-relaxation times, $\tau_{VT}^{N_2-N_2}$ and $\tau_{VT}^{O_2-O_2}$ [15, 28, 31]. Finally, the Millikan and White correlation provided a prediction for the fifth relaxation time, $\tau_{VT}^{N_2-O_2}$ [15]. While the Millikan and White correlation for N_2-O_2 V-T relaxation retains relatively high uncertainty, the vibrational temperature of O_2 was insensitive to this rate. The V-T relaxation times that strongly impact the N_2 vibrational temperature, $\tau_{VT}^{N_2-N_2}$ and $\tau_{VT}^{N_2-O_2}$, do not strongly impact the vibrational temperature of O_2 (Eq. 4). Due to this insensitivity, fits of the O_2 vibrational temperature time-histories only strongly depended on the two O_2 V-T times and the V-V time.

The early rate of O_2 vibrational temperature increase was fit to determine $\tau_{VT}^{O_2-N_2}$. While the early rise time depended on both $\tau_{VT}^{O_2-O_2}$ and $\tau_{VT}^{O_2-N_2}$, mixtures of 10% and 21% O_2 in N_2 depend much more strongly on $\tau_{VT}^{O_2-N_2}$ due to the mixture rule for V-T times (Eq. 11). Additionally, $\tau_{VT}^{O_2-O_2}$ has been previously studied with relatively low uncertainty [15, 28, 31]. The vibrational temperature was related to the vibrational energy using a simple harmonic approximation (Eq. 12). While a simple harmonic oscillator model for O_2 has been observed to break down at high vibrational levels and high temperatures, for v" = 4,5 and temperatures of 2000-4000 K, a simple harmonic oscillator remains a relatively good approximation [15, 33].

$$\frac{1}{\tau_{VT}^{mix}} = \frac{X_{O_2}}{\tau_{VT}^{O_2-O_2}} + \frac{X_{N_2}}{\tau_{VT}^{O_2-N_2}} \tag{11}$$

$$E_V(T) = \frac{R\theta_V}{\exp\left(\frac{\theta_V}{T}\right) - 1} \tag{12}$$

In addition to the mixture rule and simple harmonic oscillator approximations, the fit of the O_2 vibrational temperature time histories from 0-15 μs neglected any influence from V-V relaxation. At these early times, the vibrational temperatures of both O_2 and N_2 remain far below the translational temperature of the gas mixture. Due to the exponential dependence of E_V on T_v and the definitions of the normalized vibrational energies, X, both X_{O_2} and X_{N_2} remain small at early times, thus providing grounds for neglecting V-V relaxation (Eqs. 4, 5). Once data for $\tau_{VT}^{O_2-N_2}$ was obtained from early times, $\tau_{VV}^{O_2-N_2}$ was obtained by fitting the entire profile. As the O_2 vibrational temperature approached the translational temperature, the role of V-V transfer increased, so particular weight was given to this region. Both the early fits for $\tau_{VT}^{O_2-N_2}$ and the full profile fits for $\tau_{VV}^{O_2-N_2}$ used a least-squares curve fitting toolbox with a 95% confidence interval.

3. Uncertainty Analysis

The uncertainty in measured quantities arose from noise in the optical diagnostics, pressure transducers, and shock velocity measurements and was propagated using a standard root-sum-squares method of error propagation. Uncertainty in both the optical diagnostic and pressure transducer measurements largely arose from electronic noise. For both absorbance and pressure, the standard deviation of the raw signal to the best fit time-history determined the uncertainty. The absorbance best fit was found using a simulation of the relaxation process in tandem with an absorbance model, whereas the pressure best fit was obtained by fitting a polynomial to the post-reflected-shock data.

The shock velocity uncertainty – attributed to attenuation – was propagated to calculate the post-shock temperature uncertainty. Once uncertainty in the absorbance, pressure, and initial temperature were quantified, the uncertainty was propagated to the O_2 vibrational temperature time-histories. The uncertainty in vibrational temperature arose from the uncertainty in the absorbance ratio, and this was amplified by the sensitivity of the temperature diagnostic [26]. However, the wavelengths in this study were selected to maximize the sensitivity of the diagnostic and thereby reduce the vibrational temperature uncertainty.

The uncertainties in the two vibrational relaxation times were found from the fitting uncertainty. The bounds on the 95% confidence interval, found by the least-squares curve fit, defined the fitting uncertainty for $\tau_{VT}^{O_2-N_2}$ and $\tau_{VV}^{O_2-N_2}$. While fitting bounds contributed most strongly to the uncertainty in the vibrational relaxation times, absorbance and temperature uncertainty also contributed slightly. The uncertainty in $\tau_{VT}^{O_2-O_2}$ was taken as a fixed value of 12% as found in previous laser absorption studies [28, 31].

IV. Results

In the following sections, an example absorbance time-history demonstrates typical data quality for a matched shock experiment. Vibrational temperature time-histories, measured using the absorbance ratio, show the vibrational relaxation process for 10% and 21% mixtures of O_2 in N_2 at three temperature conditions. Finally, results from vibrational temperature fits show vibrational relaxation results for $\tau_{VT}^{O_2-N_2}$ and $\tau_{VV}^{O_2-N_2}$. To compare to previous data, the data for $\tau_{VV}^{O_2-N_2}$ are also presented in terms of ${}^{N_2}_{O_2}Q_{0,1}^{1,0}$.

A. Time-Histories

Absorbance time-histories were obtained using the Beer-Lambert relation and measured intensity signals (Eq. 1). An example absorbance time-history for a 10% O_2 in N_2 mixture at 2920 K demonstrates data quality for the two wavelengths probed in this study (Fig. 2). As previously stated, measurements at a wavelength of 211.2 nm probed the fourth vibrational level of the ground state of oxygen and 221.6 nm probed the fifth. Measurements at 221.6 nm exhibited lower noise than those at 211.2 nm due to higher output power from the ultraviolet laser system. While laser output power varied due to wavelength, careful alignment adjustments optimized the laser signal to maximum power prior to each shock experiment.

The raw data for each absorbance time-history was fit to determine the uncertainty. The best-fits were calculated with a vibrational relaxation simulation and an experimentally validated absorbance model to simulate the oxygen vibrational temperature (Eqs. 4, 5) [26]. The simulated O_2 vibrational temperature and initial gas composition provided sufficient information to simulate the absorbance, because dissociation was negligible over the experimental test times at the studied temperatures. While this simulation required values for the five relaxation times, the two self-relaxation times, $\tau_{VT}^{N_2-N_2}$ and $\tau_{VT}^{O_2-O_2}$, were taken from literature, and $\tau_{VT}^{N_2-O_2}$ did not strongly affect the simulation [15, 28, 31]. The iteration upon $\tau_{VT}^{O_2-N_2}$ and $\tau_{VV}^{O_2-N_2}$ reduced the electronic noise while resulting in converged values for simulated and measured relaxation times.

Vibrational temperature time-histories were obtained through the ratio of absorbance at two wavelengths, whereas the translational/rotational time-histories were obtained using the shock jump relations and energy conservation (Eq. 10) [34]. The N_2 vibrational temperature time-histories were calculated for the best-fit simulation using converged values for $\tau_{VT}^{O_2-N_2}$ and $\tau_{VV}^{O_2-N_2}$, literature values for $\tau_{VT}^{N_2-N_2}$ and $\tau_{VT}^{O_2-O_2}$, and the Millikan and White correlation for $\tau_{VT}^{N_2-O_2}$. Six temperature time-histories, measured in repeated shock experiments, are shown for mixtures of 10% and 21% O_2 in N_2 (Fig. 3). These time histories show a steady depression of the O_2 vibrational temperature below the translational temperature at times longer than 50 μs due to V-V energy transfer from O_2 to N_2. This observed difference between $T_v^{O_2}$ and T_{tr} demonstrates the sensitivity of the laser absorption diagnostic when applied to the multiple temperature environment of a vibrationally relaxing mixture of gases.

The uncertainty in the vibrational temperature increased with increasing temperature due to decreasing sensitivity

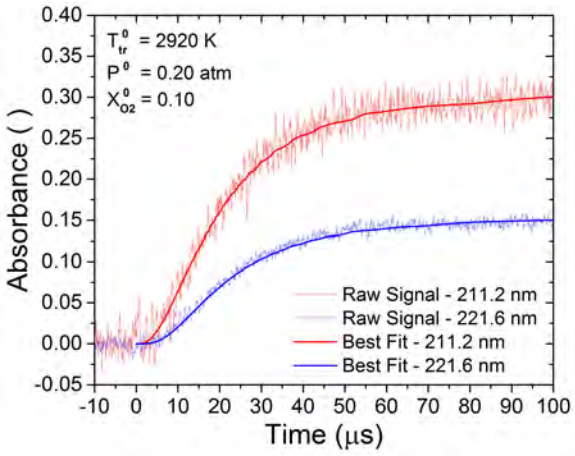

Fig. 2 Absorbance (α) time-history for two matched vibrational relaxation shocks in a 10% O_2/N_2 mixture. While each absorbance trace was measured in separate shock experiments, conditions matched with a temperature difference of no more than 40 K.

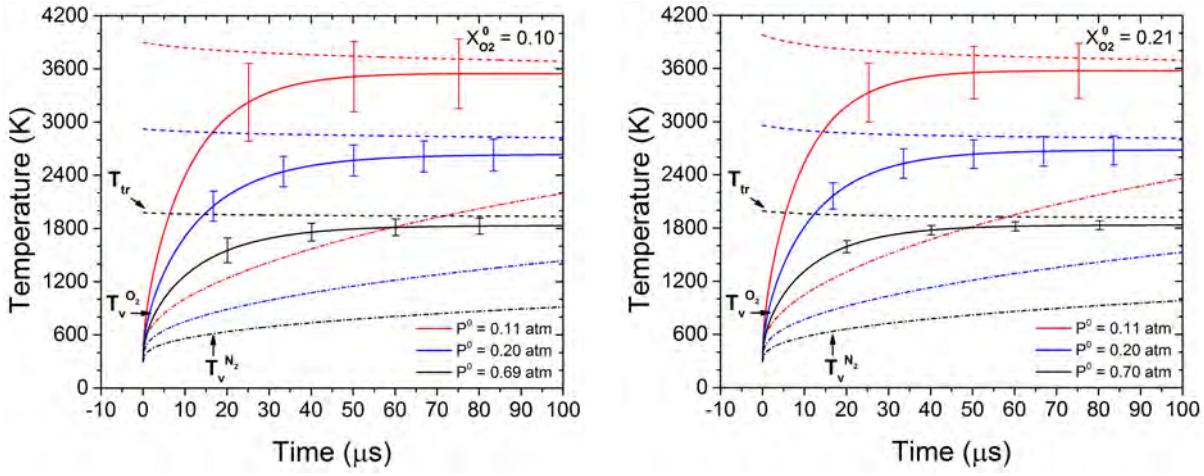

(a) **(b)**

Fig. 3 Temperature time-histories for three 10% (a) and three 21% (b) O_2-N_2 vibrational relaxation experiments. Uncertainty bounds increased at higher temperatures due to lower experimental pressures and lower sensitivity of the absorption diagnostic. These experiments exhibit a persistent difference between T_{tr} and $T_v^{O_2}$ at long times due to V-V energy transfer from O_2 to N_2.

of the temperature diagnostic. Experimental pressures were chosen such that the signal to noise ratio across all three temperatures remained relatively consistent. However, the signal to noise ratio was lower for the 10% O_2 in N_2 experiments than the 21% experiments. Additionally, the uncertainty was larger at early times due to the small absorbance signals. The simulated translational/rotational temperature was observed to decrease very slightly due to the endothermic vibrational relaxation process. This effect was larger at higher temperature and a higher O_2 concentrations. While this effect introduced some uncertainty in the calculation of relaxation times, the uncertainty due to vibrational temperature was much more influential.

B. Relaxation Times

Two vibrational relaxation times, $\tau_{VT}^{O_2-N_2}$ and $\tau_{VV}^{O_2-N_2}$, were determined from fits to the O_2 vibrational temperature time-histories. The V-T relaxation time was determined by fitting the early time data from 0-15 μs and leveraging

previous data for $\tau_{VT}^{O_2-O_2}$. In contrast, the V-V relaxation time was found by fitting the vibrational temperature time-history for the full 100 μs test time. Data for both the V-T and V-V relaxation times were plotted on a Landau-Teller diagram to compare current data to both previous data and the Millikan and White correlation (Fig. 4) [15–17, 19].

Current data for both the V-T and V-V relaxation times fall above model predictions (Fig. 4) [15, 19]. The data for $\tau_{VT}^{O_2-N_2}$ shows longer relaxation times than those predicted by the Millikan and White correlation, and the current data consistently fall above the correlation by about 70%. Similarly, the data for $\tau_{VV}^{O_2-N_2}$ falls above the model predictions of Berend et al. by 70%. Because the Millikan and White correlation was assumed in the studies used in the Berend et al. data fit, these discrepancies are directly related.

Current data agree relatively well with previous experimental data, but exhibits much lower scatter (Fig. 4) [16, 17]. Data taken by White were completed using optical interferometry and infrared emission from carbon monoxide (CO) in mixtures of 5%, 10%, 21%, 33%, and 50% O_2 [16]. The data presented in the original paper distinguished between a fast relaxation time observed at early experimental times and an overall mixture relaxation time. The data presented here interprets the fast relaxation time as a mixture of $\tau_{VT}^{O_2-O_2}$ and $\tau_{VT}^{O_2-N_2}$. To plot the data in terms of $\tau_{VT}^{O_2-N_2}$, the mixture rule was applied to the various mixtures with literature values for $\tau_{VT}^{O_2-O_2}$ (Eq. 11) [28, 31]. In contrast, the results from Generalov and Losev were measured using broadband UV absorption up to much higher temperatures. In this case, the values for $\tau_{VT}^{O_2-N_2}$ were reported without the use of the mixture rule. The low temperature data shows high scatter compared to the higher temperature data. Current results show very good consistency with the lower scatter data above 3000 K. Ultimately current laser absorption data show consistency with previous interferometry, emission, and broadband UV absorption results with especially good agreement at temperature above 3000 K.

In addition to presenting data as vibrational relaxation times, many previous studies reduced data from multiple mixture compositions to determine probabilities of vibrational energy transfer, ${}_{O_2}^{N_2}Q_{0,1}^{1,0}$ (Fig. 5) [16, 18–23]. These experiments, typically employing interferometry or emission diagnostics, obtained values for $\tau_{VV}^{N_2-O_2}$ by assuming Millikan and White correlation values across a range of mixture compositions. Once $\tau_{VV}^{N_2-O_2}$ was determined, the probability of vibrational energy transfer was determined using known concentrations and bimolecular collision rates (Eq. 8). Berend et al. simulated classical trajectories for diatomic molecules with Morse potential functions to determine the probability of vibrational energy transfer and thereby $\tau_{VV}^{N_2-O_2}$ (Fig. 4) [19]. However, the Berend et al. prediction

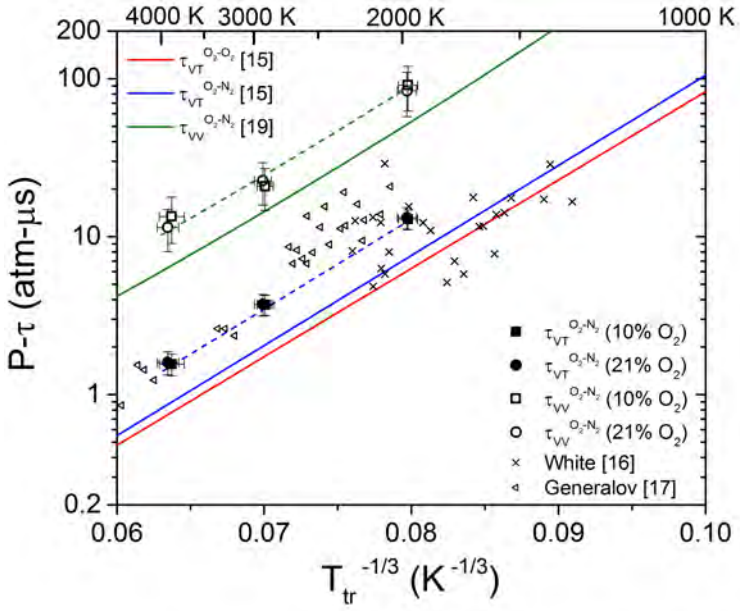

Fig. 4 Landau Teller plot depicting vibrational relaxation times as a function of $T_{tr}^{-1/3}$. Solid lines show predictions taken from the Millikan and White correlations, while dashed lines provide fits to current data [15]. Current data for $\tau_{VT}^{O_2-N_2}$ shows lower scatter than the earlier interferometry measurements by White and the broadband UV absorption measurements by Generalov and Losev [16, 17]. Though not directly measured, $\tau_{VT}^{O_2-O_2}$ is shown for comparison, since it was used in the calculation of $\tau_{VT}^{O_2-N_2}$ at early times.

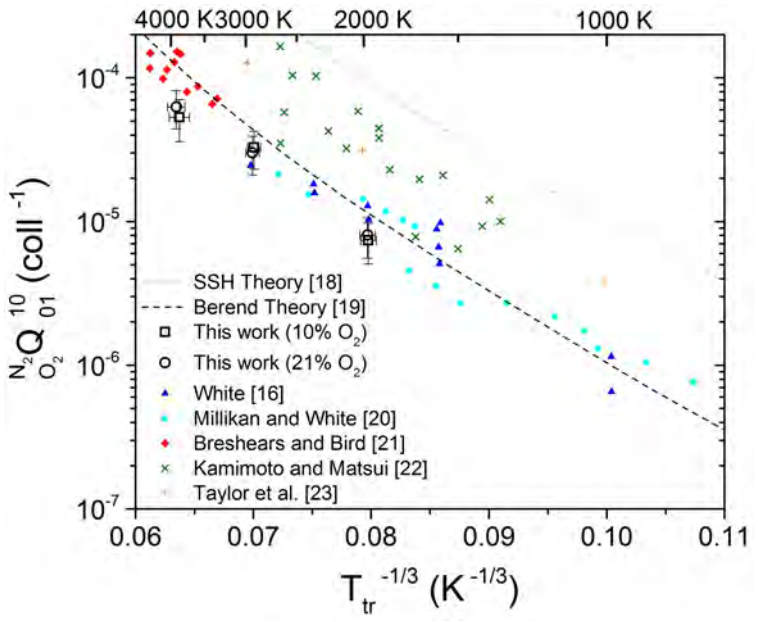

Fig. 5 Probability of vibrational transfer from N_2 to O_2 as a function of $T_{tr}^{-1/3}$. Current data shows slightly lower probabilities than previous data, but previous data assumed Millikan and White correlation values for $\tau_{VT}^{O_2-N_2}$ [16, 20–23]. Though the Berend theory fits literature data well, this fit was enforced by adjusting parameters of the simulated Morse potential [19]. When reported, previous studies exhibited uncertainty of greater than 50% in addition to high scatter [16, 21].

adjusted the range term in the simulated Morse potential to provide a best fit to the available data. Because the Berend et al. prediction fits data that used the Millikan and White correlation for $\tau_{VT}^{O_2-N_2}$ and $\tau_{VT}^{N_2-O_2}$, both model discrepancies stem from the difference between current data and the Millikan and White correlation.

Current data shows lower probability but follows a similar trend as previous data and the Berend et al. prediction (Fig. 5) [19]. While all previous data fall below the predictions of SSH theory, the scatter between studies remains fairly large [18]. Data from Taylor et al. and Kamimoto and Matsui lie at much higher probabilities than the Berend et al. prediction, but the remaining studies show relatively good agreement [16, 20–23]. Current data overlaps with some of the Millikan and White data, but generally falls below data from Breshears and Bird. However, both of these data sets have stated uncertainties greater than 50%, and current data falls within these bounds. While current results fall somewhat below previous data, they exhibit significantly reduced scatter due to the specificity of laser absorption diagnostics.

V. Conclusions

Vibrational relaxation times were measured behind reflected shocks in shock-tube experiments to determine O_2 vibrational temperature time-histories and vibrational relaxation times for $\tau_{VT}^{O_2-N_2}$ and $\tau_{VV}^{O_2-N_2}$. Experiments were completed in mixtures of 10% and 21% O_2 in N_2 at temperatures between 2000 and 4000 K and sub-atmospheric pressures. A tunable, pulsed ultraviolet laser absorption diagnostic probed time-histories involving the fourth (v" = 4) and fifth (v" = 5) vibrationally excited levels of the ground electronic state of O_2 in the Schumann-Runge system. Vibrational temperature time-histories were determined from absorbance time-histories using the ratio of absorbance from 211.2 nm and 221.6 nm experiments. Given that previous studies measured the vibration-translation (V-T) relaxation time of pure O_2, fits of the vibrational temperature time-histories at early times provided sufficient data to isolate $\tau_{VT}^{O_2-N_2}$ [28, 31]. Once the two V-T times were determined, $\tau_{VV}^{O_2-N_2}$ was determined by fitting the full vibrational temperature profile. As current measurements track the vibrational temperature of O_2, this technique exhibits insensitivity to both $\tau_{VT}^{N_2-O_2}$ and $\tau_{VT}^{N_2-N_2}$. Compared to previous studies, values for $\tau_{VT}^{O_2-N_2}$ show lower scatter and uncertainty [16, 17]. Additionally, data for $\tau_{VT}^{O_2-N_2}$ and $\tau_{VV}^{O_2-N_2}$ exceed model predictions by 70% [15, 19]. However, the probability data

used in the Berend et al. fit assumed Millikan and White correlation values for $\tau_{VT}^{O_2-N_2}$ and $\tau_{VT}^{N_2-O_2}$, so the discrepancy in $\tau_{VV}^{O_2-N_2}$ stems from the discrepancy in $\tau_{VT}^{O_2-N_2}$. Results for V-V energy transfer were presented as both a vibrational relaxation time, $\tau_{VV}^{O_2-N_2}$, and a probability of vibrational energy transfer, ${}^{N_2}_{O_2}Q_{0,1}^{1,0}$ the latter of which exhibits much lower scatter than previous studies [16, 20–23]. While previous studies applied interferometry, emission, and broadband UV absorbance, this study demonstrates the first application of laser absorption spectroscopy to the determination of vibrational relaxation times in air.

Acknowledgments

The authors would like to thank Dr. K. Hanquist at the Univesity of Arizona and Dr. R. Chaudhry at the University of Michigan for discussions about computational models. This work was supported by the Air Force Office of Scientific Research through AFOSR grant FA9550-16-1-0291 with contract monitor Dr. I. Leyva.

References

[1] Treanor, C. E., and Marrone, P. V., "Effect of Dissociation on the Rate of Vibrational Relaxation," *Physics of Fluids*, Vol. 5, No. 9, 1962, pp. 1022–1026.

[2] Marrone, P. V., and Treanor, C. E., "Chemical Relaxation with Preferential Dissociation from Excited Vibrational Levels," *Physics of Fluids*, Vol. 6, No. 9, 1963, pp. 1215–1221.

[3] Josyula, E., and Bailey, W. F., "Vibration-Dissociation Coupling Using Master Equations in Nonequilibrium Hypersonic Blunt-Body Flow," *Journal of Thermophysics and Heat Transfer*, Vol. 15, No. 2, 2001, pp. 157–167.

[4] Hank, J., Murphy, J., and Mutzman, R., "The X-51A Scramjet Engine Flight Demonstration Program," *15th AIAA International Space Planes and Hypersonic Systems and Technologies Conference*, 2008, pp. 1–13.

[5] Walker, S., Sherk, J., Shell, D., Schena, R., Bergmann, J., and Gladbach, J., "The DARPA/AF Falcon Program: The Hypersonic Technology Vehicle #2 (HTV-2) Flight Demonstration Phase," *15th AIAA International Space Planes and Hypersonic Systems and Technologies Conference*, Vol. 2, 2008, pp. 1–9.

[6] Dolvin, D., "Hypersonic International Flight Research and Experimentation Technology Development and Flight Certification Strategy," *16th AIAA/DLR/DGLR International Space Planes and Hypersonic Systems and Technologies Conference*, 2009.

[7] Kimmel, R.L., and Adamczak, D., "Hypersonic International Flight Research and Experimentation (HIFiRE) Fundamental Science and Technology Development Strategy," 2008, pp. 1–11.

[8] Urzay, J., "Supersonic Combustion in Air-Breathing Propulsion Systems for Hypersonic Flight," *Annual Revew of Fluid Mechanics*, Vol. 50, No. 1, 2018, pp. 593–627.

[9] Nompelis, I., Candler, G. V., and Holden, M. S., "Effect of Vibrational Nonequilibrium on Hypersonic Double-Cone Experiments," *AIAA Journal*, Vol. 41, No. 11, 2003, pp. 2162–2169.

[10] Coblish, J., Smith, M., Hand, T., Candler, G., and Nompelis, I., "Double-Cone Experiment and Numerical Analysis at AEDC Hypervelocity Wind Tunnel No. 9," *43rd AIAA Aerospace Sciences Meeting and Exhibit*, 2005.

[11] Nompelis, I., Candler, G., MacLean, M., Wadhams, T., and Holden, M., "Numerical Investigation of High Enthalpy Chemistry on Hypersonic Double-Cone Experiments," *43rd AIAA Aerospace Sciences Meeting and Exhibit*, 2005.

[12] Druguet, M.-C., Candler, G., and Nompelis, I., "Comparison of Physical Models in Computations of High-Enthalpy Double-Cone Flows," *9th AIAA/ASME Joint Thermophysics and Heat Transfer Conference*, 2006.

[13] Nompelis, I., and Candler, G., "Investigation of Hypersonic Double-Cone Flow Experiments at High Enthalpy in the LENS Facility," *45th AIAA Aerospace Sciences Meeting and Exhibit*, 2007.

[14] Holloway, M. E., Hanquist, K. M., and Boyd, I. D., "Effect of Thermochemistry Modeling on Hypersonic Flow over a Double Cone," *AIAA Scitech Forum*, 2019.

[15] Millikan, R. C., and White, D. R., "Systematics of Vibrational Relaxation," *The Journal of Chemical Physics*, Vol. 39, No. 12, 1963, pp. 3209–3213.

[16] White, D. R., "Shock-Tube Study of Vibrational Exchange in N_2–O_2 Mixtures," *The Journal of Chemical Physics*, Vol. 49, No. 12, 1968, pp. 5472–5476.

[17] Losev, S. A., and Generalov, N. A., "Vibrational Excitation and Decomposition of Molecular Oxygen and Carbon Dioxide Behind Shock Waves," *Journal of Quantitative Spectroscopy and Radiative Transfer*, Vol. 6, No. 1, 1966, pp. 101–125.

[18] Schwartz, R. N., Slawsky, Z. I., and Herzfeld, K. F., "Calculation of Vibrational Relaxation Times in Gases," *Journal of Chemical Physics*, Vol. 20, No. 10, 1952, pp. 1591–1599.

[19] Berend, G. C., Thommarson, R. L., and Benson, S. W., "Vibration-Vibration Energy Exchange in N_2 with O_2 and HCl Collision Partners," *The Journal of Chemical Physics*, Vol. 57, No. 9, 1972, pp. 3601–3604.

[20] Millikan, R. C., and White, D. R., "Vibrational Relaxation in Air," *AIAA Journal*, Vol. 2, No. 10, 1964, pp. 1844–1846.

[21] Breshears, W. D., and Bird, P. F., "Effect of Oxygen Atoms on the Vibrational Relaxation of Nitrogen," *Journal of Chemical Physics*, Vol. 48, No. 10, 1968, pp. 4768–4773.

[22] Kamimoto, G., and Matsui, H., "Vibrational Energy Exchange on N_2-O_2 Collision," *AIAA Journal*, Vol. 7, No. 12, 1969, pp. 2358–2360.

[23] Taylor, R. L., Camac, M., and Feinberg, R. M., "Measurements of Vibration-Vibration Coupling in Gas Mixtures," *Symposium (International) on Combustion*, Vol. 11, No. 1, 1967, pp. 49–65.

[24] Blackman, V., "Vibrational Relaxation in Oxygen and Nitrogen," *Journal of Fluid Mechanics*, Vol. 1, No. 1, 1956, pp. 61–85.

[25] Campbell, M. F., Owen, K. G., Davidson, D. F., and Hanson, R. K., "Dependence of Calculated Postshock Thermodynamic Variables on Vibrational Equilibrium and Input Uncertainty," *Journal of Thermophysics and Heat Transfer*, Vol. 31, No. 3, 2017, pp. 586–608.

[26] Krish, A., Streicher, J. W., and Hanson, R. K., "Ultraviolet Absorbance Cross-Section Measurements of Shock Heated O_2 using a Tunable Laser from 2,000-10,700 K," *Journal of Quantitative Spectroscopy and Radiative Transfer*, in prep.

[27] Owen, K. G., Davidson, D. F., and Hanson, R. K., "Measurements of Oxygen Dissociation Using Laser Absorption," *Journal of Thermophysics and Heat Transfer*, Vol. 30, No. 2, 2016, pp. 274–278.

[28] Owen, K. G., Davidson, D. F., and Hanson, R. K., "Oxygen Vibrational Relaxation Times: Shock Tube/Laser Absorption Measurements," *Journal of Thermophysics and Heat Transfer*, Vol. 30, No. 4, 2016, pp. 791–798.

[29] Bykova, N. G., and Kuznetsova, L. A., "Study of the Absorption Characteristics of Molecular Oxygen in the Schumann-Runge System at High Temperatures: I. Calculations of Absorption Spectra," *Optics and Spectroscopy*, Vol. 105, No. 5, 2008, pp. 668–673.

[30] Bykova, N. G., Zabelinskii, I., Ibraguimova, L. B., and Shatalov, O. P., "Study of the absorption characteristics of molecular oxygen in the Schumann-Runge system at high temperatures: II. Experiment and Comparison with Calculation," *Optics and Spectroscopy*, Vol. 105, No. 5, 2008, pp. 674–679.

[31] Streicher, J. W., Krish, A., Wang, S., Davidson, D. F., and Hanson, R. K., "Measurements of Oxygen Vibrational Relaxation and Dissociation Using Ultraviolet Laser Absorption in Shock Tube Experiments," *AIAA Scitech Forum*, 2019, pp. 1–11.

[32] Bethe, H., and Teller, E., "Deviations From Thermal Equilibrium in Shock Waves," , 1941.

[33] Ibraguimova, L. B., Sergievskaya, A. L., Levashov, V. Y., Shatalov, O. P., Tunik, Y. V., and Zabelinskii, I. E., "Investigation of Oxygen Dissociation and Vibrational Relaxation at Temperatures 4000-10800 K," *Journal of Chemical Physics*, Vol. 139, No. 3, 2013.

[34] McBride, B. J., Zehe, M. J., and Gordon, S., "NASA Glenn Coefficients for Calculating Thermodynamic Properties of Individual Species," Tech. Rep. September, 2002.